UNIVERSIDADE FEDERAL DO CEARÁ

CENTRO DE TECNOLOGIA

DEPARTAMENTO DE ENGENHARIA DE TELEINFORMÁTICA

PROGRAMA DE PÓS-GRADUAÇÃO EM ENGENHARIA DE TELEINFORMÁTICA

DOUTORADO EM ENGENHARIA DE TELEINFORMÁTICA

RUBEM VASCONCELOS PACELLI

DETECTION AND CHARACTERIZATION OF EQUATORIAL IONOSPHERIC SCINTILLATION BASED ON GNSS OBSERVATIONS USING CONVOLUTIONAL NEURAL NETWORKS

FORTALEZA

2026

RUBEM VASCONCELOS PACELLI

DETECTION AND CHARACTERIZATION OF EQUATORIAL IONOSPHERIC SCINTILLATION BASED ON GNSS OBSERVATIONS USING CONVOLUTIONAL NEURAL NETWORKS

Tese apresentada ao Programa de Pós-Graduação em Engenharia de Teleinformática do Centro de Tecnologia da Universidade Federal do Ceará, como requisito parcial à obtenção do título de doutor em Engenharia de Teleinformática. Área de Concentração: Sinais e Sistemas

Orientador: Prof. Dr. Felix Dieter Antreich

Coorientador: André Lima Ferrer de Almeida

FORTALEZA

2026

RUBEM VASCONCELOS PACELLI

DETECTION AND CHARACTERIZATION OF EQUATORIAL IONOSPHERIC SCINTILLATION BASED ON GNSS OBSERVATIONS USING CONVOLUTIONAL NEURAL NETWORKS

Tese apresentada ao Programa de Pós-Graduação em Engenharia de Teleinformática do Centro de Tecnologia da Universidade Federal do Ceará, como requisito parcial à obtenção do título de doutor em Engenharia de Teleinformática. Área de Concentração: Sinais e Sistemas

Aprovada em: 31 de Março de 2026

BANCA EXAMINADORA

Prof. Dr. Felix Dieter Antreich (Orientador)
Instituto Tecnológico de Aeronáutica (ITA)

André Lima Ferrer de Almeida (Coorientador)
Universidade Federal do Ceará (UFC)

Prof. Dr. Fazal-E-Asim
Universidade Federal do Ceará (UFC)

Prof. Dr. Tarcisio Ferreira Maciel
Universidade Federal do Ceará (UFC)

Prof. Dr. Jens Berdermann
Deutsche Zentrum für Luft- und Raumfahrt
(DLR)

Prof. Dr. Michael Joham
Technische Universität München (TUM)

Dedico esta Tese à Rita Gabriella de Lima Maia, minha amada mulher, pelo incentivo, compreensão e apoio à minha jornada acadêmica e profissional. Seu amor e sua presença, além de terem sido fundamentais para que eu concluísse este Doutorado, servem de alicerce para a minha vida.

AGRADECIMENTOS

I am grateful to my supervisor, Professor Felix Antreich, who has embraced me as a PhD student and guided me through the research process with his expertise and support. Without his guidance, this thesis would not have been possible as he has provided me with the necessary resources and opportunities to conduct my research and has always been available to discuss my ideas and provide feedback.

I would also like to thank my co-supervisor, Professor André Lima Ferrer de Almeida, who accepted the transition of my PhD supervision to Professor Felix and enabled the cotutelle agreement between the Federal University of Ceará and Polytechnic University of Catalonia.

I am also grateful to the professors and partners from the Polytechnic University of Catalonia, who have welcomed me during my research stay in Barcelona and provided me with valuable insights and feedback on my research. Also, I want to express my gratitude to my UPC supervisor, Professor Angela Aragon-Angel, who has provided me with the opportunity to conduct research in the field of scintillation monitoring at UPC, and to Adria, who has been a great technical instructor and collaborator during my research stay.

A special thanks to colleagues during my other stay in Aeronautics Institute of Technology, São José dos Campos, São Paulo, who have provided me with some good moments.

I gratefully acknowledge the financial funders of my PhD research. In particular, to Brazil's National Council for Scientific and Technological Development (CNPq) under grant 406517/2022-3, 407245/2022-7, and 305064/2025-8 PQ-C, Brazil's Funding Authority for Studies and Projects (FINEP) under grant 01.22.0581.00 and Coordination for the Improvement of Higher Education Personnel (CAPES) grant with number 88887.975685/2024-00, the European Commission through the scholarships 165074/2021-3 and the project Galileo Information Center for Brazil, Grant Agreement SI2.809402.

Finally, I would like to thank my girlfriend, Gabriella, for her love and for being my best friend, being the person who truly supported me in the hard moments.

"Isn't that intriguing? We start by understanding theorems, definitions, principles... all of which build huge walls for the analytical understanding of a complex system that otherwise could not be comprehended. The paradox, however, happens only after years of struggle, when the apparent restrictive concreteness of Engineering, which once seemed to limit you, now grant you freedom. There are no rules, no transgressions, no wrongdoings. It is only you, God's axioms, and your ability to describe the reality surround you. Engineering is nothing but the sheer art of crafting ideas at your free will, but the beauty of its connotation is revealed only to the stubborn ones."

(Monologue in a dream.)

RESUMO

Receptores de Sistemas Globais de Navegação por Satélite (GNSS) operando na região equatorial são severamente afetados por cintilação ionosférica, causando rápidas flutuações na amplitude e fase da onda eletromagnética. Para monitorar a atividade de cintilação, receptores comerciais tipicamente fornecem os índices S_4 e σ_ϕ, calculados a partir de limiares *ad-hoc* e técnicas de remoção de tendência. Além da limitação intrínseca de se restringirem a um problema de classificação M-ário, esses métodos de filtragem são conhecidos por mascarar eventos de cintilação. A presente tese propõe uma mudança de paradigma na caracterização da cintilação ionosférica. Em vez de depender de técnicas de remoção de tendência e limiares pré-estabelecidos, métodos bayesianos recentes são empregados para separar o sinal de cintilação da dinâmica da linha de visada, e novos algoritmos de redes neurais convolucionais são investigados para a tarefa de caracterização. Um modelo simplificado de sinal é derivado e utilizado para gerar séries temporais sintéticas de cintilação com base em dois modelos de cintilação ionosférica: o modelo de cintilação de Cornell e o modelo compacto de cintilação baseado em tela de fase. A principal contribuição é um novo framework que combina redes neurais convolucionais e mapas de ativação de classe como ferramenta de interpretabilidade *post-hoc* que destaca as regiões de entrada mais relevantes para a tarefa discriminativa. Essa abordagem torna possível analisar amostras cujas características tendem a ser classificadas como cintilação forte em vez de fraca, e vice-versa, sem estabelecer limiares arbitrários ou recorrer a heurísticas *ad-hoc* definidas para obter índices de cintilação. Os resultados demonstram acurácia média acima de 89%, o que viabiliza a caracterização da severidade da cintilação em nível de amostra e oferece melhorias significativas em comparação aos métodos tradicionais de classificação baseados em limiares, utilizados em aplicações de monitoramento de cintilação ionosférica.

Palavras-chave: GNSS, caracterização da cintilação equatorial, redes neurais convolucionais, mapas de ativação de classe .

ABSTRACT

Global Navigation Satellite Systems (GNSS) receivers operating in the equatorial region are severely affected by ionospheric scintillation caused by rapid fluctuations in the amplitude and phase of the received electromagnetic wave. To monitor scintillation activity, commercial receivers typically provide the S_4 and σ_ϕ indices, which are computed using *ad-hoc* thresholds and detrending techniques. In addition to the intrinsic limitation of being restricted to an M-ary classification problem, these filtering methods are known to mask scintillation events. The present thesis proposes a paradigm shift in the characterization of ionospheric scintillation. Instead of relying on detrending techniques and preset thresholds, recent Bayesian methods are employed to disentangle the scintillation signal from line-of-sight dynamics, and new convolutional neural network algorithms are investigated for the characterization task. A simplified signal model is derived and used to generate synthetic scintillation time series based on two ionospheric scintillation models: the Cornell Scintillation Model and the compact phase-screen-based scintillation model. The main contribution of this thesis is a new framework that combines convolutional neural networks and class activation maps as a *post-hoc* interpretability tool that highlights input regions most relevant to the discriminative task. This approach makes it possible to analyze samples whose features are prone to be classified as strong rather than weak scintillation, and the converse, without setting arbitrary thresholds or relying on *ad-hoc* heuristics established to obtain scintillation indices. The results demonstrate an average accuracy above 89%, which enables sample-level characterization of the severity of scintillation and provides significant improvements compared to traditional threshold-based classification methods used in ionospheric scintillation monitoring applications.

Keywords: GNSS, equatorial scintillation characterization, convolutional neural networks, class activation maps.

LIST OF FIGURES

LIST OF TABLES

LIST OF ABBREVIATIONS AND ACRONYMS

1PPS	1-Hz pulse per second
AACGM	Altitude-adjusted corrected geomagnetic coordinate
ACF	Autocorrelation function
ADAM	Adaptive moment estimation
ADC	Analog-to-digital converter
AGC	Automatic gain control
AKF	Adaptive Kalman filter
AltBOC	Alternative BOC
AR	Autoregressive
AWGN	Additive white Gaussian noise
BB	Baseband
C/N_0	Carrier-to-noise ratio
CAM	Class activation map
CDF	Cumulative distribution function
CDMA	Code division multiple access
CLT	Closed-loop tracking
CNN	Convolutional neural network
CPSSM	Compact phase-screen-based scintillation model
CSK	Code shift key
CSM	Cornell scintillation model
DAQ	Data acquisition
dCAM	Dimension-wise class activation map
dCNN	Dimension-wise convolutional neural network
DDM	Doppler-delay map
DL	Deep learning
DLL	Delay-locked loop
DNN	Deep neural network
EKF	Extended Kalman filter
EUV	Extreme ultraviolet
FC	Fully connected
FFT	Fast Fourier transform

FLL	Frequency-locked loop
GAP	Global average pooling
GEO	Geostationary earth orbit
GISTM	GNSS ionospheric scintillation and TEC monitors
GNSS	Global navigation satellite systems
GPS	Global positioning system
HA	High accuracy
IF	Intermediate frequency
IGRF	International geomagnetic reference field
IPE	Irregularity parameter estimation
IPP	Ionospheric pierce point
ISMR	Ionospheric scintillation monitoring receiver
KF	Kalman filter
LEO	Low earth orbit
LNA	Low noise amplifier
LO	Local oscillator
LOS	Line-of-sight
LPF	Lowpass filter
MC	Multiconstellation
MEO	Medium earth orbit
MF	Multifrequency
MLP	Multilayer perceptron
MM	Mass market
NCO	Numerically-controlled oscillator
NN	Nearest neighbour
NP	Neyman-Pearson
OCXO	Oven-controlled crystal oscillator
OLT	Open-loop tracking
PDF	Probability density function
PLL	Phase-locked loop
PPP	Precise point positioning
PR	Pseudorandom

PSD	Power spectral density
PVT	Position, velocity, and time
PWE	Parabolic wave equation
QPSK	Quadrature phase-shift keying
ReLU	Rectified linear unit
RF	Radio frequency
RF-FE	Radio frequency front end
RINEX	Receiver independent exchange format
RT	Rayleigh-Taylor
RTK	Real-time kinematics
SCAp	Safety- and liability-critical applications
SDR	Software-defined radio
SGD	Stochastic gradient descent
SNR	Signal-to-noise ratio
SOLT	Semi-open loop tracking
SOTA	State of the art
SSM	State-space model
SVC	Support vector classifier
SVM	Support vector machine
TCXO	Temperature compensated crystal oscillator
TEC	Total electron content
TPPSM	Two-component power-law phase-screen model
TSC	Time series classification
TTM	Tensor-times-matrix
UHF	Ultra high frequency
VHF	Very high frequency
WSS	Wide-sense stationary

LIST OF SYMBOLS

CONTENTS

1 INTRODUCTION

The main focus of this thesis is to provide new characterization methods for equatorial ionospheric scintillation. The goal of the present chapter is to provide the required background and outline the thesis motivation and contribution. Hence, the following issues are addressed:

1. introduction to equatorial scintillation, covering its morphology and impact on global navigation satellite systems (GNSS);
2. literature review on ionospheric scintillation monitoring;
3. definition of the thesis outline, motivation, and contribution;

1.1 Morphology of equatorial scintillation

The ionosphere is the uppermost layer of the Earth's atmosphere, from 50 km to 1000 km altitude, and is heavily ionized by solar radiation (TEUNISSEN; MONTENBRUCK, 2017, p. 12). On the one hand, visible and infrared wavelengths can pass through the atmosphere since they are too long to ionize the neutral gas. On the other hand, extreme ultraviolet (EUV) and X-ray radiations are absorbed in the upper atmosphere, thus ionizing the medium. As solar rays penetrate the atmosphere, the number of free electrons (and hence the capacity to create ions) increases insofar as the radiation intensity reduces due to absorption (TEUNISSEN; MONTENBRUCK, 2017, p. 177). The ionized gases (i.e., O, O_2, N, N_2, and NO) create an electron density profile throughout each layer of the ionosphere:

- the F layer (150 km to 1000 km) is the largest and most ionized layer of the ionosphere. The EUV radiation plays a major role in the ionization of this region, where the density of free electrons increases along the F1 layer (150 km to 200 km) and reaches its maximum value within the F2 layer (200 km to 1000 km). This region of maximum electron density is referred to as the Chapman layer (DAVIES, 1990), and its peak is time-dependent, reaching maximum value at 14 h local time and minimum before sunrise. Likewise, the height at which the peak occurs also has a diurnal dependence, where it tends to fall at dawn and rise during the evening hours (KNIGHT, 2000);
- the E layer (90 km to 150 km) is mainly ionized by X-rays: due to their wavelength, they can travel even further Earthwards without losing much of their energy in the F layer. X-rays accompanying solar flare eruptions cause an enhancement in the ionization of the E layer at 100 km, approximately (TEUNISSEN; MONTENBRUCK, 2017, p. 178).

Some of the observed scintillations can be caused by the irregularities in this layer, such as sporadic E and auroral E (AARONS, 1982);

- the D layer (60 km to 90 km), the lowest ionospheric layer, exhibits minimal free electron density, disappearing at night.

Figure 1 shows a typical free electron density profile during daytime and nighttime.

Figura 1 – A typical electron density profile.

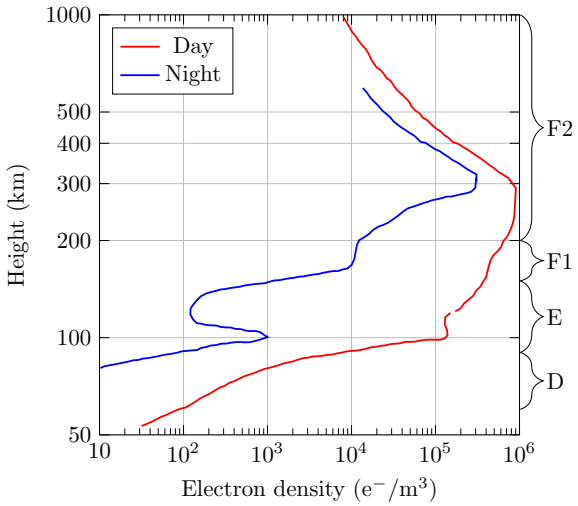

Fonte: Adapted from (MORAES; PERRELLA, 2009-Jul-Dec).

Ionospheric scintillation occurs mainly in the F2 layer, when the free electrons yield inhomogeneous plasmas (or bubbles) with a time-varying refractive index. Transionospheric radio waves passing through them suffer a combined effect of diffraction and refraction:

- When the plane wavefront encounters an inhomogeneous plasma, the difference between the refractive index of the medium and the plasma alters the wavefront velocity and direction. This effect, called refraction, occurs not only when the wave penetrates the irregular plasma but also within it because its electron density is nonuniform. When the refractive index is low, the velocity of the radio wave is higher and the wavefront will advance farther. When the refractive index is high, the wavefront is retarded (VASYLYEV *et al.*, 2022). However, for wave propagation in an ionized medium, the group velocity times the phase velocity equals the speed of light squared (CHENG, 2013, p. 378). To maintain this relationship constant, the phase velocity is increased when the group velocity is decreased. On the one hand, the decreased group velocity leads to a group delay in the incoming signal, which leads to code based ranging errors. On the other hand, an increase in the phase velocity leads to phase advance, which challenges the carrier phase tracking

loop. The compound effect of code delay and phase advance is known as code-phase divergence and is one of the main effects of refraction.

- The electromagnetic waves can also surround the irregularities instead of passing through them, especially when the size of the irregularities is small. This effect, called diffraction, creates a spatial scattering pattern which is converted into a temporal one by the relative movement between the receiver and the satellites or by changes in the structure of the irregularities (KNIGHT *et al.*, 1998). Some portions of the wavefront will be convex (focusing) while others will be concave (defocusing). Moreover, the scattered waves can superimpose constructively or destructively, thus leading to a complex pattern with deep fades and, eventually, some signal instantaneous power enhancement. This phenomenon can be observed in Figure 2, where it shows the plot of the carrier-to-noise ratio (C/N_0) estimation over time for two satellites, one experiencing scintillation and the other with no scintillation, at all. The required C/N_0 limit for tracking and acquisition were added for the sake of benchmark.

This combined effect of refraction and diffraction occurred within the ionosphere is called ionospheric scintillation.

Figura 2 – C/N_0 level for scintillation (blue curve) and nonscintillation (red curve) events.

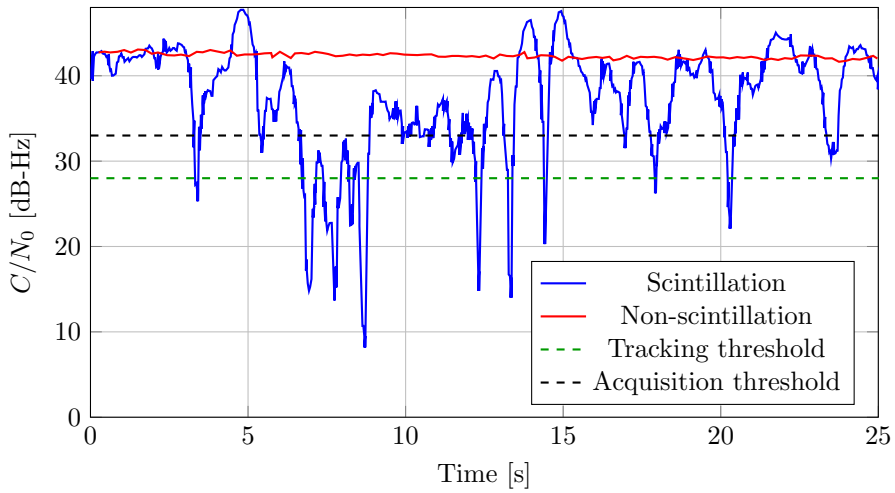

Fonte: Adapted from Kintner *et al.* (2007).

1.1.1 Geographical and seasonal dependency

Ionospheric scintillation usually occurs in two contrasting regions on the globe: the low-latitude or equatorial region (within $\pm 20^\circ$ around the magnetic equator) and the high-latitude region (comprising the polar and auroral zones, from 55° to 90°). Some articles have shown that

ionospheric scintillation in these regions differs in terms of generating mechanisms, intensity and statistics (BASU *et al.*, 1987; JIAO *et al.*, 2013), which makes the analysis of the event dependent on the geographical context. Here, we will focus on the equatorial scintillation, which is the main topic of this thesis.

At low latitudes, the height of the free electrons is pronounced due to a $\mathbf{E} \times \mathbf{B}$ force created by the geomagnetic field and an eastward electric field in the E layer, which becomes enhanced after the sunset. This vector field pulls the F layer upwards, moving the free electron peak to approximately 500 km, which occurs around 19 h local time (KNIGHT, 2000). At this height, the temperature and pressure are low enough so that the electrons can travel freely without recombining into neutral gas for a longer time. Therefore, the electron density in the heightened F2 layer remains relatively high, especially after dusk. Due to gravity and pressure gradient, these free electrons are forced downwards along the magnetic field lines, thus creating regions with high electron density at approximately ± 20 degrees with respect to the geomagnetic equator. Such regions are called *equatorial anomaly*, and the phenomenon that gives rise to it, shown in Figure 3, is called *fountain effect* (LUCENA *et al.*, 2021). Satellite navigation services operating around the geomagnetic equator, as shown in Figure 4, can experience an enhanced scintillation intensity due to equatorial anomaly.

Figura 3 – Fountain effect, which gives rise to the equatorial anomaly.

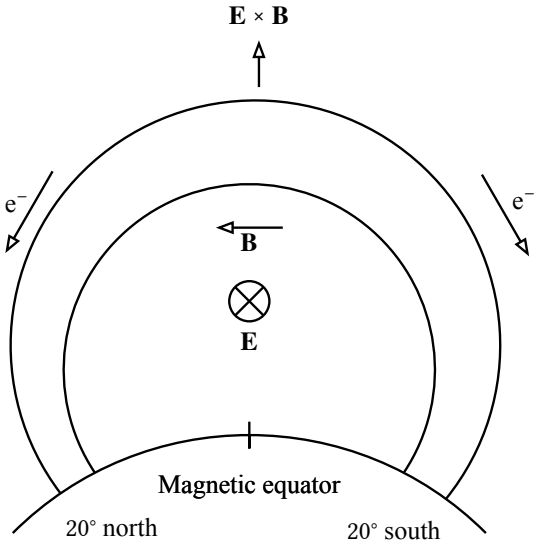

Figura 4 – Total electron content unit (TECU) map varying wordwide according to the local time for a given day. The color-bars values range is fixed within each snapshot.

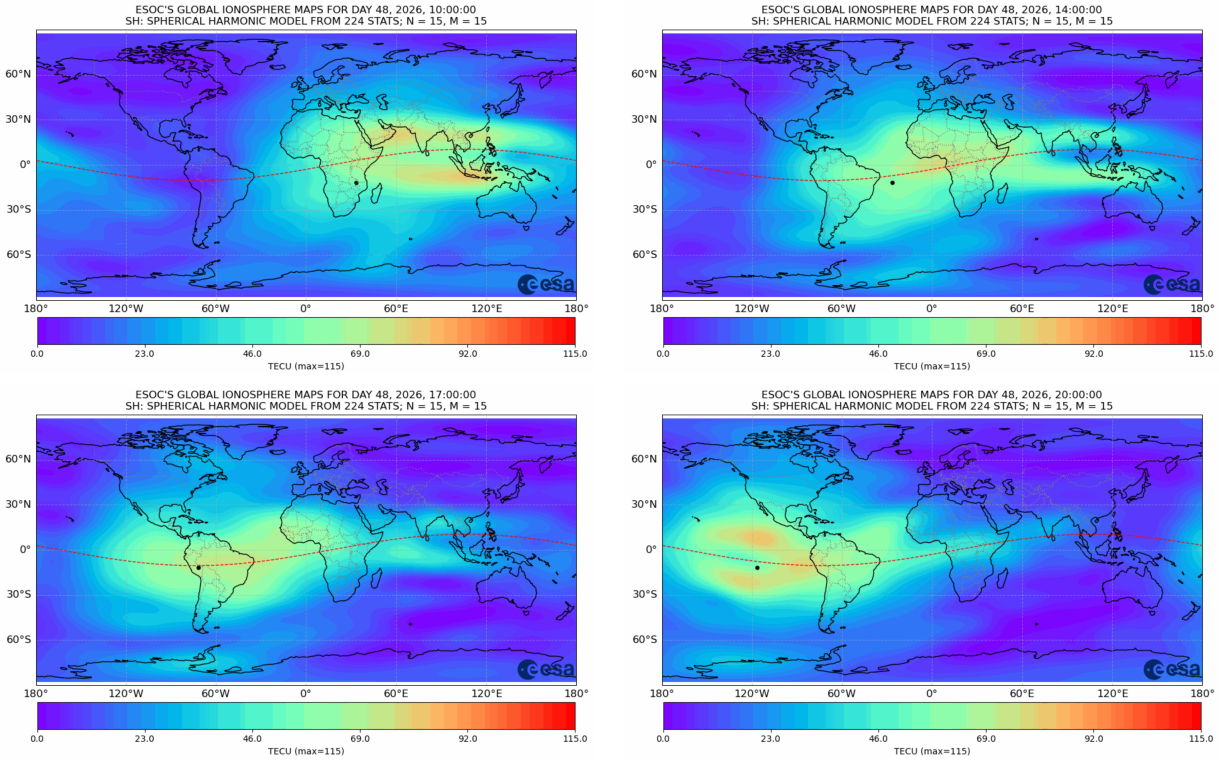

Fonte: Obtained from Feltens (2026).

During the nighttime, the free electron density diminishes in the E layer due to the absence of the Sun, and the number of recombinations is large enough to create a low-density plasma. Therefore, two layers with contrasting plasma densities are created where a high-density medium (in F layer) is supported by a low-density medium (in E layer), thus creating an unstable equilibrium (SILVA, 2017). The formation of low-density plasma bubbles formed at the base of the F layer is credited by many authors to the generalized Rayleigh-Taylor (RT) plasma instability[1] (ABDU *et al.*, 1981; KELLEY, 1985; ABDU, 2001). Such a phenomenon generates irregularities highly elongated along the geometric field lines (KINTNER *et al.*, 2004) with a large scale spectrum range, varying from dozens of centimetres to hundreds of kilometres (PAULA *et al.*, 2003). However, for signals in very high frequency (VHF) or ultra high frequency (UHF), the inhomogeneities responsible for scintillation are mainly those in the scale of hundreds of meters (NUNES *et al.*, 2022). Since this is in the same order of magnitude as the Fresnel scale (BÉNIGUEL, 2011), diffraction dominates the overall scintillation effect in equatorial region

[1] This theory was initially proposed by Dungey in 1956 (DUNGEY, 1956) after some irregularities in the F layer had been observed by Booker and Wells in 1938 (BOOKER; WELLS, 1938). The hydrodynamic RT instability was proposed as the primary generation process of ionospheric instabilities. Then, other parameters such as electric field, neutral wind, and plasma density gradient were included in the RT theory, thus forming the generalized RT instability.

(KINTNER *et al.*, 2009).

Concerning scintillation intensity, two kinds of patterns can be identified: for an amplitude scintillation index (*vide* Appendix A) below 0.5, the amplitude and phase scintillations are linearly correlated, while for greater values there is no apparent correlation (ITU-R, 2007). Regardless, the amplitude fluctuation is notably higher than the phase, thus causing deep fading of the received signal. In practice, equatorial scintillation is usually observed after sunset and the subsequent evening hours (KNIGHT, 2000). Moreover, the equatorial scintillation intensity has a strong seasonal dependency, being more severe in the equinoxes (spring and autumn) and milder in the summer. Its intensity is also correlated with the solar activity during the 11-year solar cycle, peaking at the solar maximum (FOHLMEISTER *et al.*, 2018).

1.1.2 Frequency dependency

The impact of ionospheric scintillation on electromagnetic waves changes depending on their frequency. For weak to moderate scintillation conditions (*i.e.*, $S_4 < 0.6$) and for a frequency range from 138 MHz to 2.9 GHz, the scintillation activity is roughly consistent with $S_4 \propto f^{-1.5}$ (AARONS, 1982), where S_4 is the amplitude scintillation index (*vide* Appendix A). This exponent increases for more intense scintillation regimes.

The frequency-dependent behavior of scintillation poses a practical concern for satellite-based navigation systems as multiconstellation (MC) and multifrequency (MF) receivers that have been widely adopted to provide high accuracy with a long continuity of satellite services.

1.2 Effects of ionospheric scintillation in GNSS receivers

The principal impact of scintillation in GNSS receivers resides in the tracking capabilities and consequently the accuracy of the position, velocity, and time (PVT) solution. Synchronization is the key part of a precise positioning output once 1 µs of error leads to a positioning error of almost 300 m. As a result, this requirement is much tighter for GNSS than in other communication systems (EGEA-ROCA *et al.*, 2022). From the signal processing perspective, ionospheric scintillation can be viewed as a noise that impairs the acquisition and mainly the tracking module. When the tracked carrier phase is momentarily slipped by one

or more full or half[2] cycles, and then the loop recovers the lock, a "phase unlock" or "cycle slips" is said to have occurred. However, during intense scintillation events, the tracking loop may not recover the lock, thus leading[3] to a "frequency unlock", "drop lock", or "loss of lock" (HUMPHREYS *et al.*, 2010a). In some cases, the loss of lock can last hours due to long scintillation events, making the system inoperative if the receiver cannot lock more than four in-view satellites. Figure 2 shows a comparative example of the estimated C/N_0 level for two satellites, one in the presence and the other absence of scintillation.

Approaches to ionospheric scintillation depend on the application. mass-market (MM) receivers prioritize low power and cost, so they simply tolerate amplitude and phase fluctuations and keep computing the PVT solution using only the code phase measurements. Professional segments such as high accuracy (HA) and safety- and liability-critical applications (SCAp) detect and reject data affected by potential scintillation to meet performance standards (VILÀ-VALLS *et al.*, 2020; EGEA-ROCA *et al.*, 2022). Scientific applications adopt the opposite direction, collecting scintillation-corrupted data to characterize it statistically and to develop detection, mitigation, and forecasting methods. In every case where scintillation is of concern, monitoring is essential.

1.3 Literature review

This section presents a literature review of ionospheric scintillation monitoring methods. Two pertinent aspects are discussed: detection and characterization methods for ionospheric scintillation; and estimation of the scintillation signal.

1.3.1 Detection and characterization of ionospheric scintillation

The most prominent technique for ionospheric scintillation monitoring is based on the S_4 and σ_ϕ indices, which quantify the amplitude and phase fluctuations of the received signal, respectively, and were proposed by Dierendonck *et al.* (1993). Both indices have become standard metrics in ionospheric scintillation monitoring receivers (ISMRs) and underpinned newer algorithms and strategies. Appendix A provides a detailed description of these indices,

[2] In the data channel, the Costas phase-locked loop (PLL) is used as it is insensitive to half phase jumps induced the by the bit stream. In this case, the phase slips occur in half cycles ($\pm\pi$) instead of full cycles ($\pm 2\pi$).

[3] The term "drop lock" is usually preferred in the classical PLL literature, while "frequency unlock" is more suitable to digital PLL implementations as it is a more precise description (HUMPHREYS *et al.*, 2010a). On the other hand, "loss of lock" is a general term used whenever the receiver cannot recover the tracked phase anymore.

whereas this section focus on relevant advances reported in the literature.

While detection methods based on Neyman-Pearson (NP) with S_4 and σ_ϕ have been successfully implemented as an alarm mechanism, the adopted detrending methods have been a topic of debate in the last decades as they affect the observed value. A significant issue arises from the overlap[4] between the scintillation bandwidth and other impairments, leading to modifications in the indices depending on the defined cutoff frequency (FORTE; RADICELLA, 2002; BEACH, 2006; NIU *et al.*, 2012; NIU, 2012). Additionally, S_4 and σ_ϕ can also lead to false alarm episodes when multipath or strong interference is present. For these reasons, alternative approaches avoiding such indices have been proposed in the literature.

In Fu *et al.* (1999), several scintillation observables similar to S_4 were defined and decomposed using wavelet techniques, where it was assumed that the wavelet coefficients follow Gaussians distributions with the same variance but different means for scintillation and no scintillation hypotheses. Although the scintillation indices (and their detrending methods) are avoided, the raw carrier phase measurements are used as input data, which can be severely affected by cycle slips and loss of lock during intense scintillation events. More recently, Miriyala *et al.* (2015) proposed to evaluate the C/N_0 ratio by using complementary ensemble empirical mode decomposition in combination with multifractal detrended fluctuations analysis. However, it is well-known that the C/N_0 is not a reliable estimator when the signal experiences deep fading (JIAO *et al.*, 2016), and all mentioned algorithms make assumptions about the distribution, which leads to nonoptimized *ad hoc* thresholds.

To overcome such disadvantages, data-driven machine learning algorithms have been reported as methods for detection and characterization of scintillation. Jiao *et al.* (2017a) have proposed support vector machine (SVM) to perform supervised classification (or detection) of scintillation events from a real dataset, where the examples were labelled via visual inspection. The input vector was the estimated PSD of the raw signal intensity and, in some scenarios, also the maximum and mean values of S_4. This enabled the extraction of high-order moments of scintillation events, leading to an accuracy performance of around 95 % on the validation dataset, where the inclusion of S_4 did not necessarily increase the performance. This result surpassed the accuracy of traditional NP-based scintillation detectors operating with S_4 and σ_ϕ. Moreover, no prior distribution or detrending methods were required as the model extracts the features directly from the postcorrelated data. Once trained, such a model can be used as an automatic amplitude

[4] It is well known that the power spectral density (PSD) of oscillator noise of temperature compensated crystal oscillators (TCXOs) significantly overlaps the PSD of the scintillation phase (DIERENDONCK, 2005).

scintillation detector, operating in near real-time and in human-level performance. This approach had continuity in Liu *et al.* (2018) and in Jiao *et al.* (2017b), where both also indicate the viable application of the binary SVM classifier for the amplitude and phase scintillation detection. Other machine-learning techniques, such as decision tree, were also proposed in Linty *et al.* (2018), which indicate a similar accuracy performance, around 98 %.

Although the reported works have shown promising results using the postcorrelated data as input, the scintillation signal is not directly estimated. In other words, the methods proposed so far do not characterize the scintillation signal itself, but the disturbed correlator output containing scintillation-induced variations combined with other sources of impairments, geometry, and receiver-induced artifacts.

1.3.2 Estimation of the scintillation signal

Most of the initial attempts at monitoring scintillation via GNSS signals were experimentally deployed using traditional receivers designed for navigation purposes (DIERENDONCK *et al.*, 1993). The closed-loop tracking (CLT) architecture of such receivers is usually composed of PLL or frequency-locked loop (FLL) for carrier tracking, and delay-locked loop (DLL) for code tracking. These loops are designed to operate under nominal conditions, where the received signal is only impaired by thermal noise and line-of-sight (LOS) dynamics. However, under scintillation conditions, the tracking loop performance degrades significantly, specially for the carrier which is more sensitive to disturbances. An increased phase error leads the PLL to operate in its nonlinear region. In this case, due to the feedback mechanism, the tracked signal phase is not only corrupted by scintillation and other impairments, but also by receiver-induced signal processing artifacts generated by the PLL itself (XU; MORTON, 2018). Ultimately, this process causes cycle slips and, under intense and persistent conditions, loss of lock. Since the code loop is Doppler-aided by the carrier loop in GNSS receivers (JIAO, 2017), carrier loss of lock propagates to the code tracking, leading to a total loss of lock. As a consequence, the scintillation signal cannot be observed from the correlator output and the traditional scintillation indices become inaccurate. This limits the recent advances for detection and characterization of ionospheric scintillation, which still rely on the correlator output data to estimate the actual scintillation-induced variations. An additional step to obtain the scintillation signal is still required.

Driven by these limitations and the premise that navigation is not a goal for monito-

ring stations, a fundamental redesign of the GNSS receiver architecture has been proposed in the literature. Curran *et al.* (2014) has developed a new software-defined radio (SDR) receiver for scintillation monitoring, where the purpose of the signal processing chain is reconfigured to explore the geometry and time information and obtain the scintillation signal in open loop. In contrast to the traditional closed-loop operation, this receiver resigns its navigation capabilities as it would be a redundant task provided that the ground station position is known, fixed, and externally surveyed. Each sample from the data acquisition (DAQ) is associated with a timestamp, sourced from the local reference clock. On the one hand, an *a priori* clock error model is employed to correct biases between the local (*i.e.*, the receiver) and the GNSS reference clock. On the other hand, satellite clock errors are adjusted using its model based on the second-order polynomial equation, whereas the ephemeris-computed trajectory is used to estimate and wipe off the LOS phase from the incoming signal. While the feedforward processing of the open-loop tracking (OLT) architecture avoids the feedback artifacts, timing recovery is heavily dependent on clock models, whose efficacy is yet to be evaluated (XU; MORTON, 2018). To circumvent this problem, a hybrid approach based on a semi-open loop tracking (SOLT) architecture has been proposed by Xu e Morton (2018), where a CLT module is used in parallel to achieve a valid receiver time solution before initializing the SOLT system.

It is important to mention that the CLT approach is not undesirable for scintillation monitoring, as long as the scintillation-affected carrier and code phase can be tracked robustly. Although PLL, FLL, and DLL cannot provide that, advanced Kalman-based algorithms for carrier tracking have been proposed in the literature for reliable estimation of scintillation-affected carrier phase. Initial studies proposed a Kalman filter (KF)-based PLL to track the overall carrier phase (*i.e.*, combined scintillation, LOS dynamics, and other sources of impairments) (PSIAKI *et al.*, 2007; BARREAU *et al.*, 2012), as well as the extended Kalman filter (EKF) for joint code and phase tracking (PSIAKI; JUNG, 2002). Subsequently, the lowpass nature of the scintillation signal led to augmenting the state-space model (SSM) with an autoregressive (AR) process to model scintillation effects, which are then estimated by the KF (FOHLMEISTER *et al.*, 2018). Likewise, an augmented-SSM EKF was used to track both scintillation amplitude and phase by Vilà-Valls *et al.* (2015). These developments have led to more recent studies in which KF variants, such as adaptive Kalman filter (AKF) (LOCUBICHE-SERRA *et al.*, 2016; LOCUBICHE-SERRA *et al.*, 2021b) and the adaptive hard-limited KF (LOCUBICHE-SERRA *et al.*, 2021a), where the enhanced tracking robustness can be exploited to characterize

the scintillation signal directly from the estimated states (in case of the augmented SSM) or in postprocessing (when only the total carrier phase is tracked) (VILÀ-VALLS *et al.*, 2020; LOPES *et al.*, 2023b; FLORINDO; ANTREICH, 2024). However, these studies do not focus on scintillation monitoring *per se*, but rather on robust carrier tracking under scintillation conditions. Therefore, advanced tracking algorithms exploring the known and surveyed receiver-satellite geometry to extract the scintillation signal are still an open research topic.

1.4 Motivation and objectives

Considering the state of the art (SOTA) limitations in characterizing the ionospheric scintillation signal and the recent advances in estimating it from the postprocessed data, the main objective of the present thesis is to propose new methods for signal-level characterization of scintillation events. Instead of relying on S_4 and σ_ϕ and adopting an m-ary classification approach, the efforts are made on finding *where* the most discriminative features in the scintillation time series are located. The motivation for such an approach is to provide means for ionospheric scintillation monitoring stations to identify time series segments threatening the performance of GNSS receivers due to the presence of deep fades and fast phase variations.

Although empirical datasets are preferable for validating new characterization methods, the current deployment of ISMRs *in situ* still rely on classical CLT structures that distort the scintillation signal (SEPTENTRIO, 2018; VALLEY, 2017). Although newer strategies to obtain the scintillation signal from OLT and SOLT are reported in the literature (CURRAN *et al.*, 2014; XU; MORTON, 2018), such architectures are not widely adopted yet and the available datasets thus processed are scarce. Due to this technical limitation, the present thesis employs well-accepted scintillation models to generate synthetic datasets for validating the proposed characterization methods.

To achieve the main objective, two specific objectives are defined:

1. **Simulation of scintillation signals**: two models generate synthetic datasets for validating the proposed methods. First is the Cornell scintillation model (CSM), which allows low-complexity simulation of the diffractive patterns but ignores refractive effects from large-scale irregularities (JIAO *et al.*, 2018). Therefore, a physics-based model, originally named Two-component power-law phase-screen model (TPPSM) and based on phase screen theory (JIAO *et al.*, 2018; XU *et al.*, 2020), is used as basis for the CPSSM, from

which scintillation time series are generated in both MF and MC scenarios, contemplating diffractive and refractive effects.

2. **Characterization of scintillation signals**: the thesis proposes new CNN-based methods for detecting and characterizing scintillation events. Initial work uses the CSM for *m*-ary classification, and subsequent architectures provide sample-level characterization under CPSSM in MF and MC scenarios, overcoming current SOTA limitations.

The motivation in exploring CNN-based methods for scintillation characterization stems from their successful application in image processing and computer vision. Notably, time series and images share a common structural property: both constitute ordered data in either the spatial or temporal dimension. This similarity has enabled the successful transfer of contemporary pattern recognition techniques from image processing domains to time series analysis (FAWAZ *et al.*, 2019). Evidence indicates that interpretability methods for temporal data achieve enhanced performance when time series are reformulated as image-like representations (ISMAIL *et al.*, 2020). Despite these promising developments, numerous time series applications remain underexploiting this potential. Notably, semantic segmentation methods in computer vision demonstrate superior capabilities for identifying and characterizing localized spatial features, whereas time series classification (TSC) has conventionally depended on global descriptors such as higher-order statistical moments (*e.g.*, S_4 and σ_ϕ). This methodological gap is particularly concerning for ionospheric scintillation monitoring, where perturbations exhibit pronounced dynamic and nonstationary behavior, leading to insufficient signal interpretation. Thus, feature attribution analysis, manifested as activation maps indicating which signal samples drive classification outcomes, provides this requisite diagnostic information.

1.5 Contributions

The following journal article is derived from this thesis:

1. Pacelli, Rubem Vasconcelos; Florindo, Rodrigo de Lima; Antreich, Felix; de Lucena, Antônio Macilio Pereira. "An All-Digital Coherent AFSK Demodulator for CubeSat Applications," *Digital Signal Processing*, vol. 162, p. 105147, Jul. 2025 (PACELLI *et al.*, 2025a).

The following journal article has been submitted to the GPS Solutions and is under review at the time of writing:

1. Pacelli, Rubem Vasconcelos; Florindo, Rodrigo de Lima; Antreich, Felix; Aragon-Angel,

Angela; Rovira-Garcia, Adria; Ferrer, André Lima Ferrer. "Characterizing Equatorial Scintillation Signals Using Dimensional-Wise Convolutional Neural Networks and Class Activation Maps," *GPS Solutions*, submitted in Nov. 2025.

The following conference proceeding articles are derived from this thesis:

1. Pacelli, Rubem Vasconcelos; Florindo, Rodrigo de Lima; Antreich, Felix; de Almeida, André Lima Ferrer; Aragon-Angel, Angela; Garcia, Adrià Rovira. "Characterization of Ionospheric Scintillation Using Deep Learning Models," in *Proc. 38th International Technical Meeting of the Satellite Division of The Institute of Navigation (ION GNSS+ 2025)*, pp. 3339–3352, Sep. 2025 (PACELLI *et al.*, 2025b).
2. Pacelli, Rubem Vasconcelos; Aragon-Angel, Angela; García, Adrià Rovira; de Almeida, Andre Lima Ferrer; Antreich, Felix. "Convolutional Neural Networks for Time Series Classification of Ionospheric Scintillation," in *Proc. 37th International Technical Meeting of the Satellite Division of The Institute of Navigation (ION GNSS+ 2024)*, pp. 3019–3028, Sep. 2024 (PACELLI *et al.*, 2024).
3. Florindo, Rodrigo de Lima; Pacelli, Rubem; Ferreira, Thiago Lobo; Silva, Daniele Oliveira; de Lucena, Antonio Macilio Pereira; Antreich, Felix. "Advanced Kalman Filter Carrier Tracking: Performance Assessment Under Two Ionospheric Scintillation Models," in *Proc. 38th International Technical Meeting of the Satellite Division of The Institute of Navigation (ION GNSS+ 2025)*, pp. 3421–3435, Sep. 2025 (FLORINDO *et al.*, 2025).

1.6 Thesis outline

The present thesis is organized as follows:

1. In Chapter 2, the channel and received GNSS signal modeling are presented.
2. Chapter 3 discusses the two scintillation models used in this thesis;
3. In Chapter 4, CNN-based methods for scintillation detection and characterization are proposed.
4. Chapter 5 presents the numerical results of the proposed characterization methods on synthetic and real scintillation datasets.
5. Finally, in Chapter 6, the main conclusions of this thesis are drawn, and some future research directions are suggested.

1.7 Notation

Continuous- and discrete-time signals are denoted using parentheses and brackets, respectively; for example, $a(t)$ and $a[n]$ represent a continuous-time signal and its discrete-time version at a given sampling instant. Ordered discrete sequences without temporal support also use brackets, and commas separate their elements. Scalars are indicated by nonbold letters ($a, \ldots, A, \ldots, \mathcal{A}, \ldots$), vectors by bold lowercase letters ($\mathbf{a}, \ldots$), matrices by bold uppercase letters ($\mathbf{A}, \ldots$), tensors by uppercase calligraphic bold letters ($\boldsymbol{\mathcal{A}}, \ldots$), and sets by uppercase calligraphic letters ($\mathcal{A}, \ldots$). Any-order tensor indexing follows the convention defined by Kolda e Bader (2009). Other operators and notation are defined as they appear in the text.

2 SIGNAL MODEL

This chapter addresses the following questions:

1. How to model the received baseband (BB) GNSS signal in the presence of ionospheric scintillation?
2. What postprocessing techniques are applied to extract scintillation information from the received signal?

We begin with a wideband radio frequency (RF) signal model that captures the main channel impairments and derive the simplified BB model used in this thesis, which retains only scintillation-induced variations and noise. The final section states the postprocessing assumptions.

2.1 GNSS signal model

Let $N_\mathrm{c} \in \mathbb{N}$ be the number of signals processed in parallel by the receiver channels. Each channel is defined as a unique combination of pseudorandom (PR) code and carrier frequency of the target satellite signal. Assuming a generic GNSS signal based on quadrature phase-shift keying (QPSK) modulation[1] (TEUNISSEN; MONTENBRUCK, 2017, p. 403), the transmitted signal can be expressed as

$$s_\mathrm{RF}(t,n_\mathrm{c}) = \sqrt{2P}\,\mathrm{Re}\Big\{ s(t,n_\mathrm{c})\, e^{j2\pi f_\mathrm{c} t} \Big\}, \tag{2.1}$$

where $P \in \mathbb{R}_+$ is the transmitted signal power [W] (assumed constant for all satellites), $s(t,n_\mathrm{c}) \in \mathbb{C}$ is the unity-power lowpass equivalent of $s_\mathrm{RF}(t,n_\mathrm{c})$, and $f_\mathrm{c} \in \mathbb{R}_+$ is the carrier frequency [Hz] associated with the n_cth channel, with $n_\mathrm{c} \in \{1,2,\ldots,N_\mathrm{c}\}$.

The most general complex envelope of a GNSS signal contains in-phase and quadrature components:

$$s(t,n_\mathrm{c}) = c_\mathrm{i}(t,n_\mathrm{c})\, d_\mathrm{i}(t,n_\mathrm{c}) + j c_\mathrm{q}(t,n_\mathrm{c})\, d_\mathrm{q}(t,n_\mathrm{c}), \tag{2.2}$$

where $d_\mathrm{i}(t,n_\mathrm{c}), d_\mathrm{q}(t,n_\mathrm{c}) \in \mathbb{R}$ are the navigation message symbols[2], $c_\mathrm{i}(t,n_\mathrm{c}), c_\mathrm{q}(t,n_\mathrm{c}) \in \mathbb{R}$ are the spreading waveforms, and the subscripts $\cdot_\mathrm{i}$ and $\cdot_\mathrm{q}$ indicate whether the signals refer to the real or imaginary part, respectively. Because the present signal model assumes data-only signals,

[1] Even for modulation schemes not covered by QPSK, such as alternative BOC (AltBOC) or code shift key (CSK), the signal has a similar structure.

[2] ± 1 for data channels and $+1$ for pilot channels.

the quadrature component is omitted (TEUNISSEN; MONTENBRUCK, 2017, p. 403), and the lowpass equivalent simplifies to $s(t,n_c) = c(t,n_c)\,d(t,n_c) \in \mathbb{R}$, with $d_i(t,n_c) \triangleq d(t,n_c)$, and

$$c_i(t,n_c) \triangleq c(t,n_c) = \sum_{i\in\mathbb{Z}} c\left[i \bmod N_{cp}, n_c\right] p\left(t - iT_{cp}, n_c\right), \tag{2.3}$$

where mod is the modulo operator and $c[0,n_c], c[1,n_c], \cdots, c\left[N_{cp}-1,n_c\right]$ is the chip sequence for a given PR code. The value $c[i,n_c] \in \{-1,1\}$ is obtained every $T_{cp} \in \mathbb{R}$ seconds and repeated every $N_{cp} \in \mathbb{N}$ chips. The signal $p(t,n_c) \in \mathbb{R}$ is the chip pulse shape, which is assumed here to be defined in $\left[0,T_{cp}\right)$. Hence, the period of $c(t,n_c)$ is $T_{cp}N_{cp}$ seconds.

The transmitted signal can be rewritten as

$$s_{RF}(t,n_c) = \sqrt{2P}\,s(t,n_c)\cos(2\pi f_c t). \tag{2.4}$$

The propagation channel for GNSS signals can be divided into three main parts: the exosphere (*i.e.*, outer space), the ionosphere, and the troposphere (which also accounts for effects from the stratosphere). Any other effects, such as those caused by the plasmasphere or magnetosphere, are not considered in this propagation channel. The exosphere is a vacuum medium and can be assumed to affect the signal only through free-space path loss. The troposphere is nondispersive for frequencies up to 15 GHz (SUBIRANA *et al.*, 2013, Section 5.4.2), meaning that the group delay is constant over this range, or equivalently, the transfer function phase response is linear in frequency (LATHI, 2010, Section 3.4.2). Moreover, scattering effects in the troposphere are considered negligible (FOHLMEISTER *et al.*, 2018, Section 2.1) (HOFMANN-WELLENHOF *et al.*, 2008, Section 5.3.3). In contrast, the ionosphere is dispersive, so the code and carrier phase propagate at different speeds. Their velocities depend on the carrier frequency. In addition to the refractive effect from the stable ionospheric part, scintillation can occur in the equatorial region due to plasma irregularities with a scale size lower than or comparable to the dimension of the first Fresnel zone, that may cause deep fades and rapid phase fluctuations in GNSS signals.

Based on this discussion, the wideband RF signal at the receiver antenna is modeled as[3]

$$\begin{aligned} r_{RF}(t) = \sum_{n_c=1}^{N_c} \gamma_T(t,n_c)\, s\left(t - \tau_T(t,n_c), n_c\right) \cos\left[2\pi f_c\left(t - \tau_{LOS}(t,n_c)\right) + \phi_{atm}(t,n_c)\right] \\ + \eta_{RF}(t). \end{aligned} \tag{2.5}$$

[3] A constant phase representing the initial offset between transmitter and receiver carrier should be inserted in (2.5) but was set to zero for the sake of simplicity.

The amplitude $\gamma_{\mathrm{T}}(t,n_{\mathrm{c}}) \in \mathbb{R}$ models the envelope variations caused by the channel, including free-space path loss and scintillation-induced amplitude fluctuations. The term $\phi_{\mathrm{atm}}(t,n_{\mathrm{c}}) \in \mathbb{R}$ accounts for atmospheric phase effects [rad] from the ionosphere, troposphere, and stratosphere. The noise $\eta_{\mathrm{RF}}(t)$ is zero-mean, real-valued additive white Gaussian noise (AWGN) with two-sided PSD $N_0/2 \in \mathbb{R}$, where N_0 is the noise power spectral density [W/Hz]. The total code delay [s] is denoted as $\tau_{\mathrm{T}}(t,n_{\mathrm{c}}) \in \mathbb{R}_+$. The LOS delay, $\tau_{\mathrm{LOS}}(t,n_{\mathrm{c}}) = \rho_{\mathrm{s,g}}(t,n_{\mathrm{c}})/c_0 \in \mathbb{R}_+$, is the time taken by the signal to travel from the satellite to the receiver through free space, where $\rho_{\mathrm{s,g}}(t,n_{\mathrm{c}}) \in \mathbb{R}_+$ is the true geometric range [m] and $c_0 \in \mathbb{R}_+$ is the speed of light in vacuum [m/s].

By analyzing the evolution of the received carrier argument in (2.5) from the instant t_{a}, it follows that[4]

$$
\begin{aligned}
&2\pi f_{\mathrm{c}}(t-\tau_{\mathrm{LOS}}(t,n_{\mathrm{c}})) + \phi_{\mathrm{atm}}(t,n_{\mathrm{c}}) \\
&= 2\pi f_{\mathrm{c}}\left(t - \tau_{\mathrm{LOS}}(t_{\mathrm{a}},n_{\mathrm{c}}) - \int_{t_{\mathrm{a}}}^{t} \frac{\partial \tau_{\mathrm{LOS}}(u,n_{\mathrm{c}})}{\partial u}\,\mathrm{d}u\right) + \phi_{\mathrm{atm}}(t,n_{\mathrm{c}}) \\
&= 2\pi f_{\mathrm{c}} t + \underbrace{2\pi \int_{t_{\mathrm{a}}}^{t} f_{\mathrm{D}}(u,n_{\mathrm{c}})\,\mathrm{d}u + \phi_{\mathrm{LOS}}(t_{\mathrm{a}},n_{\mathrm{c}}) + \phi_{\mathrm{atm}}(t,n_{\mathrm{c}})}_{=\phi_{\mathrm{T}}(t,n_{\mathrm{c}})},
\end{aligned}
\tag{2.6}
$$

where $f_{\mathrm{D}}(u,n_{\mathrm{c}}) = -f_{\mathrm{c}}\frac{\partial \tau_{\mathrm{LOS}}(u,n_{\mathrm{c}})}{\partial u}$ is the Doppler frequency [Hz], which is being integrated in the interval $[t_{\mathrm{a}},t]$, and

$$
\begin{aligned}
\phi_{\mathrm{LOS}}(t_{\mathrm{a}},n_{\mathrm{c}}) = &= -2\pi f_{\mathrm{c}}\frac{\rho_{\mathrm{s,g}}(t_{\mathrm{a}},n_{\mathrm{c}})}{c_0} = -2\pi f_{\mathrm{c}}\tau_{\mathrm{LOS}}(t_{\mathrm{a}},n_{\mathrm{c}}) \\
&= -2\pi f_{\mathrm{c}}\int_{t_{\mathrm{t}}}^{t_{\mathrm{a}}} \frac{\partial \tau_{\mathrm{LOS}}(u,n_{\mathrm{c}})}{\partial u}\,\mathrm{d}u = 2\pi\int_{t_{\mathrm{t}}}^{t_{\mathrm{a}}} f_{\mathrm{D}}(u,n_{\mathrm{c}})\,\mathrm{d}u
\end{aligned}
\tag{2.7}
$$

is the accumulated LOS phase due to Doppler over the interval $(t_{\mathrm{t}},t_{\mathrm{a}})$, where t_{t} is the transmission time, defined as $s(t,n_{\mathrm{c}}) = 0\,\forall\, n_{\mathrm{c}} \in \{1,2,\cdots,N_{\mathrm{c}}\}, t < t_{\mathrm{t}}$ (we assume that all signals are transmitted at t_{t}). The signal $\phi_{\mathrm{T}}(t,n_{\mathrm{c}}) \in \mathbb{R}$ represents the total (atmospheric + geometric) phase variation [rad] during the interval $[t_{\mathrm{t}},t]$.

Let us analyze the evolution of $\phi_{\mathrm{T}}(t,n_{\mathrm{c}})$ within the kth correlation interval, that is, $t_{\mathrm{a}} \triangleq kT$ and $t \in [kT,(k+1)T)$, where $T \in \mathbb{R}_+$ is the correlation interval. By assuming that the

[4] Under this formulation, one can state that the phase-based ranging problem boils down to estimating $\phi_{\mathrm{T}}(t,n_{\mathrm{c}})$ unwrapped, *i.e.*, with the initial full-cycle ambiguity solved. On the one hand, standard carrier tracking loops based on PLLs and/or FLLs lock initially onto the fractional part of $\phi_{\mathrm{T}}(t,n_{\mathrm{c}}) \in \mathbb{R}$, but maintain this phase unwrapped and precisely estimated provided that no cycle slips occur. On the other hand, the initial full-cycle ambiguity is solved by the navigation data processor with a positioning algorithm, such as precise point positioning (PPP) or real-time kinematics (RTK), while nongeometric phase contributions are modeled and removed from $\phi_{\mathrm{T}}(t,n_{\mathrm{c}})$ to obtain $\phi_{\mathrm{LOS}}(t,n_{\mathrm{c}})$, from where the true range is calculated.

Doppler frequency is constant for this interval, from (2.6), we have that

$$\phi_{\mathrm{T}}(t,n_{\mathrm{c}}) = 2\pi f_{\mathrm{D}}[k,n_{\mathrm{c}}](t-kT) + \phi_{\mathrm{LOS}}(kT,n_{\mathrm{c}}) + \phi_{\mathrm{atm}}(t,n_{\mathrm{c}}), \tag{2.8}$$

where $f_{\mathrm{D}}[k,n_{\mathrm{c}}] \triangleq f_{\mathrm{D}}(kT,n_{\mathrm{c}})$.

2.2 Receiver RF-FE and signal conditioning

The first structure that captures and processes the transmitted signal at the receiver is the radio frequency front end (RF-FE), which comprises the receiver antenna, low noise amplifiers (LNAs), RF and intermediate frequency (IF) filters, a local oscillator (LO), mixers, an automatic gain control (AGC), and an analog-to-digital converter (ADC). This set of components conditions the received signal in the analog domain for subsequent digital processing. Modern GNSS receivers based on the SDR concept aim to minimize analog preprocessing to obtain digital samples as early as possible. While different architectures can be used to achieve this goal (BETZ, 2015, Section 14.3), Figure 5 shows an RF-FE example that adopts a single-stage superheterodyne architecture, which is still widely adopted in modern receivers due to its good selectivity[5] and sensitivity[6] characteristics.

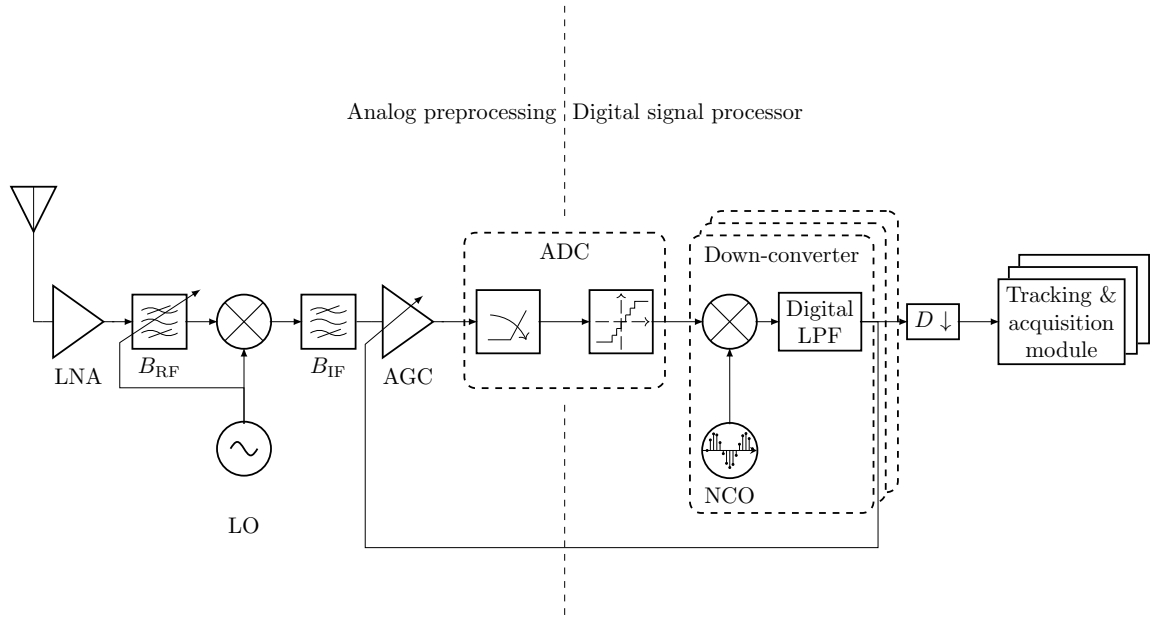

Figura 5 – Block diagram of the GNSS receiver.

[5] Ability to suppress closely-spaced signals in frequency.
[6] Ability to detect weak signals.

The low-power[7] wideband signal captured by the antenna is amplified by an LNA, and an analog bandpass filter with tunable center frequency of $f_{\mathrm{RF}} \in \mathbb{R}$ and one-sided bandwidth of $B_{\mathrm{RF}} \in \mathbb{R}$ suppresses out-of-band interference. A frequency synthesizer uses the LO as reference to generate a carrier tuned at f_{RF}, which is mixed with the RF signal to shift it from f_{c} to $f_{\mathrm{IF}} \in \mathbb{R}$ (usually $f_{\mathrm{c}} \gg f_{\mathrm{IF}}$). Depending whether $f_{\mathrm{RF}} = f_{\mathrm{c}} \pm f_{\mathrm{IF}}$, components around $f_{\mathrm{im}} = f_{\mathrm{c}} \pm 2f_{\mathrm{IF}}$ are also translated to IF if the RF filter does not suppress them. To keep the frequency ratio small, one can opt to the high-side tuning[8] of the RF stage, *i.e.*, $f_{\mathrm{RF}} = f_{\mathrm{c}} + f_{\mathrm{IF}}$. In this case, to remove the image frequency, we have that $f_{\mathrm{RF}} + \frac{B_{\mathrm{RF}}}{2} < f_{\mathrm{im}} = f_{\mathrm{RF}} + f_{\mathrm{IF}} \therefore B_{\mathrm{RF}} < 2f_{\mathrm{IF}}$. Although the frequency synthesizer can generate a range of frequencies as a ratio of the LO frequency, we assume that f_{RF} is kept fixed.

Afterwards, a high Q-factor[9] analog filter with bandwidth $B_{\mathrm{IF}} \in \mathbb{R}$ and nontunable center frequency at f_{IF} is employed to eliminate the intermodulation product generated by the mixing between the RF local carrier and the filtered signal. The bandwidth B_{IF} must be narrow enough to reject the intermodulation product but wide enough to capture all the N_{c} signals over the frequencies of interest.

Classical superheterodyne receivers continue processing the IF signal in the analog domain until BB sampling, whereas modern SDR-based receivers sample the signal directly at IF using a high-sampling rate. This step is supported by a closed-loop AGC circuit that maintains the signal amplitude within the full-scale level of the ADC. The conditioned signal is then sampled and quantized. We assume that the ADC has sufficient resolution so that quantization errors are negligible and that its sampling rate satisfies the Nyquist sampling criterion. A digital downconverter then shifts the signal from IF to BB using a numerically-controlled oscillator (NCO) and a digital lowpass filter (LPF). The BB signal is decimated so that the sampling rate $f_{\mathrm{s}} \in \mathbb{R}$ satisfies $f_{\mathrm{s}} \geq 2B_{\max}$, where $B_{\max} \in \mathbb{R}_{+}$ is the maximum one-sided bandwidth among all BB signals processed by the receiver.. To handle MF signals in parallel, the receiver uses a set of down-converters, each tuned to a carrier frequency, to split the wideband into N_{f} narrowband

[7] The effective earthward power is about 500 W, but the received power is on the order of 10^{-16} W (MISRA; ENGE, 2006, p. 431).

[8] High-side tuning leads to a lower $f_{\mathrm{RF,min}}/f_{\mathrm{RF,max}}$ ratio, where $f_{\mathrm{RF,min}} \leq f_{\mathrm{RF}} \leq f_{\mathrm{RF,max}}$. This is preferable as a large frequency ratio makes the frequency synthesizer's RF circuit more complex and costly to implement (ZIEMER; TRANTER, 2006, Section 3.5).

[9] The quality factor (Q-factor) is defined as 2π times the ratio of stored to dissipated energy per cycle (HAYKIN; MOHER, 2006, p. 178). While this definition is useful for resonators, in RF filter design Q is more commonly expressed as the ratio between center frequency and bandwidth, serving as figure of merit for frequency selectivity (ZIEMER; TRANTER, 2006, p. 107). Note, however, that the Q factor is rigorously defined only for resonators. For filters, it is only an approximation (GREEN, 1955).

signals in BB, where $N_{\mathrm{f}} \in \mathbb{N}$ is the number of frequencies processed simultaneously by the receiver.

The whole system including the RF-FE, ADC, NCOs, and digital LPFs is referred to as the DAQ module, which streams N_{f} digital signals. Each one is expressed as

$$r[n,n_{\mathrm{f}}] = \sum_{n_{\mathrm{c}} \in \mathcal{S}_{n_{\mathrm{f}}}} A[k,n_{\mathrm{c}}]\, s(nT_{\mathrm{s}} - \tilde{\tau}_{\mathrm{T}}[k,n_{\mathrm{c}}], n_{\mathrm{c}})\, e^{j\tilde{\phi}_{\mathrm{T}}[n,n_{\mathrm{c}}]} + \eta[n,n_{\mathrm{f}}], \tag{2.9}$$

where $T_{\mathrm{s}} = 1/f_{\mathrm{s}} \in \mathbb{R}$ is the sampling interval that defines n, $A[k,n_{\mathrm{c}}] \in \mathbb{R}$ is the signal amplitude after the conditioning stage, and $n_{\mathrm{f}} \in \{1,2,\cdots,N_{\mathrm{f}}\}$. Let $N = T/T_{\mathrm{s}} \in \mathbb{N}$ be the number of samples within the correlation interval, where N is an integer multiple of N_{cp}. Then, $n \in \{kN, kN+1, \ldots, (k+1)N-1\}$ for the time interval $[kT, (k+1)T)$. The set denoted as $\mathcal{S}_{n_{\mathrm{f}}} \subset \{1,2,\cdots,N_{\mathrm{c}}\}$ contains the indices of the signals that are present in the n_{f}th narrowband coming from the DAQ.

The stochastic process $\eta(t,n_{\mathrm{f}}) \in \mathbb{C}$ is the BB equivalent of $\eta_{\mathrm{IF}}(t) \in \mathbb{R}$, which in turn is the band-limited version of $\eta_{\mathrm{RF}}(t)$ within $|f \pm f_{\mathrm{IF}}| \leq B_{\max}$. The signal $\eta_{\mathrm{IF}}(t)$ models Gaussian noise at the ADC input. Therefore, $\eta[n,n_{\mathrm{f}}] \triangleq \eta(nT_{\mathrm{s}}, n_{\mathrm{f}})$ in (2.9) is its nth noise sample, representing additive fluctuations caused by Johnson-Nyquist (*i.e.*, thermal) and other receiver electronic noise, which corrupts the n_{f}th narrowband signal. A statistical analysis of $\eta[n,n_{\mathrm{f}}]$ is provided in Appendix B. Although the discrete-time noise in (2.9) comes from $\eta_{\mathrm{RF}}(t)$, which is statistically equivalent for all frequencies, we maintain the dependence on n_{f} in $\eta[n,n_{\mathrm{f}}]$ to account for the fact that the noise power may vary due to differences in the frequency response of the RF-FE or due to the presence of other frequency-dependent interferences arisen from the receiver circuit, before the signal is digitalized.

Under the argument that the correlation will perform the code division multiple access (CDMA) separation for each overlapping BB signal in the n_{f}th frequency narrowband, let us focus on a single overall phase of the n_{c}th channel in (2.9). It can be decomposed as

$$\tilde{\phi}_{\mathrm{T}}[n,n_{\mathrm{c}}] = \phi_{\mathrm{T}}[n,n_{\mathrm{c}}] + \phi_{\mathrm{osc,gnd}}[k] + \phi_{\mathrm{osc,sat}}[k,n_{\mathrm{c}}], \tag{2.10}$$

where

$$\begin{aligned}\phi_{\mathrm{T}}[n,n_{\mathrm{c}}] =& 2\pi\tilde{f}_{\mathrm{D}}[k,n_{\mathrm{c}}](nT_{\mathrm{s}} - kT) + \phi_{\mathrm{LOS}}[k,n_{\mathrm{c}}] + \phi_{\mathrm{atm}}[k,n_{\mathrm{c}}] \\ =& 2\pi\tilde{f}_{\mathrm{D}}[k,n_{\mathrm{c}}](nT_{\mathrm{s}} - kT) + \phi[k,n_{\mathrm{c}}],\end{aligned} \tag{2.11}$$

with

$$\phi_{\mathrm{LOS}}[k,n_{\mathrm{c}}] \triangleq \phi_{\mathrm{LOS}}(kT,n_{\mathrm{c}}), \tag{2.12}$$

$$\phi_{\mathrm{atm}}[k,n_{\mathrm{c}}] \triangleq \phi_{\mathrm{atm}}(kT,n_{\mathrm{c}}), \tag{2.13}$$

$$\phi[k,n_{\mathrm{c}}] \triangleq \phi_{\mathrm{LOS}}[k,n_{\mathrm{c}}] + \phi_{\mathrm{atm}}[k,n_{\mathrm{c}}]. \tag{2.14}$$

Although omitted in Figure 5 and for the sake of clarity, the monitoring station adopts an external LO that provides a ideally pure sinusoidal reference to the frequency synthesizer, which controls the clock signal of the ADC, generates the carrier frequency used by the RF stage (f_{RF}), and drives all other frequency- and time-dependent processes within the receiver (BETZ, 2015, Section 14.1). Additionally, we assume that the local reference time is GNSS-disciplined. In this setup, the receiver generates a 1-Hz pulse-per-second (1PPS) signal synchronized with the GNSS reference time, *i.e.*, shifted by the receiver clock bias (computed by the navigation data processor). A second 1PPS signal is locally generated by the frequency synthesizer (without any time shift). The phase difference between them feeds back through a control loop to align the 1PPS signal (and all other outputs) generated by the frequency synthesizer with the 1PPS signal generated by the receiver (LOMBARDI, 2008). As a result, the SDR can assign an absolute GNSS-referenced timestamp to every sample delivered by the DAQ. For this reason, in (2.8), no distinction is made between the time readings generated by the ground station and satellite clocks with respect to the GNSS reference time. In other words, everything is referenced to the same temporal support, t, as if the timing of the satellite and ground station were perfectly synchronized to the system time. However, reference LO is not perfect and introduces two main impairments: (i) a long-term drifting behavior, primarily caused by external effects such as aging and temperature variations. It adds a deterministic frequency deviation to the oscillator frequency, making the ADC sampling instants deviate from their correct values; (ii) phase noise, defined as small and short-term random fluctuations and caused by imperfections in the internal oscillator circuitry, introducing noise in the amplitude and frequency (*i.e.*, jitter) of the ideal sinusoidal signal generated by the oscillator. (BORRE *et al.*, 2022, Section 11.2.2). The same nonidealities also affect the satellite oscillator, which is used to generate the carrier frequency (*e.g.*, L1/E1, L2, *etc.*) transmitted to the ground station.

For the phase, these impairments are incorporated into (2.10) as $\phi_{\mathrm{osc,gnd}}[k]$ and $\phi_{\mathrm{osc,sat}}[k,n_{\mathrm{c}}]$ for the ground station[10] and satellite clocks, respectively. For the code delay, they

[10] The index n_{c} does not exist for the clock error of the ground station because every time and frequency reference

are introduced in (2.9) as follows

$$\tilde{\tau}_{\mathrm{T}}[k,n_{\mathrm{c}}] = \tau_{\mathrm{T}}[k,n_{\mathrm{c}}] + \tau_{\mathrm{osc,gnd}}[k] + \tau_{\mathrm{osc,sat}}[k,n_{\mathrm{c}}], \tag{2.15}$$

where $\tau_{\mathrm{osc,gnd}}[k], \tau_{\mathrm{osc,sat}}[k,n_{\mathrm{c}}] \in \mathbb{R}$ are the clock error signal for the ground station and satellite, respectively, and $\tau_{\mathrm{T}}[k,n_{\mathrm{c}}] \triangleq \tau_{\mathrm{T}}(kT,n_{\mathrm{c}})$.

Additionally, the carriers synthesized by the satellite and ground station were assumed to be perfectly tuned to the nominal carrier frequency, f_{c}, which is not true in practice. Hence, the frequency shifting and drifting caused by the nonideal oscillators is inserted into (2.11) as follows

$$\tilde{f}_{\mathrm{D}}[k,n_{\mathrm{c}}] = f_{\mathrm{D}}[k,n_{\mathrm{c}}] + f_{\mathrm{osc,gnd}}[k] + f_{\mathrm{osc,sat}}[k,n_{\mathrm{c}}], \tag{2.16}$$

where $f_{\mathrm{osc,gnd}}[k,n_{\mathrm{c}}], f_{\mathrm{osc,sat}}[k,n_{\mathrm{c}}] \in \mathbb{R}$ are the clock error signal for the Doppler shift for the ground station and the satellite, respectively.

Finally, substituting (2.11) into (2.10) leads to

$$\tilde{\phi}_{\mathrm{T}}[n,n_{\mathrm{c}}] = 2\pi\tilde{f}_{\mathrm{D}}[k,n_{\mathrm{c}}](nT_{\mathrm{s}} - kT) + \tilde{\phi}[k,n_{\mathrm{c}}], \tag{2.17}$$

where

$$\tilde{\phi}[k,n_{\mathrm{c}}] = \phi[k,n_{\mathrm{c}}] + \phi_{\mathrm{osc,gnd}}[k] + \phi_{\mathrm{osc,sat}}[k,n_{\mathrm{c}}]. \tag{2.18}$$

Note that the code delay, frequency, amplitude, clock errors, and atmospheric carrier phase are all time-indexed using k, the correlation index, since all of them are considered to be constant over the correlation interval.

2.3 Acquisition module

The set $\{r[n,n_{\mathrm{f}}]\}_{n_{\mathrm{f}}=1}^{N_{\mathrm{f}}}$ feeds the correlator bank, the main and most energy-consuming component of the digital signal processor. Each correlator channel processes a single narrowband signal and is assigned to a unique combination of satellite PR code and carrier frequency. In the case of multiple satellites in one narrowband signal, the same is replicated and forwarded to different correlator channels. Each correlator multiplies the incoming signal by a local replica containing the target satellite PR code and the estimated signal parameters (code delay and

is assumed to be sourced by the same external LO. Hence, the clock error signal is assumed to be common for all channels.

carrier phase). The estimation of the parameters are performed by the acquisition and tracking modules, whose operation alternates depending on whether the satellite is locked or not.

For the acquisition module, the correlator bank is used to perform a time-frequency search and produce the Doppler-delay map (DDM), from which the coarse estimations of code delay and Doppler frequency are extracted. If the n_{f}th narrowband signal is assigned to the n_{c}th correlator channel, then the correlator takes N samples from $r[n,n_{\mathrm{f}}]$ and multiplies them with[11]

$$c\left(iT_{\mathrm{s}}-\hat{\tau}_{\mathrm{T}},n_{\mathrm{c}}\right)e^{-2\pi\hat{f}_{\mathrm{D}}iT_{\mathrm{s}}}\;\forall\, i\in\{0,1,\ldots N-1\}\,. \tag{2.19}$$

In this thesis, the hat notation indicates estimates of true values. The acquisition module evaluates the DDM to identify the set $\{\hat{\tau}_{\mathrm{T}},\hat{f}_{\mathrm{D}}\}$ that raises the correlator output above the noise floor the most. Once found, the signal is considered acquired (*i.e.*, the satellite is locked), and the corresponding set provides coarse initial estimates. The digital signal processor then switches to tracking mode for that channel.

2.4 Tracking module

The tracking module provides fine estimates of the code delay, carrier phase, and Doppler frequency, by using the coarse estimates obtained from the acquisition module as initial condition. In the present thesis, due to specific focus on characterization of ionospheric scintillation, it is assumed that the refined code ($\hat{\tau}_{\mathrm{T}}[k,n_{\mathrm{c}}]$) and carrier ($\hat{\phi}[k,n_{\mathrm{c}}]$ and $\hat{f}_{\mathrm{D}}[k,n_{\mathrm{c}}]$) estimates are obtained at each correlation interval by a CLT architecture, which is discussed in Section 2.5.

For $n\in\{kN,kN+1,\ldots,(k+1)N-1\}$, the argument of the carrier replica, $\hat{\phi}_{\mathrm{T}}[n,n_{\mathrm{c}}]$ is generated from the estimates $\hat{\phi}[k,n_{\mathrm{c}}]$ and $\hat{f}_{\mathrm{D}}[k,n_{\mathrm{c}}]$ as follows[12]

$$\hat{\phi}_{\mathrm{T}}[n,n_{\mathrm{c}}]=2\pi\hat{f}_{\mathrm{D}}[k,n_{\mathrm{c}}]\left(nT_{\mathrm{s}}-kT\right)+\hat{\phi}[k,n_{\mathrm{c}}]\,. \tag{2.20}$$

The kth output of the postcorrelated signal can be expressed as

$$y[k,n_{\mathrm{c}}]=\frac{1}{N}\sum_{n=kN}^{(k+1)N-1}r[n,n_{\mathrm{f}}]\,c\left(nT_{\mathrm{s}}-\hat{\tau}_{\mathrm{T}}[k,n_{\mathrm{c}}]\right)e^{-j\hat{\phi}_{\mathrm{T}}[n,n_{\mathrm{c}}]} \tag{2.21}$$

[11] In the cold start, one can only obtain the code phase in the interval $[0,T_{\mathrm{cp}}N_{\mathrm{cp}})$. However, the acquisition step is readily followed by frame synchronization, which allows to disambiguate the total code delay over multiple code periods (KAPLAN; HEGARTY, 2017, Section 8.10.1). Here, for the sake of simplicity, we denote the total code delay estimate straightforwardly.

[12] Before starting the next correlation interval, the receiver updates the carrier phase estimate as $\hat{\phi}[k+1,n_{\mathrm{c}}]=\hat{\phi}[k,n_{\mathrm{c}}]+2\pi\hat{f}_{\mathrm{D}}[k,n_{\mathrm{c}}]\,T$ to account for the phase evolution during the previous correlation interval. This step prevents abrupt phase jumps at the beginning of each new interval.

Note that $r[n,n_{\mathrm{f}}]$ contains $|\mathcal{S}_{n_{\mathrm{f}}}|$ received signals overlapped in the code space (*vide* (2.9)), where $|\mathcal{S}_{n_{\mathrm{f}}}|$ is the cardinality of $\mathcal{S}_{n_{\mathrm{f}}}$. We assume that the correlation process is able to separate the n_{c}th signal from the others in the n_{f}th narrowband, where $n_{\mathrm{c}} \in \mathcal{S}_{n_{\mathrm{f}}}$. Therefore, by using (2.9), we can rewrite (2.21) as

$$\begin{aligned} y[k,n_{\mathrm{c}}] =& \frac{A[k,n_{\mathrm{c}}]}{N} \sum_{n=kN}^{(k+1)N-1} s\left(nT_{\mathrm{s}} - \tilde{\tau}_{\mathrm{T}}[k,n_{\mathrm{c}}]\right) c\left(nT_{\mathrm{s}} - \hat{\tau}_{\mathrm{T}}[k,n_{\mathrm{c}}]\right) e^{j\delta\phi_{\mathrm{T}}[n,n_{\mathrm{c}}]} \\ &+ \frac{1}{N} \sum_{n=kN}^{(k+1)N-1} \eta[n,n_{\mathrm{f}}]\, c\left(nT_{\mathrm{s}} - \hat{\tau}_{\mathrm{T}}[k,n_{\mathrm{c}}]\right) e^{-j\hat{\phi}_{\mathrm{T}}[n,n_{\mathrm{c}}]}, \end{aligned} \tag{2.22}$$

where $\delta\phi_{\mathrm{T}}[n,n_{\mathrm{c}}] \triangleq \tilde{\phi}_{\mathrm{T}}[n,n_{\mathrm{c}}] - \hat{\phi}_{\mathrm{T}}[n,n_{\mathrm{c}}] \in \mathbb{R}$ is the phase error that drives the tracking loop (under perfect lock, $\delta\phi_{\mathrm{T}}[n,n_{\mathrm{c}}]$ is zero). Substituting Equations (2.17) and (2.20) into the definition of $\delta\phi_{\mathrm{T}}[n,n_{\mathrm{c}}]$ yields

$$\begin{aligned} \delta\phi_{\mathrm{T}}[n,n_{\mathrm{c}}] =& 2\pi\left(\tilde{f}_{\mathrm{D}}[k,n_{\mathrm{c}}] - \hat{f}_{\mathrm{D}}[k,n_{\mathrm{c}}]\right)(nT_{\mathrm{s}} - kT) + \left(\tilde{\phi}[k,n_{\mathrm{c}}] - \hat{\phi}[k,n_{\mathrm{c}}]\right) \\ =& 2\pi\delta f_{\mathrm{D}}[k,n_{\mathrm{c}}]\,(nT_{\mathrm{s}} - kT) + \delta\phi[k,n_{\mathrm{c}}], \end{aligned} \tag{2.23}$$

where $\delta f_{\mathrm{D}}[k,n_{\mathrm{c}}] \triangleq \tilde{f}_{\mathrm{D}}[k,n_{\mathrm{c}}] - \hat{f}_{\mathrm{D}}[k,n_{\mathrm{c}}]$ is the residual Doppler frequency error and $\delta\phi[k,n_{\mathrm{c}}] \triangleq \tilde{\phi}[k,n_{\mathrm{c}}] - \hat{\phi}[k,n_{\mathrm{c}}]$. Substituting (2.23) into (2.22) gives

$$\begin{aligned} y[k,n_{\mathrm{c}}] =& \frac{A[k,n_{\mathrm{c}}]}{N} e^{j\delta\phi[k,n_{\mathrm{c}}]} \sum_{n=kN}^{(k+1)N-1} s\left(nT_{\mathrm{s}} - \tilde{\tau}_{\mathrm{T}}[k,n_{\mathrm{c}}]\right) c\left(nT_{\mathrm{s}} - \hat{\tau}_{\mathrm{T}}[k,n_{\mathrm{c}}]\right) e^{j2\pi\delta f_{\mathrm{D}}[k,n_{\mathrm{c}}](n-kN)T_{\mathrm{s}}} \\ &+ \frac{1}{N} \sum_{n=kN}^{(k+1)N-1} \eta[n,n_{\mathrm{f}}]\, c\left(nT_{\mathrm{s}} - \hat{\tau}_{\mathrm{T}}[k,n_{\mathrm{c}}]\right) e^{-j\hat{\phi}_{\mathrm{T}}[n,n_{\mathrm{c}}]} \\ =& \frac{A[k,n_{\mathrm{c}}]}{N} e^{j\delta\phi[k,n_{\mathrm{c}}]} \sum_{i=0}^{N-1} s\left(iT_{\mathrm{s}} - \tilde{\tau}_{\mathrm{T}}[k,n_{\mathrm{c}}] + kT\right) c\left(iT_{\mathrm{s}} - \hat{\tau}_{\mathrm{T}}[k,n_{\mathrm{c}}]\right) e^{j2\pi\delta f_{\mathrm{D}}[k,n_{\mathrm{c}}]iT_{\mathrm{s}}} \\ &+ \frac{1}{N} \sum_{i=0}^{N-1} \eta[i,n_{\mathrm{f}}]\, c\left(iT_{\mathrm{s}} - \hat{\tau}_{\mathrm{T}}[k,n_{\mathrm{c}}]\right) e^{-j\hat{\phi}_{\mathrm{T}}[i+kN,n_{\mathrm{c}}]} \\ =& \frac{A[k,n_{\mathrm{c}}]}{N} e^{j\delta\phi[k,n_{\mathrm{c}}]} \sum_{i=0}^{N-1} s\left(iT_{\mathrm{s}} - \tilde{\tau}_{\mathrm{T}}[k,n_{\mathrm{c}}] + kT\right) c\left(iT_{\mathrm{s}} - \hat{\tau}_{\mathrm{T}}[k,n_{\mathrm{c}}]\right) e^{j2\pi\delta f_{\mathrm{D}}[k,n_{\mathrm{c}}]iT_{\mathrm{s}}} \\ &+ v[k,n_{\mathrm{c}}], \end{aligned} \tag{2.24}$$

where the summation index has changed from n to $i = n - kN$. The time shift in $\eta[i,n_{\mathrm{f}}]$ is neglected as it is wide-sense stationary (WSS). The noise term $v[k,n_{\mathrm{c}}]$ is defined as

$$v[k,n_{\mathrm{c}}] \triangleq \frac{1}{N} \sum_{i=0}^{N-1} \eta[i,n_{\mathrm{f}}]\, c\left(iT_{\mathrm{s}} - \hat{\tau}_{\mathrm{T}}[k,n_{\mathrm{c}}]\right) e^{-j\hat{\phi}_{\mathrm{T}}[i+kN,n_{\mathrm{c}}]}. \tag{2.25}$$

The noise $v[k,n_c] \in \mathbb{C}$ is a zero-mean and proper[13] Gaussian noise with variance

$$\begin{aligned}\sigma_v^2 = \frac{1}{N^2}\mathrm{E}\left[v[k,n_c]\,v^*[k,n_c]\right] = \frac{1}{N^2}\mathrm{E}\Bigg[&\sum_{p=0}^{N-1}\eta[p,n_f]\,c\left(pT_s-\hat{\tau}_T[k,n_c]\right)e^{j\hat{\phi}_T[p+Nk,n_c]} \\ &\sum_{q=0}^{N-1}\eta^*[q,n_f]\,c\left(qT_s-\hat{\tau}_T[k,n_c]\right)e^{-j\hat{\phi}_T[q+Nk,n_c]}\Bigg] \\ = \frac{1}{N^2}\sum_{p=0}^{N-1}\sum_{q=0}^{N-1}&R_\eta[p-q,n_f]\,c\left(pT_s-\hat{\tau}_T[k,n_c]\right)c\left(qT_s-\hat{\tau}_T[k,n_c]\right)e^{-j\left(\hat{\phi}_T[p+Nk,n_c]-\hat{\phi}_T[q+Nk,n_c]\right)}\end{aligned} \tag{2.26}$$

where $\cdot^*$ denotes the conjugate operator,

$$R_\eta[m,n_f] = \mathrm{E}\left[\eta[n+m,n_f]\,\eta^*[n,n_f]\right] = 2N_0B_{\max}\delta[m] \tag{2.27}$$

is the autocorrelation function of $\eta[n,n_f]$ (*cf.* (B.28)) and

$$\delta[m] = \begin{cases} 1 & m=0 \\ 0 & \text{otherwise} \end{cases} \tag{2.28}$$

is the Kronecker function. Substituting (2.27) into (2.26) yields

$$\sigma_v^2 = \frac{2N_0B_{\max}}{N} = \frac{\sigma_\eta^2}{N}, \tag{2.29}$$

where $\sigma_\eta^2 = 2N_0B_{\max}$ is the variance of $\eta[n,n_f]$ (*cf.* (B.2)).

2.5 Monitoring Station Subroutines for Scintillation Signal Extraction

On the one hand, part of the monitoring station subroutines are similar to the ones implemented in conventional GNSS receivers. On the other hand, specific monitoring-geared algorithms should be implemented to separate the scintillation-induced amplitude and phase variations from other impairments affecting the received signal. This distinction arises because *the monitoring problem is not a navigation problem*. Hence, they must not be treated likely (CURRAN *et al.*, 2014). While conventional receivers strive to compute the PVT solution and demodulate the navigation message while maintaining lock, scintillation monitoring stations can know their fixed position beforehand and can survey the navigation message transmitted during a scintillation event at the cost of offline processing.

With the navigation message, the following monitoring-geared subroutines can be implemented:

[13] A complex-valued and WSS process $a(t)$ is called proper when its pseudocovariance is zero, *i.e.*, $\mathrm{E}\left[\left(a(t)-\mathrm{E}[a(t)]\right)^2\right] = 0$ (PROAKIS; SALEHI, 2007, p. 65).

- *Bit wipe-off*: during ionospheric scintillation, errors in the navigation bit detection lead to phase errors. The bit wipe-off technique consist of recording the high-rate baseband signal during scintillation event and reprocessing it offline with the correct navigation bits. This procedure eliminates bit-induced half-cycle phase discontinuities (HUMPHREYS *et al.*, 2010a; HUMPHREYS *et al.*, 2010b).
- *LOS effects removal*: under nominal conditions, the station location is determined using a navigation algorithm just as in a standard GNSS receiver, *i.e.*, by solving the ranging equations from the measured pseudoranges to obtain the positioning and timing. Once the solution converges, the station position is trusted for long periods since only the Earth-crustal motion can cause a variation. Thus, the fixed station position and the satellite trajectory (calculated from broadcast ephemerides) provide a coarse estimation of the true geometric range. Under a scintillation event, this information can be combined with the postcorrelated data to separate LOS effects from other impairments. However, since the satellite trajectory information is not available worldwide instantaneously, the receiver must record the BB signal during a scintillation event and reprocess it offline with the estimated satellite trajectory. Obtaining the satellite-receiver dynamics information for monitoring is a key advantage over the traditional navigation problem, where the receiver position is unknown (in a cold start) and must be determined in real time. The rationale is that, even for advanced tracking algorithms, separating LOS components from scintillation effects is often difficult for receivers used for navigation, where propagation geometry is unknown (FLORINDO *et al.*, 2025).
- *Satellite clock error correction*: the transmission time with respect to the satellite clock readings and the coefficients of the polynomial equation are broadcasted to the receiver. These coefficients are used to correct the bias between the system time and the satellite clock, which operates in free-running mode (CURRAN *et al.*, 2014).

Additional conditions and subroutines can mitigate other effects that may obscure scintillation observations:

- *Receiver clock error mitigation*: the LO used by the monitoring station should be a rubidium (*i.e.,* atomic) or an oven-controlled crystal oscillator (OCXO) to provide a stable reference. As discussed in Section 2.2, the estimated receiver clock bias, obtained from the navigation solution under nominal conditions, can be used to discipline the local clock readings to the GNSS system time. However, during a scintillation event, only the last

computed bias shall be used since the timing solution cannot be trusted anymore. If the duration of the scintillation event is long enough, the receiver clock bias can drift significantly, and the static correction may not be sufficient. In such cases, an *a priori* clock model can be adopted to compensate the long-term drift and remove it from receiver clock. This approach does not completely remove the receiver clock error, but mitigates its impact (CURRAN *et al.*, 2014).

- *AGC bypass*: the AGC should be disabled to avoid masking scintillation amplitude variations (DIERENDONCK; ARBESSER-RASTBURG, 2004).

Let $\hat{\rho}_{\mathrm{s,g}}[k,n_{\mathrm{c}}]$ be the estimate of $\rho_{\mathrm{s,g}}[k,n_{\mathrm{c}}] \triangleq \rho_{\mathrm{s,g}}(kT,n_{\mathrm{c}})$, obtained in the monitoring station from the ephemerides. Therefore, $\hat{\tau}_{\mathrm{s,g}}[k,n_{\mathrm{c}}] = \hat{\rho}_{\mathrm{s,g}}[k,n_{\mathrm{c}}]/c_0$ provides a coarse estimate of the LOS code delay, $\tau_{\mathrm{LOS}}[k,n_{\mathrm{c}}] = \rho_{\mathrm{s,g}}[k,n_{\mathrm{c}}]/c_0$. Likewise,

$$\hat{f}_{\mathrm{s,g}}[k,n_{\mathrm{c}}] = -f_{\mathrm{c}} \left.\frac{\mathrm{d}\hat{\tau}_{\mathrm{s,g}}(t,n_{\mathrm{c}})}{\mathrm{d}t}\right|_{t=kT} \tag{2.30}$$

provides a coarse estimation of $f_{\mathrm{D}}[k,n_{\mathrm{c}}]$, where $\hat{\tau}_{\mathrm{s,g}}[k,n_{\mathrm{c}}] \triangleq \hat{\tau}_{\mathrm{s,g}}(kT,n_{\mathrm{c}})$ and the derivative can be numerically computed (PACELLI *et al.*, 2025a, Equation (10)).

In this thesis, we assume that a Bayesian estimation framework (*e.g.*, KF) uses $\hat{f}_{\mathrm{s,g}}[k,n_{\mathrm{c}}]$, $\hat{\tau}_{\mathrm{s,g}}[k,n_{\mathrm{c}}]$, and $y[k,n_{\mathrm{c}}]$ as input. At each correlation interval, the framework outputs $\hat{f}_{\mathrm{D}}[k,n_{\mathrm{c}}]$, $\hat{\tau}_{\mathrm{T}}[k,n_{\mathrm{c}}]$, and $\hat{\phi}[k,n_{\mathrm{c}}]$, which are fed back into the tracking system. While $\hat{f}_{\mathrm{D}}[k,n_{\mathrm{c}}]$ and $\hat{\phi}[k,n_{\mathrm{c}}]$ are used to generate the carrier replica in (2.20), $\hat{\tau}_{\mathrm{T}}[k,n_{\mathrm{c}}]$ is used to align the code phase. Under sufficiently accurate conditions, $\hat{\phi}[n,n_{\mathrm{c}}] \approx \tilde{\phi} \approx \phi[k,n_{\mathrm{c}}]$, $\hat{f}_{\mathrm{D}}[k,n_{\mathrm{c}}] \approx \tilde{f}_{\mathrm{D}}[k,n_{\mathrm{c}}] \approx f_{\mathrm{D}}[k,n_{\mathrm{c}}]$, and $\hat{\tau}_{\mathrm{T}}[k,n_{\mathrm{c}}] \approx \tilde{\tau}_{\mathrm{T}}[k,n_{\mathrm{c}}] \approx \tau_{\mathrm{T}}[k,n_{\mathrm{c}}]$. The tilde notation is also dropped because it is assumed that satellite clock errors are removed using the navigation message and that receiver clock errors are negligible due to a high-stability external reference clock. Therefore, clock error contributions in (2.16), (2.15), and (2.18) are neglected.

These assumptions allow reasonable code phase and Doppler wipe-off in (2.22), yielding[14]

$$\begin{aligned} y[k,n_{\mathrm{c}}] =& \frac{A[k,n_{\mathrm{c}}]}{N} e^{j\delta\phi[k,n_{\mathrm{c}}]} \sum_{n=0}^{N-1} e^{j2\pi\delta f_{\mathrm{D}}[k,n_{\mathrm{c}}]nT_{\mathrm{s}}} + v[n,n_{\mathrm{c}}] \\ =& \frac{A[k,n_{\mathrm{c}}]}{N} e^{j\delta\phi[k,n_{\mathrm{c}}]} \frac{\sin(\pi\delta f_{\mathrm{D}}[k,n_{\mathrm{c}}]NT_{\mathrm{s}})}{\sin(\pi\delta f_{\mathrm{D}}[k,n_{\mathrm{c}}]T_{\mathrm{s}})} e^{j\pi\delta f_{\mathrm{D}}[k,n_{\mathrm{c}}](N-1)T_{\mathrm{s}}} + v[n,n_{\mathrm{c}}], \end{aligned} \tag{2.31}$$

where $s(nT_{\mathrm{s}} - \hat{\tau}_{\mathrm{T}}[k,n_{\mathrm{c}}]) = c(nT_{\mathrm{s}} - \hat{\tau}_{\mathrm{T}}[k,n_{\mathrm{c}}])$ is assumed under the bit wipe-off procedure, $\tilde{\phi}[k,n_{\mathrm{c}}] \approx \phi[k,n_{\mathrm{c}}]$ is assumed under negligible clock errors , $c^2(nT_{\mathrm{s}} - \hat{\tau}_{\mathrm{T}}[k,n_{\mathrm{c}}]) \triangleq 1$

[14] $\sum_{k=a}^{b} e^{jkx} = \frac{\sin\left(\frac{b+1-a}{2}x\right)}{\sin\left(\frac{x}{2}\right)} e^{j\frac{(a+b)x}{2}}$.

By considering the following approximations

$$N \gg 1 \therefore N \approx N-1, \tag{2.32}$$

$$\pi\delta f_{\mathrm{D}}[k,n_{\mathrm{c}}]T_{\mathrm{s}} \to 0 \therefore \sin(\pi\delta f_{\mathrm{D}}[k,n_{\mathrm{c}}]T_{\mathrm{s}}) \approx \pi\delta f_{\mathrm{D}}[k,n_{\mathrm{c}}]T_{\mathrm{s}}, \tag{2.33}$$

in (2.31), we have that

$$\boxed{y[k,n_{\mathrm{c}}] = A[k,n_{\mathrm{c}}]\,\mathrm{sinc}(\delta f_{\mathrm{D}}[k,n_{\mathrm{c}}]T)\,e^{j(\pi\delta f_{\mathrm{D}}[k,n_{\mathrm{c}}]T+\delta\phi[k,n_{\mathrm{c}}])} + v[k,n_{\mathrm{c}}],} \tag{2.34}$$

where

$$\mathrm{sinc}(x) = \frac{\sin(\pi x)}{\pi x}. \tag{2.35}$$

For $\delta f_{\mathrm{D}}[k,n_{\mathrm{c}}] \approx 0$, the expression in (2.31) can be further simplified to

$$\boxed{y[k,n_{\mathrm{c}}] = A[k,n_{\mathrm{c}}]\,e^{j\delta\phi[k,n_{\mathrm{c}}]} + v[k,n_{\mathrm{c}}].} \tag{2.36}$$

Under the assumption of AGC bypass, the amplitude of the received signal reads[15]

$$A[k,n_{\mathrm{c}}] \propto \gamma_{\mathrm{T}}[k,n_{\mathrm{c}}] = \sqrt{P_{\mathrm{LOS}}[k,n_{\mathrm{c}}]}\gamma_{\mathrm{s}}[k,n_{\mathrm{c}}], \tag{2.37}$$

where $P_{\mathrm{LOS}}[k,n_{\mathrm{c}}], \gamma_{\mathrm{s}}[k,n_{\mathrm{c}}] \in \mathbb{R}$ are respectively the free-space path loss [W] and the scintillation amplitude distortions caused by diffraction patterns observed by the receiver. The power $P_{\mathrm{LOS}}[k,n_{\mathrm{c}}]$ depends only on the propagation geometry between the satellite and ground stations, and can be deterministically estimated as (HOFMANN-WELLENHOF *et al.*, 2008, Equation (4.24))

$$\hat{P}_{\mathrm{LOS}}[k,n_{\mathrm{c}}] = G_{\mathrm{s}}G_{\mathrm{g}}P\hat{L}[k,n_{\mathrm{c}}], \tag{2.38}$$

where $G_{\mathrm{s}}, G_{\mathrm{g}} \in \mathbb{R}_+$ are the satellite and receiver antenna gains (constants), respectively, and $\hat{L}[k,n_{\mathrm{c}}] \in \mathbb{R}_+$ is the closed-form estimate of free-space path loss, given by the Friis transmission formula (HOFMANN-WELLENHOF *et al.*, 2008, Equation (4.22)):

$$\hat{L}[k,n_{\mathrm{c}}] = \left(\frac{c_0}{4\pi f_{\mathrm{c}}\hat{\rho}_{\mathrm{s,g}}[k,n_{\mathrm{c}}]}\right)^2. \tag{2.39}$$

Normalizing $y[k,n_{\mathrm{c}}]$ by $\sqrt{\hat{P}_{\mathrm{LOS}}[k,n_{\mathrm{c}}]}$ leads to

$$\boxed{\bar{y}[k,n_{\mathrm{c}}] = \gamma_{\mathrm{s}}[k,n_{\mathrm{c}}]\,e^{j\delta\phi[k,n_{\mathrm{c}}]} + \bar{v}[k,n_{\mathrm{c}}]}, \tag{2.40}$$

[15] Under AGC bypass condition, some proportionality constant is expected due to gains in the analog RF and IF stages.

where $\bar{y}[k,n_c] \triangleq y[k,n_c]/\sqrt{\hat{P}_{LOS}[k,n_c]}$ and $\bar{v}[k,n_c] \triangleq v[k,n_c]/\sqrt{\hat{P}_{LOS}[k,n_c]}$. Note that a proportionality constant due to analog gains in the RF and IF stages is expected to scale $\gamma_s[k,n_c]$ in (2.40). In practice, it should appear as a constant bias in the C/N_0 estimate under nonscintillation conditions. Here, this constant is set to one for the sake of simplicity. In practice, the noise variance is obtained from the carrier-to-noise ratio estimates in Hz, $\widehat{c/N_0}[k]$ (LOPES *et al.*, 2023b), leading to

$$\sigma_{\bar{v}}^2[k] = \frac{1}{T\,\widehat{c/N_0}[k]}. \tag{2.41}$$

With accurate code phase and Doppler wipe-off, the assumed Bayesian estimation framework locks onto $\phi[k,n_c]$ in (2.40) and outputs $\hat{\phi}[k,n_c]$. However, from a cold start, the estimate $\hat{\phi}[k,n_c]$ provides only the measurable fractional (wrapped) part of the total (unwrapped) carrier phase, $\phi[k,n_c]$.

2.6 Postprocessing for Scintillation Phase Extraction

On the one hand, traditional GNSS receivers use a set of four ranging equations to calculate the receiver position and recover the timing, which are unknown variables. To obtain precise and accurate positioning, all sort of impairments affecting $\tau_T[n,n_c]$ (and also $\phi_T[n,n_c]$ for carrier-based ranging) should be properly modeled and eliminated. On the other hand, the primary goal of the monitoring station is not to determine its position, but to extract the scintillation-induced variations from the received signal.

By converting the measured phase into pseudoranges, one can obtain the observable pseudorange, given by (HOFMANN-WELLENHOF *et al.*, 2012, Equation (6.9))

$$-\frac{c_0}{2\pi f_c}\hat{\phi}[k,n_c] = \rho_{s,g}[k,n_c] - \frac{c_0}{2\pi f_c}\phi_{atm}[k,n_c] + \frac{c_0}{f_c}M[k,n_c], \tag{2.42}$$

where $M[k,n_c] \in \mathbb{Z}$ is an integer ambiguity term due to the unknown number of full carrier phase cycles. Although omitted here for the sake of readability, an additive term in (2.42) should be inserted to account for other unmodeled impairments (multipath effects, hardware biases, Sagnac effect, secondary relativistic error, wind-up effects, *etc.*). However, their impact is considered small compared to the modeled effects during a scintillation event.

The atmospheric term is decomposed into the neutral nondispersive tropospheric phase contribution, the dispersive ionospheric phase contribution caused by the stable total electron content (TEC), and scintillation-induced phase variations due to turbulent plasma

irregularities, yielding

$$-\frac{c_0}{2\pi f_c}\hat{\phi}\left[k,n_c\right]=\rho_{s,g}\left[k,n_c\right]-40.3\frac{\mathrm{TEC}\left[k,n_c\right]}{{f_c}^2}-\frac{c_0}{2\pi f_c}\phi_s\left[k,n_c\right]+\rho_{trop}\left[k,n_c\right]+\frac{c_0}{f_c}M\left[k,n_c\right], \tag{2.43}$$

where $\mathrm{TEC}\left[k,n_c\right]\in\mathbb{R}_+$ is the electron content in TEC units [10^{16} $\mathrm{e}^-/\mathrm{m}^2$] along the signal path, $\phi_s\left[k,n_c\right]\in\mathbb{R}$ models the scintillation-induced phase variations [rad], and $\rho_{trop}\left[k,n_c\right]\in\mathbb{R}_+$ is the tropospheric range delay [m]. Note that

1. With the satellite range obtained from the ephemerides, we replace $\rho_{s,g}\left[k,n_c\right]$ with its estimate, $\hat{\rho}_{s,g}\left[k,n_c\right]$. Due to the very short carrier wavelength ($\approx 19\,\mathrm{cm}$ for L1 signals), some ambiguities in $M\left[k,n_c\right]$ might remain due to unmodeled effects or imprecisions in $\hat{\rho}_{s,g}\left[k,n_c\right]$. However, considering that the unique goal is the scintillation signal monitoring and provided that cycle slips do not occur, this ambiguity is translated into an initial and constant phase bias in the unwrapped scintillation phase, observed over the scintillation event, which does not affect its statistical analysis.
2. Since MF signals are expected, the ionosphere-free combination can be applied to (2.43) in order to eliminate the first-order and dominant term of the stable part of ionosphere, given by $40.3\mathrm{TEC}\left[k,n_c\right]/{f_c}^2$ (RINO *et al.*, 2018).
3. The tropospheric range delay [m], denoted as $\rho_{trop}\left[k,n_c\right]$, can be estimated by models such as Hopfield (HOFMANN-WELLENHOF *et al.*, 2008, Section 5.3.3).

Under these assumptions, the only remaining unknown in postprocessing is the scintillation phase. For simplicity, under the argument that the remaining phase contributions are removed during postprocessing, this thesis considers

$$\boxed{\hat{\psi}_s\left[k,n_c\right]=\psi_s\left[k,n_c\right]+\bar{v}\left[k,n_c\right],} \tag{2.44}$$

as the signal model for the scintillation event coming from the monitoring station, where $\psi_s\left[k,n_c\right]=\gamma_s\left[k,n_c\right]e^{j\phi_s\left[k,n_c\right]}\in\mathbb{C}$ is the scintillation signal and, in the context of phase screen theory, is also referred to as the complex field.

3 SCINTILLATION MODEL AND SIGNAL SIMULATION

This chapter introduces two scintillation models used to generate synthetic data for the simulations:

- The compact phase-screen-based scintillation model (CPSSM).
- The Cornell scintillation model (CSM).

3.1 The Compact Phase-Screen-based Scintillation Model

The CPSSM is a physics-based scintillation model grounded in phase screen theory, pioneered by Booker *et al.* (1950) and subsequently extended by many researchers. This section summarizes only the key concepts and assumptions used to implement the CPSSM.

3.1.1 Theory background

Diffraction theory approximates electromagnetic wave propagation through the ionosphere as a thin sheet that modulates amplitude and phase (RATCLIFFE, 1956). At a given receiver, interference among plane waves produces a position-dependent intensity pattern governed by the scattering direction (directional cosines). Amplitude modulation can often be neglected, and the spectrum of the random phase is sufficient, motivating the phase screen model (HEWISH, 1951).

A key improvement to the phase screen model replaced Gaussian spectra with more realistic power-law forms (RUFENACH, 1972). Under weak scattering, one-component power law is sufficient to model the phase PSD, which in temporal frequency is given by (HUMPHREYS *et al.*, 2010b)

$$S_{\phi_\mathrm{s}}(f) = \frac{C_\mathrm{p}}{({f_0}^2 + f^2)^{\frac{p}{2}}} \in \mathbb{R} \quad [\mathrm{rad}^2/\mathrm{Hz}], \tag{3.1}$$

where $p \in \mathbb{R}$ is the spectral index (or slope). The term $f_0 = v_\mathrm{e}/L_0 \in \mathbb{R}$ is the temporal frequency [Hz] associated with the irregularity outer scale [m], denoted as $L_0 \in \mathbb{R}_+$, and $v_\mathrm{e} \in \mathbb{R}$ is the effective scan velocity [m/s] at the irregularity height. The strength parameter $C_\mathrm{p} \in \mathbb{R}$ approximately equals $S_{\phi_\mathrm{s}}(f)\big|_{f=1\,\mathrm{Hz}}$ since $f_0 \ll 1\,\mathrm{Hz}$ (KNIGHT, 2000, p. 11). Since f_0 is often poorly defined, the approximation $S_{\phi_\mathrm{s}}(f) \approx C_\mathrm{p} f^{-p}$ is commonly used (HUMPHREYS *et al.*, 2010b; FOHLMEISTER, 2021). The value of p depends on turbulence development, including the underlying instability process, latitude, and altitude (BÉNIGUEL, 2011). It typically lies

between 1 and 4, with 2.5 common in equatorial regions (KNIGHT, 2000).

The phase PSD defines the random phase fluctuations imposed at a fixed height, typically between 300 km and 400 km, where F-region irregularities are strongest (MACDOUGALL, 1981). The resulting phase screen is propagated to the receiver by solving the parabolic wave equation (PWE) with a split-step algorithm (RINO *et al.*, 2018).

3.1.2 Solving the parabolic wave equation via split-step algorithm

An electromagnetic wave propagating through a random ionospheric medium is governed by the PWE, which describes the spatial variation of the complex field. In equatorial regions, inhomogeneous structures within the ionosphere are elongated along magnetic field lines, so north–south variation can be neglected (KINTNER *et al.*, 2004). Under this assumption, a scalar eastward form of the PWE is sufficient to describe propagation at a fixed height. The resulting PWE for a time-harmonic complex field propagating from the GNSS satellite to the ground antenna is given by (RINO *et al.*, 2018, Equation (6))

$$\frac{\partial \psi_{\mathrm{s}}(x,y)}{\partial x} = \Theta_{\rho_{\mathrm{F}}} \psi_{\mathrm{s}}(x,y) + jk_{\mathrm{c}} \Delta n(x,y)\, \psi_{\mathrm{s}}(x,y), \tag{3.2}$$

where x and y denote respectively the downward (propagation-directed, starting from the phase screen) and geomagnetic eastward direction (see Figure 2 from Jiao *et al.* (2018)), $k_{\mathrm{c}} = 2\pi f_{\mathrm{c}}/c_0 = 2\pi/\lambda_{\mathrm{c}} \in \mathbb{R}$ is the carrier wavenumber [rad/m], and $\lambda_{\mathrm{c}} \in \mathbb{R}$ is the carrier wavelength [m]. The first term, $\Theta_{\rho_{\mathrm{F}}} \psi_{\mathrm{s}}(x,y)$, models the free-space propagation and is defined as (RINO *et al.*, 2018, Equation (7), (8))

$$\Theta_{\rho_{\mathrm{F}}} \psi_{\mathrm{s}}(x,y) = \frac{1}{2\pi} \int \Psi_{\mathrm{s}}(x,k_y) \exp\left\{-j\left(k_y \rho_{\mathrm{F}}\right)^2/2\right\} \exp\left\{jyk_y\right\} \mathrm{d}k_y, \tag{3.3}$$

where k_y is the wavenumber [rad/m] in the eastward direction, and

$$\Psi_{\mathrm{s}}(x,k_y) = \int \psi_{\mathrm{s}}(x,y) \exp(-jyk_y)\, \mathrm{d}y \tag{3.4}$$

is the Fourier transform of the complex field in the eastward direction. Finally, the second term in (3.2), $jk_{\mathrm{c}} \Delta n(x,y)\, \psi_{\mathrm{s}}(x,y)$, describes the phase modulation due to refraction, caused by the random fluctuations in the local refractive index, $\Delta n(x,y)$.

The phase screen model became practical with advances in numerical methods, particularly the fast Fourier transform (FFT) and split-step solutions of the PWE. The core idea of the split-step algorithm is to divide the interaction between the wavefront and the medium

into two steps: (i) solve via FFT the phase distortions caused by refraction, *i.e.*, the random fluctuations in the refractive index; (ii) propagate the wavefront thus refracted in free space. Note that, although the phase screen neglects the theoretical PSD of the amplitude scintillation, the propagation of the phase-modulated wavefront emanating from the phase screen through free space naturally introduces amplitude fluctuations, which describes, as a consequence of the phase screen model, the diffractive pattern observed at the receiver.

The split-step algorithm can be summarized as the forward and inverse FFT operations as follows:

$$\Psi_{\mathrm{s}}\left(0, n\Delta k_y\right) \triangleq \Psi_{\mathrm{s}}\left[0,n\right] = \sum_{m=0}^{N-1} e^{j\phi_{\mathrm{r}}[m]} W_N^{nm}, \quad n = 0,1,\ldots,N-1, \tag{3.5}$$

and

$$\begin{aligned}\psi_{\mathrm{s}}\left(x, m\Delta y\right) &\triangleq \psi_{\mathrm{s}}\left[x,m\right] \\ &= \frac{1}{N}\sum_{n=0}^{N-1} \Psi_{\mathrm{s}}\left[0,n\Delta k_y\right] \exp\left\{-jk_{\mathrm{c}}\left(n\Delta k_y/k_{\mathrm{c}}\right)^2 x/2\right\} W_N^{-nm}, \quad m = 0,1,\ldots,N-1,\end{aligned} \tag{3.6}$$

where $W_N \triangleq e^{-j\frac{2\pi}{N}}$ is the twiddle factor, $N \in \mathbb{N}$ is the number of samples, $\Delta y \in \mathbb{R}$ is the distance resolution along the eastward direction [m], and $\Delta k_y \in \mathbb{R}$ is the wavenumber resolution [rad/m] in y. Here, n and m represent the FFT coefficient pair for the spatial frequency and spatial domain, respectively.

Let us define the Fresnel scale as (JIAO *et al.*, 2017, Equation (3))

$$\rho_{\mathrm{F}} = \sqrt{x/k_{\mathrm{c}}} \in \mathbb{R} \quad [\mathrm{m}]. \tag{3.7}$$

Since $x = \rho_{\mathrm{F}}^2 k_{\mathrm{c}}$, (3.6) can be further simplified to

$$\psi_{\mathrm{s}}\left[x,m\right] = \frac{1}{N}\sum_{n=0}^{N-1} \Psi_{\mathrm{s}}\left[0,n\Delta k_y\right] \exp\left\{-j\left(n\Delta k_y \rho_{\mathrm{F}}\right)^2/2\right\} W_N^{-nm}. \tag{3.8}$$

Finally, the FFT for the split-step algorithm can be expressed as

$$\Psi_{\mathrm{s}}\left[0,n\right] = \sum_{m=0}^{N-1} e^{j\phi_{\mathrm{r}}[m]} W_N^{nm} \tag{3.9}$$

$$\psi_{\mathrm{s}}\left[x,m\right] = \frac{1}{N}\sum_{n=0}^{N-1} \Psi_{\mathrm{s}}\left[0,n\Delta k_y\right] \exp\left\{-j\left(n\Delta\mu_y\right)^2/2\right\} W_N^{-nm} \tag{3.10}$$

where $\Delta\mu_y = \Delta k_y \rho_{\mathrm{F}}$ is the normalized wavenumber resolution in y direction. Equations (3.9) and (3.10) form the basis of the split-step algorithm, which starts generating the random phase-integrated phase, $\phi_{\mathrm{r}}\left[m\right] \in \mathbb{R}$, representing the refracted phase emanating from the thin screen and whose PSD follows the one- or two-component power-law spectrum.

3.1.3 The two-component power-law PSD

Equation (3.1) is widely used to model the phase scintillation spectrum through p and C_p, but it is accurate only under weak scattering (RINO, 1979). For strong scintillation ($0.6 < S_4 < 1$), two-component power-law spectra are commonly used (SHISHOV, 1974; RINO; CARRANO, 2013), which is a generalization of the one component. Asymptotic and numerical analyses suggest that this model is consistent with measured data under strong scattering (RINO; CARRANO, 2013; RINO *et al.*, 2014).

As proposed by Rino *et al.* (2018), the one-dimensional two-component power-law phase spectrum can be expressed in the spatial frequency as

$$S_{\phi_\mathrm{s}}(k_y) = C_\mathrm{p} \begin{cases} k_y^{-p_1}, & k_y \leq k_{y0} \\ k_{y0}^{p_2-p_1} k_y^{-p_2}, & k_y > k_{y0} \end{cases}, \tag{3.11}$$

where $p_1, p_2 \in \mathbb{R}$ are the spectral indices[1] for the low- and high-frequency regimes, respectively, and $k_{y0} = 2\pi/L_0 \in \mathbb{R}$ is the break wavenumber [rad/m] at the Fresnel scale, *i.e.*, the spatial frequency corresponding to the spectral break point (where the spectral index switch from p_1 to p_2). If (3.11) is normalized by the Fresnel scale, it can be rewritten as

$$P_{\phi_\mathrm{s}}(\mu_y) = \frac{S_{\phi_\mathrm{s}}(k_y)}{\rho_\mathrm{F}} = \begin{cases} U_1 \mu_y^{-p_1}, & \mu_y \leq \mu_{0y} \\ U_2 \mu_y^{-p_2}, & \mu_y > \mu_{0y} \end{cases}, \tag{3.12}$$

where $\mu_{0y} = k_{y0}\rho_\mathrm{F} \in \mathbb{R}$ is the normalized break wavenumber, $U_1 = C_\mathrm{p}\rho_\mathrm{F}^{p_1-1}$, and $U_2 = C_\mathrm{p}\rho_\mathrm{F}^{p_1-1}\mu_{0y}^{p_2-p_1} = U_1\mu_{0y}^{p_2-p_1}$. The so-called universal PSD strength reads (JIAO *et al.*, 2017, Equation (7))

$$U = \begin{cases} U_1, & \mu_{0y} \geq 1 \\ U_2, & \mu_{0y} < 1 \end{cases}. \tag{3.13}$$

When $U \ll 1$, the scatter is weak, and when $U \gg 1$, the scatter is strong (JIAO *et al.*, 2017).

3.1.4 Implementation of the two-component power-law phase screen model

A realization of $\phi_\mathrm{r}[m]$ is obtained by generating an N-point complex white Gaussian noise sequence, $\eta_{\phi_\mathrm{s}}[n]$, with Hermitian symmetry:

$$\eta_{\phi_\mathrm{s}}[n] = \eta_{\phi_\mathrm{s}}^*[\mathrm{mod}(N-n, N)], \tag{3.14}$$

$$\mathrm{E}\left\{\eta_{\phi_\mathrm{s}}[n_1]\,\eta_{\phi_\mathrm{s}}^*[n_2]\right\} = \delta[n_1 - n_2], \tag{3.15}$$

[1] Note that $p_2 \geq p_1$. When $p_1 = p_2 \triangleq p$, it reduces to the one-component power-law spectrum.

respectively, where $\mathrm{mod}\,(\cdot,\cdot)$ denotes the modulus operator. Thus, we have

$$\bar{\phi}_{\mathrm{r}}[m] = \sum_{n=0}^{N-1} \sqrt{P_{\phi_{\mathrm{s}}}(n\Delta\mu_y)\Delta\mu_y/(2\pi)}\,\eta_{\phi_{\mathrm{s}}}[n]\,W_N^{-nm}. \tag{3.16}$$

Substituting $\phi_{\mathrm{r}}[m]$ with $\bar{\phi}_{\mathrm{r}}[m]$ from (3.16) in (3.5) yields $\Psi_{\mathrm{s}}[0,n]$, the complex field after the phase screen. Applying (3.6) then gives the propagated field at the receiver, $\psi_{\mathrm{s}}[x,m]$.

The spatial and temporal grids are related by

$$y[i] = y[i-1] + v_{\mathrm{e}}[i-1]\,(t[i] - t[i-1]), \tag{3.17}$$

where i indexes the spatiotemporal grid in the eastward direction (JIAO *et al.*, 2018, Equation (11)). In our simulation, we set $t[i] - t[i-1] \triangleq T$ to match the sampling interval. The effective velocity v_{e} depends on the ionospheric pierce point (IPP) scan velocity, mean ionospheric drift, irregularity anisotropy, and propagation geometry (see Vasylyev *et al.* (2022, Figure 3)). To reduce computational cost, propagation angles are often treated as constant over 5-minute intervals (JIAO *et al.*, 2018, Section 4.B). When v_{e} varies with time, space–time mapping can yield nonuniform grids, so interpolation is used to recover uniform sampling. Details on computing v_{e} and performing the interpolation are given in Jiao *et al.* (2017, Section 4) and Jiao *et al.* (2018, Section 4.D).

Using this relation, the temporal frequency (Hz) is obtained from the spatial frequency (wavenumber) as (CARRANO *et al.*, 2017, text above Equation (5))

$$k_y = 2\pi\frac{f}{v_{\mathrm{e}}}. \tag{3.18}$$

Since v_{e} governs the wavenumber evolution at the screen, some authors refer to f in (3.18) as a "Doppler frequency" (*vide* Equation (11) in Jiao *et al.* (2017)) because it represents the additional frequency shift on the wavefront, that changes the observed Doppler effect caused strictly by the LOS dynamics (*cf.* Figures 2 and 3 in Rino *et al.* (2015)). Here, to avoid confusion with the Doppler shift caused solely by the satellite–receiver motion, we refer to f as the temporal frequency used for simulation.

By recalling (3.7), the space-time conversion can be expressed in discrete steps and normalized form as

$$\Delta\mu_y = 2\pi\Delta f\frac{\rho_{\mathrm{F}}}{v_{\mathrm{e}}}, \tag{3.19}$$

where $\Delta f = 1/(NT)$ is the temporal frequency resolution [Hz]. In the ionospheric scintillation simulation, the scaling factor, $\rho_{\mathrm{F}}/v_{\mathrm{e}}$, is solely determined by the geometry of the propagation

path and plays an important role in the characteristics observed in the scintillation time series. Larger values of ρ_F/v_e lead to slower variations in the scintillation time series, while smaller values result in faster fluctuations (JIAO *et al.*, 2018, Section 4.D).

Finally, after converting from spatial to time domain, the amplitude $\gamma_s[k,n_c]$ and phase $\phi_s[k,n_c]$ time series can be obtained by taking the absolute value of the resulting complex signal and by applying the algorithm described by Rino *et al.* (2020) for phase recovery, respectively.

3.1.5 Frequency extrapolation technique

To reduce the cost of simulating the phase PSD at multiple frequencies, we employ a frequency extrapolation technique that scales the spectral parameters (μ_{0y}, U, p_1, and p_2) and the geometric factor (ρ_F/v_e). This enables MF scintillation simulation using a single reference carrier frequency.

Let $\mu_{0y,\text{ref}}$, U_{ref} and $\left(\frac{\rho_F}{v_e}\right)_{\text{ref}}$ be the normalized break wavenumber, universal PSD strength, and scaling factor at the reference carrier frequency f_{ref}, respectively, computed using the irregularity parameter estimation (IPE) technique from empirical data (CARRANO; RINO, 2016). The weak scintillation theory can be approximated to strong conditions using the following scaling relations (JIAO *et al.*, 2017, Equations (17) to (19)):

$$\mu_{0y} = \mu_{0y,\text{ref}}\sqrt{\frac{f_{\text{ref}}}{f}}, \tag{3.20}$$

$$\rho_F/v_e = \left(\frac{\rho_F}{v_e}\right)_{\text{ref}}\sqrt{\frac{f_{\text{ref}}}{f}}, \tag{3.21}$$

and

$$U = \begin{cases} U_{\text{ref}}\left(\frac{f}{f_{\text{ref}}}\right)^{\frac{p_1+3}{2}}, & \mu_{0y,\text{ref}} \geq 1, \mu_{0y} \geq 1 \\ U_{\text{ref}}/\mu_{0y,\text{ref}}^{p_2-p_1}\left(\frac{f}{f_{\text{ref}}}\right)^{\frac{p_1+3}{2}}, & \mu_{0y,\text{ref}} < 1, \mu_{0y} \geq 1 \\ U_{\text{ref}}\left(\frac{\mu_{0y}}{\mu_{0y,\text{ref}}}\right)^{p_2-p_1}\left(\frac{f}{f_{\text{ref}}}\right)^{\frac{p_2+3}{2}}, & \mu_{0y,\text{ref}} < 1, \mu_{0y} < 1 \end{cases}. \tag{3.22}$$

These relations are valid for all $f \leq f_{\text{ref}}$.

3.1.6 Adopted irregularity parameters

As demonstrated in Carrano e Rino (2016, Figs. 7a and 7b), for the one-component power law, when the universal turbulence strength is set to $U = 0.1$ and the spectral index p

varies between 1.5 and 4.5, the scintillation intensity index S_4 typically ranges from 0.2 to 0.4. Consequently, for the weak-scattering regime, we adopt $U = 0.05$ and $p_1 = p_2 = p = 3$.

Using the estimation techniques in Carrano *et al.* (2012) and Xu *et al.* (2020), we identified typical irregularity parameters for the strong scattering regime. The mean values for μ_{0y}, p_1, and p_2 are 0.55, 2.45, and 3.7, respectively. According to Carrano e Rino (2016, Section 3.2.3), these values describe a mixed-slope spectrum in which outer- and inner-scale structures jointly distort the transmitted signal. Furthermore, Xu *et al.* (2020, Fig. 6) show that $U = 2$ yields an intensity spectrum with $S_4 \approx 0.9$, a level associated with severe scintillation (HUMPHREYS *et al.*, 2010b, Section III, Subsection A).

Table 1 summarizes the weak and strong parameter sets. The CPSSM also includes a geometry-dependent time-scaling factor (scaling parameter) that varies across station–satellite links and drift velocities and is analyzed below.

Tabela 1 – Irregularity spectral parameters for the weak and strong scattering regimes in the CPSSM, where μ_{0y} is omitted for the weak (one-component) case because no spectral break is required.

Regime	U	μ_{0y}	p_1	p_2
Weak	0.05	–	3.00	3.00
Strong	2.00	0.55	2.45	3.70

3.1.7 Implementation of the CPSSM

An implementation of this model, originally named[2] TPPSM, was developed by Rino *et al.* from University of Colorado Boulder (JIAO *et al.*, 2018; XU *et al.*, 2020) to simulate ionospheric turbulence statistics. Their MATLAB and C code served as the basis for the algorithm developed in this thesis, but it was heavily refactored.

While the original code from University of Colorado Boulder is made publicly available in the following GitHub repositories:

- <https://github.com/cu-sense-lab/gnss-scintillation-simulator>;
- <https://github.com/cu-sense-lab/gnss-scintillation-simulator_2-param>,

the enhanced and refactored code (*vide* Section 5.2) used in this thesis is available at:

[2] The TPPSM is usually referred in the literature to as the model that represents the phase PSD as a two-component power law, which is more suitable for strong scattering regime (XU *et al.*, 2020, Section 1). Here, we refer to CPSSM as the general framework which does not only incorporate the TPPSM, but also the slip-step algorithm and the frequency extrapolation technique.

- <https://github.com/ita-gnss-lab/gnss-scintillation-simulator>.

3.2 The Cornell scintillation model

Although phase-screen-based models reduce computational cost, they require many physical parameters, which complicates automated simulation. Statistical models provide an alternative by generating a WSS process with specified PSD and PDF characteristics and applying it to the received signal.

3.2.1 Modeling the scintillation signal as a multiplicative disturbance

Kullstam e Keskinen (2000) modeled ionospheric scintillation by characterizing the received signal distribution at the antenna. The received power can be decomposed into a specular component and a random component arriving within an angular distribution around the LOS. Under forward scattering, the scintillation event does not affect the net received power. In other words, scintillation causes no loss in the transmitted signal power, but rather an angular redistribution around the circular antenna due to multipath scattering, which sooner or later will reach the receiver. Naturally, since no energy loss is involved, this model does not capture the refraction process when part of the electromagnetic wave is reflected to outer space. However, while the refraction effect through focusing and defocusing contributes to the overall scintillation effect, this phenomenon is only relevant when the difference in the plasma density is extremely high (KNIGHT, 2000).

Accordingly, scintillation can be modeled as a *time-varying multipath channel* with equivalent statistical properties. A time-varying multipath channel is characterized by Doppler and multipath spreads, or equivalently by the spaced-time and spaced-frequency correlation functions. Under forward scattering, Rayleigh's theorem implies that spectral energy is preserved (PROAKIS; SALEHI, 2007, Equation (2.1-19)), so the coherence bandwidth exceeds the signal bandwidth and the channel is effectively frequency-nonselective (flat fading) (PROAKIS; SALEHI, 2007, Section 13.2 *et seq.*). Consequently, over the bandwidth of interest the scintillation acts as a *multiplicative distortion of the baseband GNSS signal*, and the spaced-time correlation function captures the time variation of this multiplicative process, which follows a given distribution.

3.2.2 Distribution and correlation function for the scintillation signal

The amplitude and phase scintillation distributions have been extensively studied. Whitney *et al.* (1972) and Crane (1977) derived methods to compute the amplitude cumulative distribution function (CDF) from beacon observations. Comparisons between measured and theoretical distributions indicate that amplitude scintillation is well modeled by the Nakagami-*m* distribution, where the relationship $m = 1/S_4^2$ was initially proposed by Chytil (1967). The Nakagami-*m* PDF is given by (NAKAGAMI, 1960)

$$p(\gamma_s) = \frac{2m^m {\gamma_s}^{2m-1}}{\Gamma(m)\,\Omega^m} e^{\frac{-m{\gamma_s}^2}{\Omega}}, \tag{3.23}$$

where $\Omega = \mathrm{E}\left[{\gamma_s}^2(t)\right]$ is the scale parameter or second moment of $\gamma_s(t)$,

$$m = \frac{\Omega^2}{\mathrm{E}\left[\left({\gamma_s}^2(t) - \Omega\right)^2\right]}, \text{ for } m \geq \frac{1}{2} \tag{3.24}$$

is the fading figure, $\Gamma(\cdot)$ is the Gamma function, and $\gamma_s(t) \sim \text{Nakagami}(m, \Omega)$ is the *m*-distributed amplitude scintillation signal. For extreme scintillation events ($S_4 > 0.9$), the Rayleigh PDF provides a reasonable approximation since the Nakagami-*m* distribution approaches Rayleigh when $m = 1$ (AARONS, 1982). Methods for generating an *m*-distributed time series from Gaussian-distributed samples are discussed in Zhang (2000), Nunes e Sousa (2014a), Nunes e Sousa (2014b).

Fremouw *et al.* (1980) also provided an experimental statistical description of scintillation across Fresnel-zone regimes. They suggested the Nakagami-*m* distribution for amplitude scintillation and observed that the phase is well characterized by zero-mean Gaussian noise with variance ${\sigma_\phi}^2$.

Although hypothesis testing suggests that $\gamma_s(t) \sim \text{Nakagami}(m, \Omega)$ and $\phi_s(t) \sim \mathcal{N}\left(0, \sigma_\phi^2\right)$, later work has emphasized that amplitude and phase are not independent during deep fades. In equatorial data, Humphreys *et al.* (2010b) observed that deep fades ($> 15\,\text{dB}$) are usually accompanied by near-half-cycle phase changes with random sign. This behavior, termed "canonical fade", is a primary cause of phase unlocks and is not reproduced when amplitude and phase are generated independently, which can underestimate scintillation at high S_4 (HUMPHREYS *et al.*, 2009). When empirical records are time-shifted so that deep fades are not paired with phase changes, the probability of cycle slips decreases by 20 % (HUMPHREYS *et al.*, 2010a).

To address this limitation, the scintillation signal can be modeled as a nonzero-mean complex Gaussian process. Under forward scattering, multipath propagation yields an approximately normal[3] angular distribution around the LOS. As a consequence, amplitude scintillation can be modeled with a Rician distribution. Let

$$\psi_{\mathrm{s}}(t) = \psi_0 + \xi(t), \tag{3.25}$$

where $\psi_0 \triangleq \mathrm{E}[\psi_{\mathrm{s}}(t)] \in \mathbb{C}$ is a constant proportional to the LOS component and $\mathrm{E}[\cdot]$ denotes the statistical expectation operator. The stochastic process $\xi(t) \in \mathbb{C}$ represents the dispersive (multipath) component and is associated with the angular distribution observed at the receiver antenna. It is a WSS, complex-valued, zero-mean, colored Gaussian process with variance $2\sigma^2$ and autocorrelation function (ACF) given by (KULLSTAM; KESKINEN, 2000)

$$R_{\xi}(\tau) = 2\sigma^2 e^{-\frac{\tau}{\tau_0}}. \tag{3.26}$$

The decorrelation time τ_0 is defined as the lag at which the ACF decays to e^{-1}. This value usually varies from 2 s (for moderate scintillation) to 0.1 s (for strong scintillation) and depends on the signal frequency, season, geomagnetic latitude, and local time (HUMPHREYS *et al.*, 2010b).

Since $\psi_{\mathrm{s}}(t)$ is a nonzero-mean complex Gaussian process, its amplitude, $\gamma_{\mathrm{s}}(t) = |\psi_{\mathrm{s}}(t)| \in \mathbb{R}_+$, follows the Nakagami-$n$ (Rice) distribution (PROAKIS; SALEHI, 2007, p. 51),

$$p(\gamma_{\mathrm{s}}) = \frac{2(K+1)}{\Omega}\gamma_{\mathrm{s}} e^{-\frac{K+1}{\Omega}\left(\gamma_{\mathrm{s}}^2 + \frac{\Omega K}{K+1}\right)} I_0\left(2\gamma_{\mathrm{s}}\sqrt{\frac{K(K+1)}{\Omega}}\right), \tag{3.27}$$

where

$$\Omega = \mathrm{E}\left[\gamma_{\mathrm{s}}^2(t)\right] = 2\sigma^2(K+1) \tag{3.28}$$

is the scale parameter (which can be normalized to unity without loss of generality), $I_0(\cdot)$ is the modified Bessel function of the first kind and zero order, and

$$K = \frac{\sqrt{m^2 - m}}{m - \sqrt{m^2 - m}} = \frac{\sqrt{1 - S_4^2}}{1 - \sqrt{1 - S_4^2}}, \tag{3.29}$$

is the Rice factor, where the relationship with the scintillation index is defined by Shaft (1974).

[3] Considering circular antennas.

3.2.3 Implementation of the Cornell Scintillation Model

Humphreys *et al.* (2009) proposed a practical simulator that generates this scintillation signal by coloring complex discrete-time white Gaussian noise. The simulator is parameterized by the S_4 index and decorrelation time τ_0 and was used to test squaring-type PLLs, such as Costas loops. Gaussian, Butterworth, and f^{-4} filters were tuned so that $R_\xi(\tau_0)/R_\xi(0) = e^{-1}$, and chi-squared tests were used to assess goodness of fit. The Rician distribution performed slightly better than the Nakagami-*m* model. Because amplitude and phase are obtained from a single complex realization, the CSM captures canonical fades and is easier to implement than generating amplitude and phase independently (KNIGHT *et al.*, 1998).

For a sampling time of T, the computer-generated scintillation signal can be expressed as (HUMPHREYS *et al.*, 2009; LUCENA *et al.*, 2021)

$$\psi_\mathrm{s}(nT) = \gamma_\mathrm{s}(nT)\, e^{j\phi_\mathrm{s}(t)} = \psi_0 + \xi(nT), \tag{3.30}$$

where $\gamma_\mathrm{s}(t) \sim \mathrm{Rice}(\Omega, K)$, with the scale parameter (Ω) and Rice factor (K) given by Equations (3.28) and (3.29), respectively. It can be implemented by selecting S_4 and τ_0, computing K via (3.29), setting the nonspecular power to $2\sigma^2 = \frac{1}{1+K}$, and coloring the complex Gaussian component with a second-order low-pass Butterworth filter.

The simulation starts by generating a zero-mean white Gaussian noise and passing it through a second-order low-pass Butterworth filter whose transfer function is given by (INGLE; PROAKIS, 2000, Section 8.3)

$$|H(f)|^2 = \frac{1}{1 + \left(\frac{f}{f_{3\mathrm{dB}}}\right)^4}, \tag{3.31}$$

where $f_{3\mathrm{dB}}$ is the 3-dB cutoff frequency of the filter.

Since the two-sided PSD of the complex-valued zero-mean white Gaussian noise is N_0 and the cutoff frequency of the Butterworth filter is $f_{3\mathrm{dB}}$, the variance of the output signal is $\sigma^2 \approx 2 f_{3\mathrm{dB}} N_0$. The Butterworth filter output, denoted as $\tilde{\xi}(t) \in \mathbb{C}$, is added to the constant $\tilde{\psi}_0 = se^{\phi}$, where $s = \sqrt{2\sigma^2 K}$ is the specular component of the Rice distribution (PROAKIS; SALEHI, 2007, p. 50 *et seq.*), and ϕ is a constant phase factor drawn from $\mathcal{U}(-\pi, \pi)$ (LUCENA *et al.*, 2021). The resulting process $\tilde{\psi}_\mathrm{s}(t) = \tilde{\psi}_0 + \tilde{\xi}(t)$ is then normalized by its sample average, $\mu_\psi(t)$, thus producing $\psi_\mathrm{s}(t) = \psi_0 + \xi(t)$.

The ACF of $\xi(t)$ is given by (HUMPHREYS *et al.*, 2010a, Equation (15))

$$R_{\xi}(\tau) = \frac{1}{2}\mathrm{E}\left[\xi^{*}(t)\,\xi(t)\right] = \sigma^{2}\exp\left(-\beta\frac{|\tau|}{\tau_0}\right)\left[\cos\left(\frac{\beta\tau}{\tau_0}\right)+\sin\left(\frac{\beta|\tau|}{\tau_0}\right)\right], \tag{3.32}$$

where $\beta \triangleq 1.2396464$ so that $R_{\xi}(\tau_0)/R_{\xi}(0) = e^{-1}$ (HUMPHREYS *et al.*, 2010b). By setting β and defining a decorrelation time, τ_0, the cutoff frequency can be readily calculated as $f_{3\mathrm{dB}} = \beta/(\sqrt{2}\pi\tau_0)$ (HUMPHREYS *et al.*, 2009).

The generation of the scintillation signal by using the CSM model is shown in Figure 6.

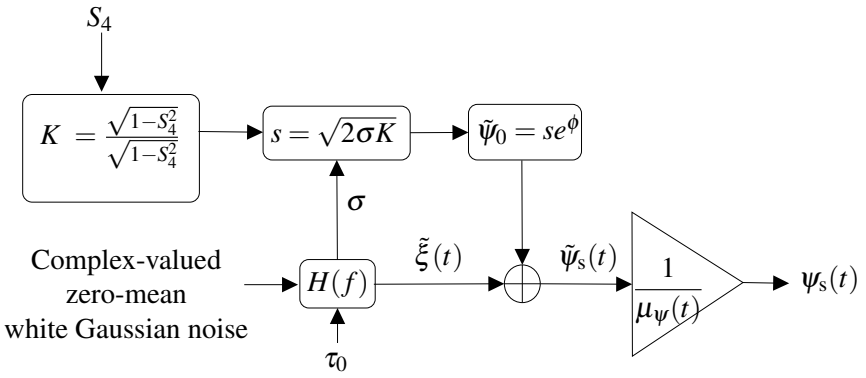

Figura 6 – The block diagram of the CSM.

The diagram is shown in continuous time, but it can be converted to discrete time using standard analog-to-digital mappings (*e.g.* impulse invariance or bilinear transformation) applied to the Butterworth prototype. The source code for the CSM, written in MATLAB by Humphreys *et al.* also from University of Colorado, is available at <https://gps.ece.cornell.edu/tools.php>.

The reader should note that the synthetic scintillation time series generated from a CSM-based simulator makes no distinction between the frequencies at which the signal is being impaired (RINO *et al.*, 2018). In other words, the CSM does not incorporate any frequency dependency in its formulation.

We define three different ionospheric scintillation severity parameters for the CSM usage, which are summarized in Table 2.

Tabela 2 – CSM configuration parameters for different scatter conditions.

Scatter condition	S_4	τ_0
Low scintillation intensity	0.5	0.7
Long-lasting scintillation activity	1	2
Strong scintillation intensity	0.9	0.2

While the first and third classes represent typical scintillation conditions observed *in situ*, the second class is less common and needs further explanation. Prolonged deep fades without abrupt phase changes are observed during intense scintillation events and under a specific geometry between the IPP drift velocity and the LOS, which depends only on the satellite trajectory for fixed monitoring stations (KINTNER *et al.*, 2004). When the irregularity moves in synchronism with the LOS geometry, scintillation can persist for up to tens of seconds, with fades lasting 2 s or longer (HUMPHREYS *et al.*, 2010b; KINTNER *et al.*, 2001). Accordingly, the second class can be interpreted as a long-lasting version of the third class (canonical fades).

4 CONVOLUTIONAL NEURAL NETWORKS FOR SCINTILLATION SIGNAL CHARACTERIZATION

This chapter presents a study on the application of CNNs for the characterization of ionospheric scintillation effects on GNSS signals. The algorithms introduced are the same as those presented in Pacelli *et al.* (2025b), Pacelli *et al.* (2024) and Pacelli *et al.* (2025, submitted only).

After a brief introduction to TSC, we describe the architectures proposed in the aforementioned articles, following the chronological and sequential evolution of the works. We start presenting a basic CNN architecture for scintillation TSC for single-frequency applications, followed by a more complex architecture for MC and MF classification of scintillation event, operating in multichannels. While the goal of initial efforts was to classify scintillation severity levels into discrete categories (*e.g.*, weak, moderate, or strong), a subsequent work employed the dimension-wise convolutional neural network (dCNN) model. Along with the dimension-wise class activation map (dCAM), the proposed model provides sample-level characterization of the scintillation effect, which enables to highlight specific segments within the time series that may cause cycle slips and loss of lock in GNSS receivers.

4.1 Introduction to time series classification

The basic work of TSC consists of assigning a label to a time series segment, indicating the class to which it belongs. In this context, a time series segment is defined as a sequence of observations that are temporally ordered. In a supervised training, each time series in the dataset contains a respective label indicating its class membership. Conversely, in an unsupervised training, the labels are not provided, and the algorithm must identify patterns and groupings within the data without prior knowledge of class assignments.

In general terms, four main categories for TSC can be identified:

- **distance-based methods**: such approaches rely on defining a distance measure to quantify the similarity between time series. The classification is then performed by comparing the distances between the input time series and a set of reference time series (or prototypes) for each class (WANG *et al.*, 2017). Classical algorithms in this class include *k*-nearest neighbour (NN), support vector classifier (SVC), and ensemble-based methods, where the distance or similarity used as figure of merit can be the Manhattan, Euclidean, Chebyshev distances, or the dynamic time warping (ZHAO *et al.*, 2017);

- **model-based methods**: the core idea is to train a generative model for each class, and then classify new time series based on the similarity of the data under each model (BAGNALL *et al.*, 2017; LÄNGKVIST *et al.*, 2014). Some examples in this category include Kernel methods (CHEN *et al.*, 2013), AR models (BAGNALL; JANACEK, 2014), and hidden Markov models (BAHL *et al.*, 1987), variational autoencoders or diffusion models;
- **feature-based methods**: this strategy uses discriminative deep learning models to minimize the classification error by learning a mapping from the input time series to the output labels. When a labeled dataset is available, the model learns in a supervised manner, adjusting its parameters to minimize the loss function that quantifies the difference between the predicted and true labels. After the training phase, the model can generalize the learned patterns to unseen examples and predict their class membership. Since the curse of dimensionality is an inherent challenge in multivariate time series, the usual approach is to reduce the dimensionality of the input to a feature vector, from which a final layer is used for the classification. Common model examples are autoencoders or CNNs (ZHAO *et al.*, 2017).
- **hypothesis-testing methods**: this is a classical approach commonly used in radar signal processing and detection theory, where the goal is to determine whether a given time series segment belongs to a particular class based on a statistical test. For instance, the NP detector is a widely used method for binary classification problems, where the likelihood ratio of the observed data under two hypotheses (*e.g.*, presence or absence of scintillation) is compared to a threshold to make a decision (KAY, 2009).

Distance-based methods, such as dynamic time warping, can capture intricate temporal dynamics to some extent, but they may have limited ability to represent higher-order temporal dependencies and cross-channel structure, especially in multichannel and MF settings (FAUVEL *et al.*, 2021, Section 2.2). Model-based methods, on the other hand, may struggle to accurately represent the complex and nonstationary nature of scintillation effects, which can vary significantly across different frequencies and constellations (ZHAO *et al.*, 2017). In fact, some results in the literature suggest that generative models, while useful for creating synthetic data, may not be as effective for classification tasks as feature-based models (FAWAZ *et al.*, 2019). Finally, the classical method for detecting scintillation events based on an assumed likelihood distribution, such as the NP detector, is still a viable approach. Moreover, a Bayesian framework can be adopted to incorporate prior knowledge about the process and decision costs,

thereby refining the estimates and providing a robust solution even under uncertainty. Although such Bayesian strategies excel in time-series estimation problems (FLORINDO *et al.*, 2025), they share a common restriction for detection and characterization: the limitation in identifying the underlying patterns in the scintillation signal that lead to the classification outcome. An additional problem is the assumption of a known distribution, which is usually difficult to obtain in practice due to the complex and nonstationary nature of scintillation effects. Conversely, feature-based methods have shown great promise in capturing complex temporal dependencies and cross-channel interactions in multivariate time-series data, making them well suited for scintillation signal characterization (ZHAO *et al.*, 2017). In particular, CNN architectures have an inherent ability to learn hierarchical feature representations from structured data, whether in temporal, spatial, or other dimensions. Therefore, this thesis focuses on feature-based methods, particularly those based on CNN architectures, to identify underlying patterns in the scintillation signal that can threaten the receiver's tracking loops.

4.2 Standard Convolutional Neural Networks

CNNs constitute a subclass of deep neural networks (DNNs) especially suited to grid-structured data, where the primary objective is to derive discriminative feature representations, used in this thesis for classification and *post-hoc* characterization. Convolutional layers apply learnable kernels across the input, enabling the network to capture hierarchical spatial patterns. Building on their success in image analysis, CNNs have been extended to time-series classification, where the input is a sequence of samples rather than a pixel array or tensor. Analogous to spatial correlations in images, temporal dependencies in one-dimensional time series can be exploited to extract informative features for classification. In the multivariate setting, CNNs can process all channels jointly by arranging them into a matrix in which each column corresponds to a distinct channel.

4.2.1 Input data structure

Let us consider the discriminative task of classifying an ionospheric scintillation event affecting N_{c} channels (coming from the DAQ) and lasting T_{sim} seconds, which correspond to N_{sim} samples. The captured time series segment is arranged into a simple example:

$$\mathbf{X}[k] = \begin{bmatrix} x[kN_{\text{sim}},1] & x[kN_{\text{sim}}+1,1] & \dots & x[kN_{\text{sim}}+N_{\text{sim}}-1,1] \\ x[kN_{\text{sim}},2] & x[kN_{\text{sim}}+1,2] & \dots & x[kN_{\text{sim}}+N_{\text{sim}}-1,2] \\ \vdots & \vdots & \ddots & \vdots \\ x[kN_{\text{sim}},N_{\text{c}}] & x[kN_{\text{sim}}+1,N_{\text{c}}] & \dots & x[kN_{\text{sim}}+N_{\text{sim}}-1,N_{\text{c}}] \end{bmatrix} \tag{4.1}$$

$$= \begin{bmatrix} \mathbf{x}[k,1] & \mathbf{x}[k,2] & \cdots & \mathbf{x}[k,N_{\text{c}}] \end{bmatrix}^{\top} \in \mathbb{R}^{N_{\text{c}} \times N_{\text{sim}}}, \tag{4.2}$$

where $\mathbf{x}[k,n_{\text{c}}] \triangleq \begin{bmatrix} x[kN_{\text{sim}},n_{\text{c}}] & x[kN_{\text{sim}}+1,n_{\text{c}}] & \cdots & x[kN_{\text{sim}}+N_{\text{sim}}-1,n_{\text{c}}] \end{bmatrix}^{\top} \in \mathbb{R}^{N_{\text{sim}}}$ and $x[k,n_{\text{c}}] = 10\log_{10}\left(|\hat{\psi}_{\text{s}}[k,n_{\text{c}}]|^2\right)$ is the signal intensity of the n_{c}th channel at the kth sample in decibels. A distinct approach adopted in this thesis is to apply the dB transformation to the signal intensity, which enhances the representation of variations in signal strength, particularly in scenarios where scintillation effects induce rapid fluctuations. This transformation aids the CNN in discerning subtle patterns associated with scintillation phenomena.

Let us consider a training in minibatches containing $N_{\text{b}} \in \mathbb{N}$ examples, then $\boldsymbol{\mathcal{X}}[i] \in \mathbb{R}^{N_{\text{b}} \times N_{\text{c}} \times N_{\text{sim}}}$ is the ith input tensor presented to the CNN, where the first mode stacks the examples in the minibatch. Therefore, $\boldsymbol{\mathcal{X}}_{u+1,:,:}[i] = \mathbf{X}_{1,:,:}[i+u] \in \mathbb{R}^{1 \times N_{\text{c}} \times N_{\text{sim}}}$, for $u \in \{0,1,\cdots,N_{\text{b}}-1\}$, where the right-hand side corresponds to the (4.1) reshaped as horizontal slice[1]. The CNN model processes the input, predicts the outputs for every example in the minibatch, computes the averaged minibatch loss, and updates the synaptic weights at every step $i = \lfloor k/N_{\text{b}} \rfloor$, which is obtained from the index k after stacking N_{b} examples ($\mathbf{X}[k]$'s) in the first mode of $\boldsymbol{\mathcal{X}}[i]$, being $\lfloor \cdot \rfloor$ the floor function.

4.2.2 Convolutional layer

The architecture of a CNN for TSC typically alternates convolutional and pooling layers, followed by one or more fully connected (FC) layers. The convolutional layers apply learnable kernel filters to the input, enabling the network to learn high-level hierarchies along the temporal and channel dimension. The pooling layers downsample the resulting feature maps, reducing dimensionality and letting the network focus on the most salient features. Finally, the FC layers aggregate these features to produce the classification output. Let $N_{\text{w}} \in \mathbb{N}$ be the number of learnable filters (or kernels) in the first convolutional layer, which equals the number of output channels or feature maps. The kernel matrices in this layer is represented by a single

[1] The reader is referred to Figure 1.3(a) in Ballard e Kolda (2025) for a visual understanding of a horizontal slice.

tensor $\boldsymbol{\mathcal{W}}[i] \in \mathbb{R}^{N_\mathrm{w} \times N_\mathrm{c} \times K_\mathrm{w}}$, where $K_\mathrm{w} \in \mathbb{N}$ is the kernel width[2] that multiplies the samples along the temporal dimension. For the n_bth example in the minibatch, the convolution output is

$$\tilde{\boldsymbol{\mathcal{O}}}_{n_\mathrm{b},n_\mathrm{w},n_\mathrm{o}}[i] = b_{n_\mathrm{w}}[i] + \boldsymbol{\mathcal{W}}_{n_\mathrm{w},:,:}[i] * \boldsymbol{\mathcal{X}}_{n_\mathrm{b},:,1+s(n_\mathrm{o}-1):K_\mathrm{w}+s(n_\mathrm{o}-1)}[i], \tag{4.3}$$

where $n_\mathrm{o} \in \left\{1,2,\ldots,N_\mathrm{o} = \left\lfloor \frac{N_\mathrm{sim}-K_\mathrm{w}}{s} \right\rfloor + 1\right\}$ is the output time index with $N_\mathrm{o} \in \mathbb{N}$ being the number of output samples after the convolutional layer, $s \in \mathbb{N}$ is the stride length, $n_\mathrm{w} \in \{1,2,\ldots,N_\mathrm{w}\}$ is the output channel index (*i.e.*, the number of kernels or feature maps), $b_{n_\mathrm{w}}[i] \in \mathbb{R}$ is the bias term associated with the n_wth filter, and $*$ denotes the cross-correlation operation, *i.e.*, elementwise product followed by summation over the resulting elements[3]. Although omitted for simplicity, a padding hyperparameter can also be included in (4.3) to, along with the stride, control the pace and area of the synaptic weights' local receptive fields, which modifies the output size N_o in $\tilde{\boldsymbol{\mathcal{O}}}[i] \in \mathbb{R}^{N_\mathrm{b} \times N_\mathrm{w} \times N_\mathrm{o}}$ (GOODFELLOW *et al.*, 2016). After the cross-correlation operation, a one-dimensional batch normalization layer is typically applied to the output tensor $\tilde{\boldsymbol{\mathcal{O}}}[i]$ to stabilize and accelerate the training process. This normalization standardizes the activations across the minibatch, ensuring that they have a mean of zero and a variance of one, which helps mitigate issues related to internal covariate shift (IOFFE; SZEGEDY, 2015). Afterwards, the rectified linear unit (ReLU) activation function is applied elementwise to introduce nonlinearity into the model, enabling it to learn complex patterns in the data (NAIR; HINTON, 2010).

4.2.3 Subsampling layer

The output of the activation function is then fed into a subsampling layer, which reduces the dimensionality of the feature maps while retaining the most salient information. A common approach is to use max pooling, where the maximum value within a specified window is selected, or average pooling, where the average value within the feature map window is computed. If $\boldsymbol{\mathcal{O}}[i] \in \mathbb{R}^{N_\mathrm{b} \times N_\mathrm{w} \times N_\mathrm{o}}$ is the output tensor after the activation function, the subsampling operation can be expressed as

$$\boldsymbol{\mathcal{P}}_{n_\mathrm{b},n_\mathrm{w},n_\mathrm{p}}[i] = g\left(\boldsymbol{\mathcal{O}}_{n_\mathrm{b},n_\mathrm{w},1+s(n_\mathrm{p}-1):N_\mathrm{pl}+s(n_\mathrm{p}-1)}[i]\right), \tag{4.4}$$

---

[2] Note that, differently from image applications, time series contain only width (*i.e.*, no height).

[3] Although the term "convolution" is widely used to refer to this operation in the deep learning (DL) literature, it is mathematically imprecise as the actual convolution operation involves flipping the kernel matrix with respect to the input, as shown in Equation (9.5) in Goodfellow *et al.* (2016). Since the learning process is insensitive to the flipping, the cross-correlation operation is adopted in most modern DL libraries, although "convolution" is carried in the name of CNNs (GOODFELLOW *et al.*, 2016, Section 9.1).

where $N_{\mathrm{pl}} \in \mathbb{N}$ is the pooling window size, $n_{\mathrm{p}} \in \left\{1, 2, \ldots, N_{\mathrm{p}} = \left\lfloor \frac{N_{\mathrm{o}} - N_{\mathrm{pl}}}{s} \right\rfloor + 1 \right\}$ denotes the temporal output samples, and $g(\cdot) : \mathbb{R}^{N_{\mathrm{pl}}} \to \mathbb{R}$ is the pooling function, which can be either the max or average operation. Therefore, the output tensor after the subsampling layer is $\boldsymbol{\mathcal{P}}[i] \in \mathbb{R}^{N_{\mathrm{b}} \times N_{\mathrm{w}} \times N_{\mathrm{p}}}$.

4.2.4 Bipyramidal effect and classification

Stacking multiple convolutional and subsampling layers allows the CNN to learn increasingly abstract and complex features from the input time series. As the data progresses through the layers, the temporal resolution (N_{o} or N_{p}) decreases[4] due to convolution and subsampling, while the number of feature maps (N_{w}) typically increases[4] as more filters are applied. This results in a bipyramidal structure, where the initial layers capture fine-grained temporal details, and deeper layers extract higher-level representations that has no temporal correlation (HAYKIN, 2009). This hierarchical feature extraction is crucial for effective time series classification, as it enables the network to discern patterns that are relevant for distinguishing between different classes of scintillation events. When the last subsampling layer reduces N_{o} to unity (or a sufficiently small value), the feature extraction is completed, that is, $\tilde{\boldsymbol{\mathcal{O}}}[i]$ is mapped to a N_{w}-dimensional feature space. This output passes through flattening and a FC layer to produce the logits $\tilde{\mathbf{Z}}[i] \in \mathbb{R}^{N_{\mathrm{b}} \times N_{\mathrm{cl}}}$, where $N_{\mathrm{cl}} \in \mathbb{N}$ is the number of classes. An activation function[5] is then applied elementwise to obtain the scintillation class probabilities, thus finishing the feedforward phase of the CNN.

4.2.5 Training, validation, and test

Before the next minibatch is processed, the backward phase occurs: for a supervised training, the N_{b} predicted outputs are compared to the ground-truth labels using a loss function $\mathcal{L}(\cdot)$, such as cross-entropy. For each loss, the backpropagation algorithm computes the local gradients with respect to the synaptic weights and biases in all layers. Then, an optimizer, such as stochastic gradient descent (SGD) or adaptive moment estimation (ADAM), uses the local gradients to update[6] the parameters. Once the entire training set has been processed, one epoch

[4] Although the layer index is avoided here to simplify the notation, the reader should be aware that N_{o}, N_{p}, and N_{w} may vary with the layer depth.

[5] Affine for regression, sigmoid for binary classification, and softmax for multiclass problems.

[6] Possibly, the optimizer state (*e.g.*, momentum/ADAM moments) or regularization (*e.g.*, weight decay/L_2) can also be used along with the local gradients to update the synaptic weights.

is completed, and the mean of all averaged minibatch losses is usually computed. Depending on the adopted methodology, a validation set can also be used to monitor the model's performance during training and observe whether an overfitting has occurred. When used, at the end of each epoch, the validation set is forward-propagated in minibatches, without updating the synaptic weights during this process (*i.e.*, without the backward phase), and the mean of all averaged minibatch losses is also computed. Training (and validation) spans N_e epochs, shuffling the order of examples in the dataset and obtaining the mean losses at each epoch. When the training is completed, the learning curve of the mean losses is plotted as a function of the epoch index. When the validation set is also used, two curves are obtained. Finally, the test set is used only once to evaluate the final model performance.

While some heuristic may also be adopted to refine the training (*e.g.*, early stopping based on the validation loss, learning rate scheduling, dropout, etc.), the general training procedure described above is widely used in the literature and does not significantly change with the adopted DL model (GOODFELLOW *et al.*, 2016).

4.3 Methodology to identify time series intervals in the scintillation signals that harm GNSS tracking loops

The first study on the application of CNN for scintillation TSC is presented in Pacelli *et al.* (2024), where a basic CNN architecture is proposed to classify scintillation severity levels in single-frequency GNSS signals, yet the main goal of this work is to identify time series segments that can potentially disrupt the GNSS receiver's tracking loops. On the one hand, extending the CNN model presented in Section 4.2 to MF inputs is as straightforward as adopting multiple channels related to the same satellite on different frequencies. On the other hand, it is still not clear how the classification task can be reformulated to highlight time series segments that may cause cycle slips and loss of lock in the receiver. To address this issue, the canonical fade and its implications for GNSS tracking loops is first discussed. Next, the class activation map (CAM) is introduced as a *post-hoc* tool to interpret the CNN decisions, allowing to spotlight the specific segments within the time series that are most influential in the classification outcome. Since the present thesis focuses on a multichannel approach containing signals from different frequencies and constellations, the dCAM tool is also presented to extend the CAM concept to capture the inter-channel activation maps, and the classical CNN is extended to a dCNN architecture to be used along with the dCAM.

4.3.1 Canonical fade and its role on tracking loop cycle slips

As observed in field testing, the primary cause of cycle slips in GNSS receivers during strong scintillation events is canonical fades, defined as sudden power fades ($> 15\,\mathrm{dB}$) accompanied by near-half-cycle phase changes (HUMPHREYS *et al.*, 2009). These events can lead to significant disruptions in the receiver's ability to maintain lock on the satellite signal, resulting in cycle slips and loss of lock. Empirical studies have shown that $90\,\%$ of equatorial-scintillation-induced cycle slips are associated with canonical fades (HUMPHREYS *et al.*, 2010a). Therefore, accurately identifying time segments in $x[i, n_c]$ featuring canonical fades is crucial for predicting and mitigating cycle slips in GNSS receivers. For this reason, the nonlinear preprocessing step to convert the signal intensity to dB scale, as described in Section 4.2, is essential to enhance the representation of rapid signal strength fluctuations associated with scintillation phenomena. Although the canonical fade definition involves both amplitude and phase variations, the focus on signal intensity in dB scale provides a practical approach to identify potential cycle slip-inducing segments in the time series data. The rationale is that significant power fades are often accompanied by phase changes, making the intensity-based analysis a valuable proxy for detecting canonical fades.

4.3.2 Class Activation Map and the dimensional-wise approach to identify canonical fades

CAM is a *post-hoc* interpretability technique that highlights the regions in the input data that are most influential in the model's decision-making process (ZHOU *et al.*, 2016). In the context of time series classification using CNNs, CAM can be employed to identify specific segments within the time series that contribute significantly to the classification outcome. This is particularly useful for understanding which parts of the scintillation-affected GNSS signals are most relevant for predicting cycle slips and loss of lock. Note that, differently from image applications, where the spatial dimensions are treated equally, all multivariate scintillation signals referred to the same temporal support as synchronization is assumed, but each channel represents a distinct frequency or constellation with unique scintillation features. Therefore, the dimensional-wise approach is particularly beneficial for ionospheric scintillation characterization as the contributing time series across channels is observed to be time-spaced from 3 to 5 s from each other due to the frequency dependence (JIAO *et al.*, 2016).

4.4 Convolutional neural networks and class activation map

In order to apply the CAM technique as a *post-hoc* interpretability tool, the CNN architecture must preserve the temporal resolution across all layers, ensuring that the output feature maps retain the same length as the input time series. This is achieved by eliminating pooling layers and adjusting the convolutional layers to use a stride of one with appropriate padding. Therefore, the operation described in Subsection 4.2.3 is omitted in the CNN architecture. Instead, the last convolutional, batch normalization, and activation layers produce feature maps with the same temporal resolution, which is passed to a global average pooling (GAP) layer which averages each feature map over the temporal dimension.

Let us denote the output of the last activation function layer as $\boldsymbol{\mathcal{O}}[i] \in \mathbb{R}^{N_\mathrm{b} \times N_\mathrm{w} \times N_\mathrm{sim}}$, where the correct stride and padding values make $N_\mathrm{o} \triangleq N_\mathrm{sim}$ to preserve the temporal resolution. The GAP layer computes the average of each feature map across the temporal dimension, resulting in

$$\check{\mathbf{Z}}_{n_\mathrm{b},n_\mathrm{w}}[i] = \langle \boldsymbol{\mathcal{O}}_{n_\mathrm{b},n_\mathrm{w},:}[i], \mathbf{1}_{N_\mathrm{sim}} \rangle, \tag{4.5}$$

where $\langle \cdot, \cdot \rangle$ denotes the inner product and $\mathbf{1}_{N_\mathrm{sim}} \in \mathbb{R}^{N_\mathrm{sim}}$ is a vector of ones. Next, the resulting matrix $\check{\mathbf{Z}}[i] \in \mathbb{R}^{N_\mathrm{b} \times N_\mathrm{w}}$ is passed through a FC layer with an activation function to produce the logits $\tilde{\mathbf{Z}}[i] \in \mathbb{R}^{N_\mathrm{b} \times N_\mathrm{cl}}$, where the classification probabilities are obtained by applying the activation function elementwise. Mathematically, this operation is expressed as[7]

$$\tilde{\mathbf{Z}}_{n_\mathrm{b},n_\mathrm{cl}}[i] = \left\langle \mathbf{W}_{n_\mathrm{cl},:}[i], \check{\mathbf{Z}}_{n_\mathrm{b},:}[i] \right\rangle, \tag{4.6}$$

where $\mathbf{W}[i] \in \mathbb{R}^{N_\mathrm{cl} \times N_\mathrm{w}}$ are the weights of the FC layer. Substituting (4.5) into (4.6), the logits can be rewritten as

$$\begin{aligned}
\tilde{\mathbf{Z}}_{n_\mathrm{b},n_\mathrm{cl}}[i] &= \sum_{n_\mathrm{w}=1}^{N_\mathrm{w}} \mathbf{W}_{n_\mathrm{cl},n_\mathrm{w}}[i] \left(\sum_{n_\mathrm{sim}=1}^{N_\mathrm{sim}} \boldsymbol{\mathcal{O}}_{n_\mathrm{b},n_\mathrm{w},n_\mathrm{sim}}[i] \right) \\
&= \sum_{n_\mathrm{sim}=1}^{N_\mathrm{sim}} \underbrace{\left(\sum_{n_\mathrm{w}=1}^{N_\mathrm{w}} \mathbf{W}_{n_\mathrm{cl},n_\mathrm{w}}[i] \boldsymbol{\mathcal{O}}_{n_\mathrm{b},n_\mathrm{w},n_\mathrm{sim}}[i] \right)}_{=\boldsymbol{\mathcal{A}}_{n_\mathrm{b},n_\mathrm{cl},n_\mathrm{sim}}[i]} \qquad (4.7) \\
&= \langle \boldsymbol{\mathcal{A}}_{n_\mathrm{b},n_\mathrm{cl},:}[i], \mathbf{1}_{N_\mathrm{sim}} \rangle, \qquad (4.8)
\end{aligned}$$

where $\boldsymbol{\mathcal{A}}[i] \in \mathbb{R}^{N_\mathrm{b} \times N_\mathrm{cl} \times N_\mathrm{sim}}$ in the CAM output tensor, containing the activation maps for each class along the temporal dimension for N_b examples. One can conclude that operations performed

[7] Ignoring the bias, which can be concatenated to the synaptic weights.

by the GAP (Equation (4.5)) FC (equation (4.6)) layer is equivalent to contracting $\mathbf{W}[i]$ and $\boldsymbol{\mathcal{O}}[i]$ is the second mode to obtain $\boldsymbol{\mathcal{A}}[i]$ (BALLARD; KOLDA, 2025, Definition 3.32), from which the logits are computed by averaging the activation maps over the temporal dimension. On the one hand, $\tilde{\mathbf{Z}}[i] \in \mathbb{R}^{N_\mathrm{b} \times N_\mathrm{cl}}$ passes through a softmax activation function to produce the scintillation class probabilities, where the highest probability indicates the predicted class. On the other hand, the predicted class for each example in the minibatch can be used to select the corresponding activation map from $\boldsymbol{\mathcal{A}}[i]$, which highlights the time series segments that most influenced the classification decision.

While CAM allows to identify specific intervals in the scintillation-affected GNSS signals that are likely to cause cycle slips and loss of lock in the receiver, $\boldsymbol{\mathcal{A}}[i]$ cannot directly capture the temporal dynamics across multiple channels. For instance, let us consider the CAM for the first example in the minibatch and the predicted class $c^\star$, then $\boldsymbol{\mathcal{A}}_{1,c^\star,:}[i] \in \mathbb{R}^{N_\mathrm{sim}}$ highlights the time steps that most influenced the classification decision. However, this activation map aggregates contributions from all channels, making it challenging to discern which specific channels were most influential at each time step.

4.4.1 Obtaining class activation map for each channel

An obvious solution to obtain the CAM for each channel is to apply the cross-correlation operation separately to each channel in (4.3). Considering time series as a special case of images containing only width as spatial dimension, the number of channels N_c coming from the DAQ would be equivalent to the number of image channels (*e.g.*, RGB). Under this analogy, the cross-correlation operation in the first layer, performed as

$$\tilde{\boldsymbol{\mathcal{O}}}_{n_\mathrm{b},n_\mathrm{w},n_\mathrm{c},n_\mathrm{o}}[i] = b_{n_\mathrm{w}}[i] + \boldsymbol{\mathcal{W}}_{n_\mathrm{w},n_\mathrm{c},:}[i] * \boldsymbol{\mathcal{X}}_{n_\mathrm{b},n_\mathrm{c},1+s(n_\mathrm{o}-1):K_\mathrm{w}+s(n_\mathrm{o}-1)}[i], \tag{4.9}$$

would produce the feature map for each channel separately in the third mode of $\tilde{\boldsymbol{\mathcal{O}}}[i] \in \mathbb{R}^{N_\mathrm{b} \times N_\mathrm{w} \times N_\mathrm{c} \times N_\mathrm{o}}$, where N_o is maintained equal to N_sim to preserve the temporal resolution throughout the layers.

The GAP and FC layers applied to the output of the last activation function layer

thus processed leads to

$$\begin{aligned}\tilde{\mathbf{Z}}_{n_\mathrm{b},n_\mathrm{cl}}[i] &= \sum_{n_\mathrm{c}=1}^{N_\mathrm{c}} \sum_{n_\mathrm{w}=1}^{N_\mathrm{w}} \mathcal{W}_{n_\mathrm{cl},n_\mathrm{c},n_\mathrm{w}}[i] \left(\sum_{n_\mathrm{sim}=1}^{N_\mathrm{sim}} \mathcal{O}_{n_\mathrm{b},n_\mathrm{w},n_\mathrm{c},n_\mathrm{sim}}[i] \right) \\ &= \sum_{n_\mathrm{sim}=1}^{N_\mathrm{sim}} \sum_{n_\mathrm{c}=1}^{N_\mathrm{c}} \underbrace{\left(\sum_{n_\mathrm{w}=1}^{N_\mathrm{w}} \mathcal{W}_{n_\mathrm{cl},n_\mathrm{c},n_\mathrm{w}}[i] \mathcal{O}_{n_\mathrm{b},n_\mathrm{w},n_\mathrm{c},n_\mathrm{sim}}[i] \right)}_{=\mathcal{A}_{n_\mathrm{b},n_\mathrm{cl},n_\mathrm{c},n_\mathrm{sim}}[i]} \\ &= \left\langle \mathcal{A}_{n_\mathrm{b},n_\mathrm{cl},:,:}[i], \mathbf{1}_{N_\mathrm{c}\times N_\mathrm{sim}} \right\rangle, \end{aligned} \tag{4.10}$$

where $\mathbf{1}_{N_\mathrm{c}\times N_\mathrm{sim}} \in \mathbb{R}^{N_\mathrm{c}\times N_\mathrm{sim}}$ is a matrix of ones and $\mathcal{O}[i] \in \mathbb{R}^{N_\mathrm{b}\times N_\mathrm{w}\times N_\mathrm{c}\times N_\mathrm{sim}}$ is obtained after passing $\tilde{\mathcal{O}}[i]$ through the batch normalization and activation function layers. Now, $\mathcal{A}[i] \in \mathbb{R}^{N_\mathrm{b}\times N_\mathrm{cl}\times N_\mathrm{c}\times N_\mathrm{sim}}$ contains the activation maps for each class along both the channel and temporal dimensions for N_b examples. In the image analogy, this architecture, referred to as cCNN and proposed by Boniol *et al.* (2022), is able to capture the regions in the input data that are most influential across the red, green, and blue channels, separately. While this might not be necessary for some image applications, it is crucial for the present application since each channel represents a distinct frequency or constellation with unique scintillation features.

The clear disadvantage of the cCNN model is that no inter-channel relationships are learned during the convolution operation, as each channel is processed independently and aggregated only in the end, during the FC layer operation for the final classification. In fact, what one seeks in inherently conflicting: learn from all channels jointly, yet interpret the contribution of each channel separately.

The cCNN limitation is particularly significant in the context of ionospheric scintillation characterization, where cross-frequency interactions can provide valuable insights into the underlying scintillation phenomena. To overcome this problem, the dCNN architecture, also proposed by Boniol *et al.* (2022), is explored. This model extends the standard CNN by incorporating inter-channel relationships during the convolution operation while still enabling the extraction of dimensional-wise activation maps through the dCAM technique.

4.4.2 Dimensional-wise convolutional networks and class activation maps

On the one hand, the standard CNN architecture processes multichannel time series in a unique order (*vide* (4.2)) to learn the inter-channel relationship, but provides only one overall CAM for all channels. On the other hand, the dCNN explores how the channel order affect the learning process to extract the CAM for each channel, yet still learning from all channels jointly.

For that, instead of (4.1), the input time series can be rearranged as

$$\boldsymbol{\mathcal{C}}[k] = \begin{bmatrix} \mathbf{x}_{1,1,:}[k,N_\mathrm{c}] & \mathbf{x}_{1,1,:}[k,1] & \dots & \mathbf{x}_{1,1,:}[k,N_\mathrm{c}-1] \\ \vdots & \vdots & \ddots & \vdots \\ \mathbf{x}_{1,1,:}[k,2] & \mathbf{x}_{1,1,:}[k,3] & \dots & \mathbf{x}_{1,1,:}[k,1] \\ \mathbf{x}_{1,1,:}[k,1] & \mathbf{x}_{1,1,:}[k,2] & \dots & \mathbf{x}_{1,1,:}[k,N_\mathrm{c}] \end{bmatrix} \in \mathbb{R}^{N_\mathrm{c}\times N_\mathrm{c}\times N_\mathrm{sim}}. \tag{4.11}$$

Note that $\mathbf{x}_{1,1,:}[k,n_\mathrm{c}] \in \mathbb{R}^{1\times 1\times N_\mathrm{sim}}$ represents the time series of the n_cth channel reshaped as a tube fiber[8] (*i.e.*, mode-3 fiber), orthogonal to the plane page (BALLARD; KOLDA, 2025, Section 1.3). Figure 7 illustrates the structure of the input tensor.

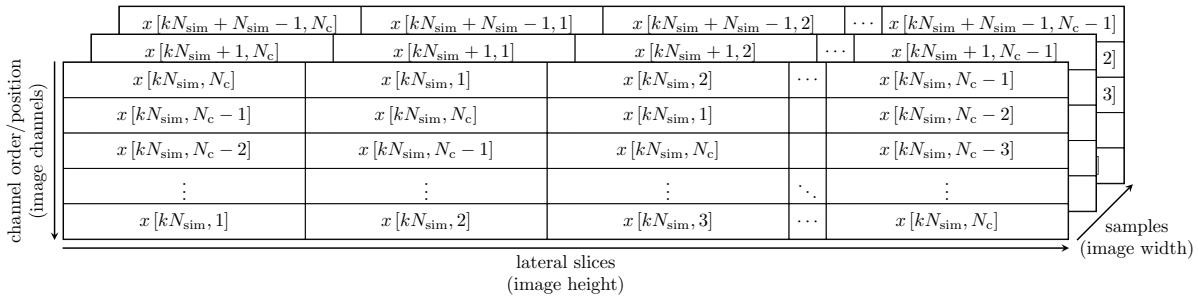

Figura 7 – Three-dimensional representation of $\boldsymbol{\mathcal{C}}[k] \in \mathbb{R}^{N_\mathrm{c}\times N_\mathrm{c}\times N_\mathrm{sim}}$. The arrows indicate the increasing mode indices. The analogy with the image structure is put in parenthesis. Note that $\boldsymbol{\mathcal{C}}[k]$ is structured following the Pytorch convention for images, *i.e.*, [channels × height × width].

With the dimensional-wise rearrangement in (4.11), the analogy to images is now complete in the sense that the input data contains both height ($= N_\mathrm{c}$) and width ($= N_\mathrm{sim}$) residing in the second and third modes of the input tensor, respectively, while the first mode is the channel ($= N_\mathrm{c}$) dimension. Therefore, the kernel matrices follow the same logic as in 2D image applications, where each kernel slides over both height and width dimensions with a local receptive field of size K_h and K_w, respectively. However, the key difference from images is that we do not want to aggregate the input data across the height dimension, since each slice along this mode represents a distinct channel order. Therefore, if all kernel matrices in the first convolutional layer are represented by a single tensor[9] $\boldsymbol{\mathcal{W}}[i] \in \mathbb{R}^{N_\mathrm{w}\times N_\mathrm{c}\times K_\mathrm{h}\times K_\mathrm{w}}$, we set $K_\mathrm{h} \triangleq 1$, and convolution operation in this layer reads

$$\tilde{\boldsymbol{\mathcal{O}}}_{n_\mathrm{b},n_\mathrm{w},n_\mathrm{c},n_\mathrm{o}}[i] = b_{n_\mathrm{w}}[i] + \boldsymbol{\mathcal{W}}_{n_\mathrm{w},:,1,:}[i] * \tilde{\boldsymbol{\mathcal{C}}}_{n_\mathrm{b},:,n_\mathrm{c},1+s(n_\mathrm{o}-1):K_\mathrm{w}+s(n_\mathrm{o}-1)}[i], \tag{4.12}$$

[8] The reader is referred to Figure 1.4(c) in Ballard e Kolda (2025) for a visual understanding of a tube fiber.

[9] The kernel tensor is organized as [number of feature maps (or kernels, which equals the number of output channels) × number of input channels × height of the local receptive field × width of the local receptive field]. Note that the tensor $\boldsymbol{\mathcal{W}}[i]$ representing the kernel matrices follows the Pytorch convention.

where $\tilde{\mathcal{C}}[i] \in \mathbb{R}^{N_\mathrm{b}\times N_\mathrm{c}\times N_\mathrm{c}\times N_\mathrm{sim}}$ is the ith data presented to the network, where its first mode stacks the N_b $\mathcal{C}[k]$'s, that is, $\tilde{\mathcal{C}}_{u+1,:,:,:}[i] = \mathcal{C}[iN_\mathrm{b}+u]$, for $u \in \{0,1,\cdots,N_\mathrm{b}-1\}$. Each resulting feature map is stored in the third mode of $\tilde{\mathcal{O}}[i] \in \mathbb{R}^{N_\mathrm{b}\times N_\mathrm{w}\times N_\mathrm{c}\times N_\mathrm{o}}$, which represents the output channel. The stride and padding are adjusted to preserve the temporal resolution, *i.e.*, $\tilde{\mathcal{O}}[i] \in \mathbb{R}^{N_\mathrm{b}\times N_\mathrm{w}\times N_\mathrm{c}\times N_\mathrm{sim}} \therefore N_\mathrm{o} \triangleq N_\mathrm{sim}$. Therefore, treating the input data as an image, $\tilde{\mathcal{O}}[i]$ contains the same resolution as $\tilde{\mathcal{C}}[i]$, that is, a height and width of N_c and N_sim, respectively, but the number of channels has changed from N_c to N_w. From (4.12), one notes that the input channels of $\mathcal{W}[i]$ (its second mode) learns from all channels of $\tilde{\mathcal{C}}[i]$ (its second mode) jointly. Also note that the n_cth height and n_wth channel of the output image $\tilde{\mathcal{O}}[i]$ (corresponding respectively to its third and second mode) result from the cross-correlation between n_wth kernel matrix and the n_cth lateral slice[10] of $\mathcal{C}[k]$ across all channels in a specific order (*vide* Figure 7). Therefore, the dCNN works in some redundancy as each kernel matrix is applied N_c times to the same set of multivariate time series but in N_c different orderings, and each result is embedded in the height dimension of the image $\tilde{\mathcal{O}}[i]$.

The logits calculated after passing $\tilde{\mathcal{O}}[i]$ through the batch normalization and activation function layers, followed by the GAP and FC neural Networks, is identical to (4.10), with the a fundamental difference in the meaning of $\mathcal{A}[i] \in \mathbb{R}^{N_\mathrm{b}\times N_\mathrm{cl}\times N_\mathrm{c}\times N_\mathrm{sim}}$: if $c^\star$ the predicted class in the first example in the minibatch, then $\mathcal{A}_{n_{\mathrm{b},c^\star,n_{\mathrm{c},:}}}[i]$ does not provide the activation map for channel n_c. Rather, it highlights degree of importance of the time series segments for all channels in *that* specific channel order, learned during the cross-correlation operation. In other words, varying n_c in $\mathcal{A}_{n_{\mathrm{b},c^\star,n_{\mathrm{c},:}}}[i]$ shows how the time series segments contributed to the classification decision changes when the channels order is changed.

4.4.3 Augmenting the CAM to obtain position-dependent channel contributions

Let $p[j]$ be a N_c-tuple containing a specific order of channel indices, where $j \in \{1,2,\ldots,N_\mathrm{c}!\} = \mathcal{P}$. For instance, $p[1] = (1,2,\cdots,N_\mathrm{c})$, $p[2] = (2,1,3,4,\cdots,N_\mathrm{c})$, and so on. If $\mathbf{P}[j] \in \mathbb{R}^{N_\mathrm{c}\times N_\mathrm{c}}$ is the permutation matrix that rearranges the rows from $p[1]$ to $p[j]$ (STRANG, 2019, Section 2.3), then

$$\mathcal{C}[i,j] = \mathcal{C}[i] \times_1 \mathbf{P}[j] \in \mathbb{R}^{N_\mathrm{c}\times N_\mathrm{c}\times N_\mathrm{sim}}, \tag{4.13}$$

[10] The reader is referred to Figure 1.3(b) in Ballard e Kolda (2025) for a visual understanding of a lateral slice.

where $\times_1$ denotes the tensor-times-matrix (TTM) product[11] along the first mode (BALLARD; KOLDA, 2025, Section 3.3). Note that $\mathcal{C}[i,j]$ is simply $\mathcal{C}[i]$ with its horizontal slices rearranged according to $p[j]$. Likewise, the CAM tensor $\mathcal{A}[i,j]$ is obtained by passing $\mathcal{C}[i,j]$ through the dCNN architecture.

Let us focus on the subarray $\mathbf{A}[i,j] \triangleq \mathcal{A}_{n_\mathrm{b},c^\star,:,:}[i,j] \in \mathbb{R}^{N_\mathrm{c}\times N_\mathrm{sim}}$, which contains the activation maps for all channel orders along the temporal dimension for the n_bth example in the minibatch and the predicted class $c^\star$. The augmented CAM reads (BONIOL *et al.*, 2022)

$$\tilde{\mathcal{A}}[i,j] = \begin{bmatrix} \mathbf{A}_{g(1,1),1,:}[i,j] & \mathbf{A}_{g(1,2),1,:}[i,j] & \cdots & \mathbf{A}_{g(1,N_\mathrm{c}),1,:}[i,j] \\ \mathbf{A}_{g(2,1),1,:}[i,j] & \mathbf{A}_{g(2,2),1,:}[i,j] & \cdots & \mathbf{A}_{g(2,N_\mathrm{c}),1,:}[i,j] \\ \vdots & \vdots & \ddots & \vdots \\ \mathbf{A}_{g(N_\mathrm{c},1),1,:}[i,j] & \mathbf{A}_{g(N_\mathrm{c},2),1,:}[i,j] & \cdots & \mathbf{A}_{g(N_\mathrm{c},N_\mathrm{c}),1,:}[i,j] \end{bmatrix} \in \mathbb{R}^{N_\mathrm{c}\times N_\mathrm{c}\times N_\mathrm{sim}}, \tag{4.14}$$

where $g:\mathbb{N},\mathbb{N}\to\mathbb{N}$ is a function that maps the 2-tuple (a,b) to the natural number representing the one-indexed position of $x[kN_\mathrm{sim},a]$ in $\mathcal{C}_{:,b,1}[i,j] \in \mathbb{R}^{N_\mathrm{c}}$. For instance, since $p[1] = (1,2,3,4,\cdots,N_\mathrm{c})$, then $\mathcal{C}[i,j=1] \triangleq \mathcal{C}[i]$, whose data are structured as shown in Figure 7. In this case, $g(1,3) = 2$ as $\mathcal{C}_{2,3,1}[i] = x[kN_\mathrm{sim},1]$. In (4.13), $\mathbf{A}_{a,1,:}[i,j] \in \mathbb{R}^{1\times 1\times N_\mathrm{sim}}$ is the ath row of $\mathbf{A}[i,j]$ reshaped as a tube fiber, with singletons in its first two modes. Note that the n_cth horizontal slice of $\tilde{\mathcal{A}}[i,j]$ contains the activation maps for the n_cth channel across all the N_c possible positions, sequentially organized in the columns and with the samples along the depth.

4.4.4 Merging random permutations to obtain dimensional-wise channel contributions

The key idea behind the dCAM technique is to train the dCNN with $\mathcal{C}[i,j=1] \triangleq \mathcal{C}[i]$, but explores the different channel orders at *post hoc* to obtain the dimensional-wise channel contributions from $\tilde{\mathcal{A}}[i,j]$. A major limitation is that, since $|\mathcal{P}| = N_\mathrm{c}!$, the number of possible permutations grows factorially with the number of channels. To make the computation feasible, a random subset of $N_\mathrm{pm} \ll |\mathcal{P}| = N_\mathrm{c}!$ possible permutations is selected from $\mathcal{P}$, denoted as $\tilde{\mathcal{P}} \subset \mathcal{P}$. The averaged result reads

$$\bar{\mathcal{A}}[i] = \frac{1}{N_\mathrm{pm}} \sum_{\forall j\in\mathbb{N}\,|\,p[j]\in\tilde{\mathcal{P}}} \tilde{\mathcal{A}}[i,j]\,. \tag{4.15}$$

The vector $\bar{\mathcal{A}}_{n_\mathrm{c},a,:}[i] \in \mathbb{R}^{N_\mathrm{sim}}$ corresponds to the averaged activation map when the channel $n_\mathrm{c} \in \{1,2,\cdots,N_\mathrm{c}\}$ is placed in position $a \in \{1,2,\cdots,N_\mathrm{c}\}$ across all random permutations

[11] If $\mathcal{A} \in \mathbb{R}^{I_1\times I_2\cdots\times I_N}$, $\mathbf{U} \in \mathbb{R}^{J_n\times I_n}$, and $\mathcal{B} = \mathcal{A}\times_n \mathbf{U}$, then $\mathcal{B}_{i_1,i_2,\cdots,i_{n-1},j_n,i_{n+1},\cdots,i_N} = \sum_{i_n=1}^{I_n} \mathcal{B}_{i_1,i_2,\cdots,i_N}\mathbf{U}_{j_n,i_n}$, and $\mathcal{B} \in \mathbb{R}^{I_1\times I_2\cdots\times I_{n-1}\times J_n\times I_{n+1}\times\cdots\times I_N}$.

in $\tilde{\mathcal{P}}$. For a sufficiently large N_{pm}, it is expected that every tube fiber in $\tilde{\boldsymbol{\mathcal{A}}}[i,j]$ is very similar, and that

$$\bar{\mathbf{A}}_{(3)}[i]\,\mathbf{1}_{N_{\text{c}}^2} = \sum_{p=1}^{N_{\text{c}}} \sum_{n_{\text{c}}=1}^{N_{\text{c}}} \bar{\boldsymbol{\mathcal{A}}}_{n_{\text{c}},p,:}[i] \tag{4.16}$$

is approximately equal to the overall CAM obtained from the standard CNN approach for TSC (*vide* $\boldsymbol{\mathcal{A}}_{n_{\text{b}},n_{\text{cl}},n_{\text{sim}}}[i]$ in (4.7)), where $\bar{\mathbf{A}}_{(3)}$ is the mode-3 unfolding of $\bar{\boldsymbol{\mathcal{A}}}[i]$. However, for a given n_{c}, if the $p^{\star}$th position significantly varies the activation map compared to other positions, then one can conclude that channel n_{c} has a strong influence on the classification decision when placed in position $p^{\star}$. The method here described to compute the dCAM, proposed by Boniol *et al.* (2022), provides a way to assess the position-dependent contributions of each channel to the classification decision, while still learning from all channels jointly during the training phase. The dimensional-wise contribution is extracted simply by computing the variance around $\bar{\mathbf{A}}_{(3)}[i]\,\mathbf{1}_{N_{\text{c}}^2}$ for all positions of a given channel.

5 RESULTS

This chapter presents the results obtained from the experiments conducted to evaluate the performance of the proposed CNN models for scintillation classification. The results shown here are the same as those presented in Pacelli *et al.* (2025b), Pacelli *et al.* (2024) and (PACELLI *et al.*, 2025). Each section focuses on different simulation results and is introduced in chronological order, starting from the initial model development to the final evaluation of the CNN models.

5.1 Classifying CSM-generated scintillation signals with CNN

This section presents the results obtained from the initial experiments using CNN models to classify scintillation signals generated by the CSM.

5.1.1 Training parameters

The primary objective of these experiments was to assess the viability of the standard CNN model, presented in Section 4.2, to classify a single scintillation time series into three scintillation intensity levels. For that, a computer simulation was performed to generate synthetic scintillation signals using the parameters defined in Table 2. Each time series instance is labeled according to its scintillation intensity level and is disposed as a two-channel (amplitude and phase) input to the CNN model, as shown in (4.1). However, instead of using the raw scintillation signal for the classification task, a noisy version of the signal was created by adding AWGN at different variance levels, calculated as a percentage of the scintillation signal variance. The simulation parameters used to generate the dataset and to train the model are summarized in Table 3.

5.1.2 Standard CNN architecture

Table 4 shows the CNN architecture with the number of parameters in each layer. Note that the input layer has the same shape as $\mathbf{X}[k] \in \mathbb{R}^{300\times 2}$, as shown in (4.1). As $\mathbf{X}[k]$ progresses through the convolutional layers, the feature dimension (second mode of each output size) increases, while the temporal dimension (first mode of each output size) decreases. All convolutional layers use ReLU activations to mitigate the vanishing gradient problem.

Tabela 3 – Simulation parameters used to generate the CSM-based dataset for CNN training and evaluation.

Parameter	**Value**
Number of realizations or independent runs	20
Number of epochs	100
Number of instances or examples	3000
Time series length per example	$N_{\text{sim}} = 300$
Training/test split ratio	$80\%/20\%$
Number of examples for the training and test sets	2400, 600
Sampling time of the scintillation signal	$T = 100\,\text{ms}$
Mini-batch size	$N_{\text{b}} = 4$
Number of channels	$N_{\text{c}} = 2$ (amplitude and phase)
Convolution + sub-sampling layer pairs	2
Pooling strategy	Average pooling
FC layer's activation function	ReLU
Estimation noise levels	0%, 10%, 50% of the scintillation signal variance

Tabela 4 – Architecture of the CNN model.

Layer	**Output size**	**Number of parameters**
Input layer	300×2	0
1st convolutional layer	294×6	90
1st pooling layer	98×6	0
2nd convolutional layer	92×12	516
2nd pooling layer	30×12	0
Flattening	360	0
FC	3	1083

Since the pooling layers only reduce the temporal dimension, the feature dimension remains unchanged after each operation. Moreover, no parameters are learned in the pooling layers, as only downsample is performed. For this model, average pooling is used.

The flattening layer reshapes the output of the last pooling layer into a one-dimensional feature vector, which is then passed to the FC layer containing most of the CNN parameters. Depending on the task, the FC layer can apply either a sigmoid for binary classification or a softmax for multiclass classification. Here, a softmax is applied.

5.1.3 Learning curves

Figure 11 presents the learning curves obtained during training, for each noise level. The curves are plotted for each realization, and an average curve across realizations is also computed. The results indicate that the estimation noise does not interfere with the learning

process, and that the model learns features from the input signal in approximately 40 epochs for every noise level.

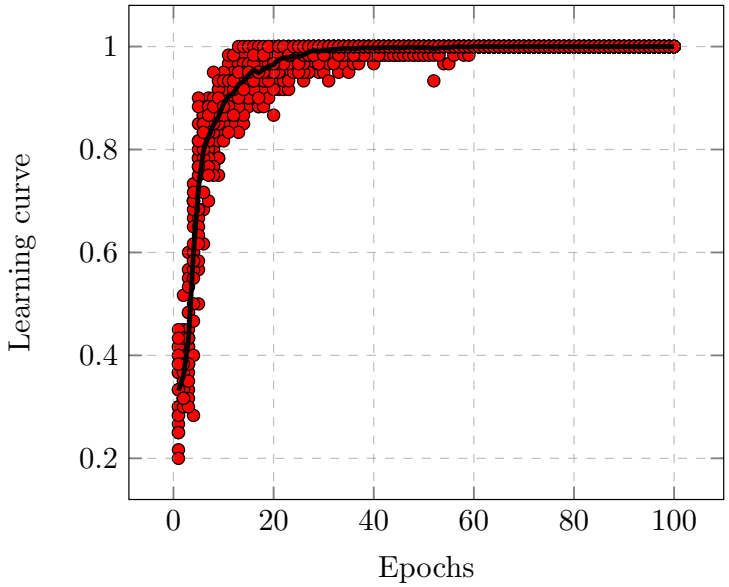

(a) 0% of the scintillation signal variance (noiseless condition).

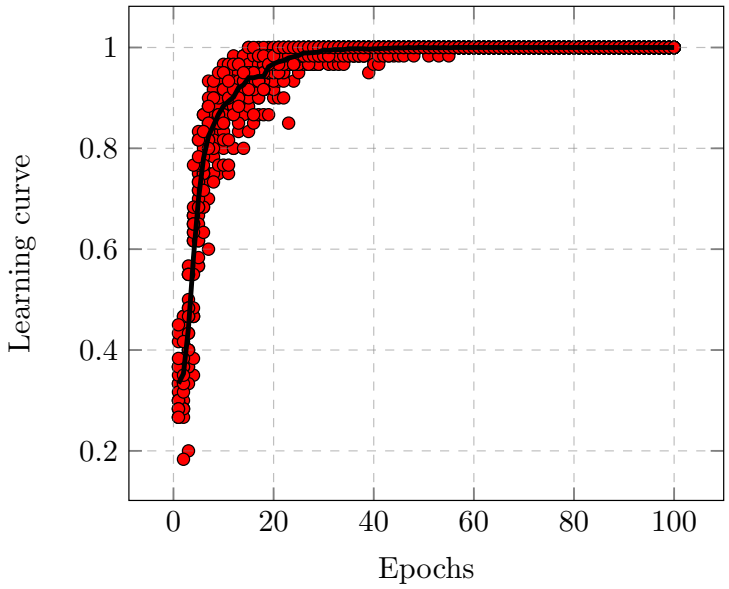

(b) 10% of the scintillation signal variance.

5.1.4 Test set accuracy

After 20 realizations, Table 5 reports the mean test set accuracy and its standard deviation for each estimation noise level. With perfect signal estimation (*i.e.*, no AWGN), the average accuracy is 91.06%, which drops to 81.88% when the estimated signal is corrupted by

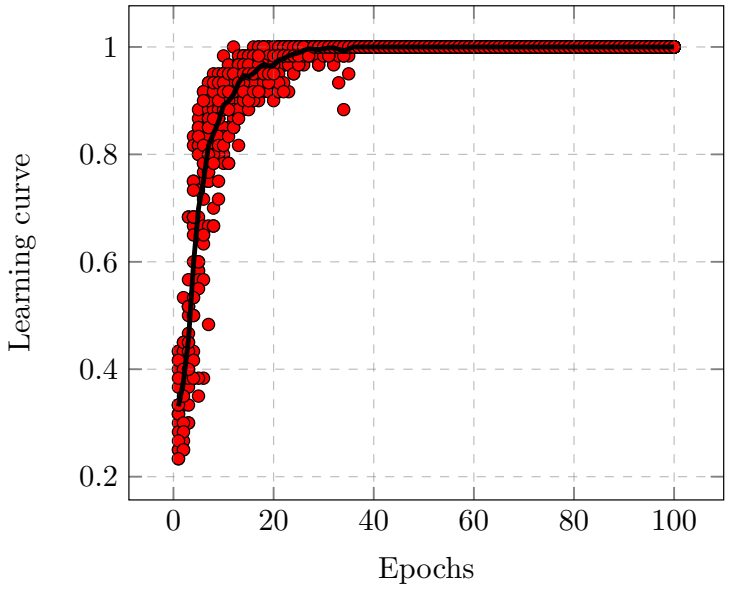

(c) 50% of the scintillation signal variance.

Figura 8 – Learning curve.

noise whose variance is 50% of the variance of the scintillation signal, indicating that the model is robust to moderate levels of estimation noise.

Tabela 5 – Average and standard deviation of the test accuracy for each estimation noise level.

Estimation noise (%)	Accuracy (%)	Standard deviation (%)
0	91.06	1.66
10	85.19	2.41
50	81.88	1.70

5.1.5 Confusion matrices

Figure 9 shows the confusion matrices for each estimation noise level. The top plot (Figure 9a) corresponds to a noise of 0%; such noise-free estimates enable the CNN to clearly cases where the plasma travels in synchronism with the IPP from canonical fades, corresponding to classes 2 and 3. As estimation noise increases (Figures 9b and 9c), correctly identifying both classes becomes more challenging, and the model increasingly assigns instances to class 1 to preserve overall accuracy. This effect is reflected in class 2, where the F_1 score drops from 0.87 in Figure 9a to 0.77 in Figure 9b and 0.75 in Figure 9c.

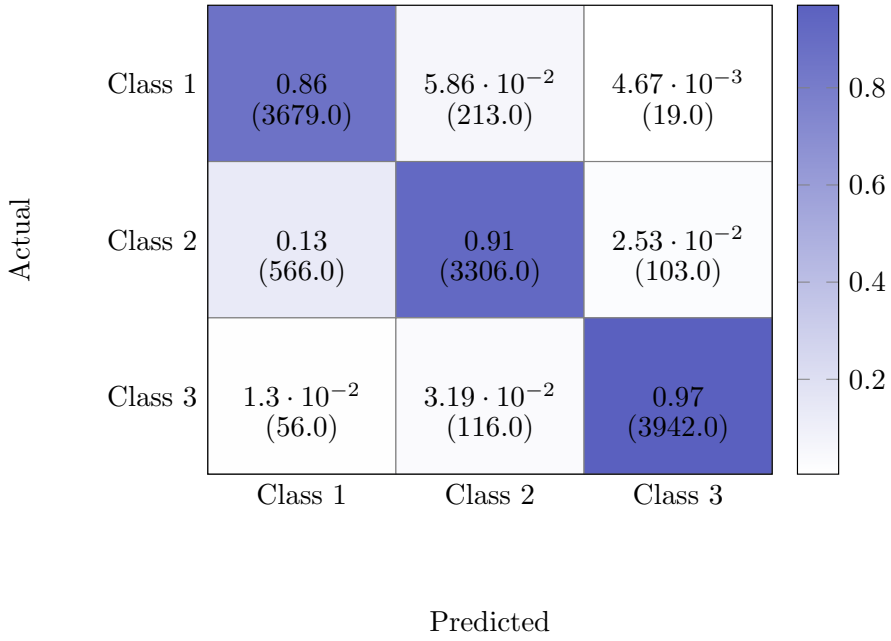

(a) 0%.

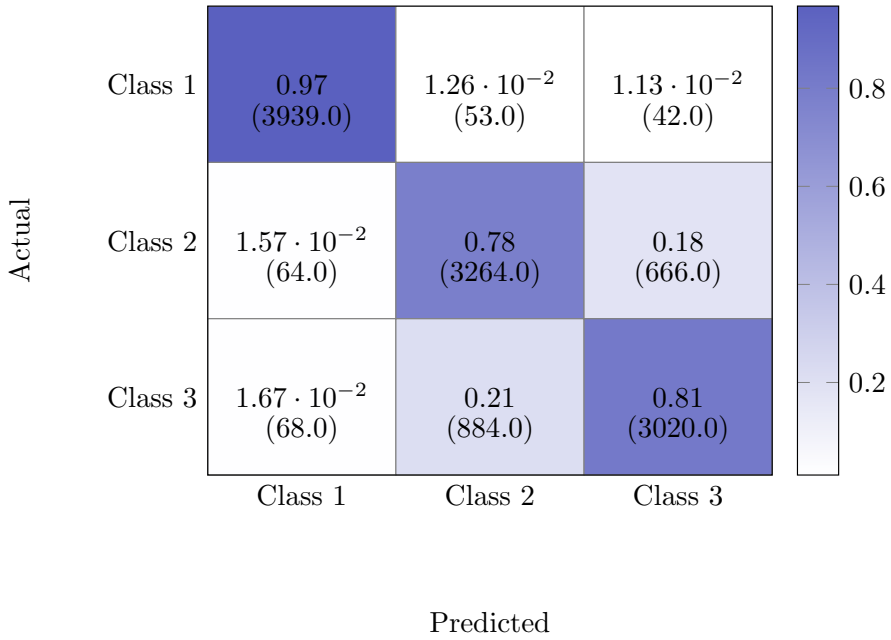

(b) 10%.

5.2 Implementation of the CPSSM

Pacelli e Florindo (2025, v2.1) have refactored a MATLAB and C implementation of the CPSSM, used to generate the scintillation time series. The implementation extends the source code originally developed by Rino *et al.* (2018), who implemented the TPPSM to simulate ionospheric turbulence statistics using a power-law profile. From this initial codebase, the following features were added:

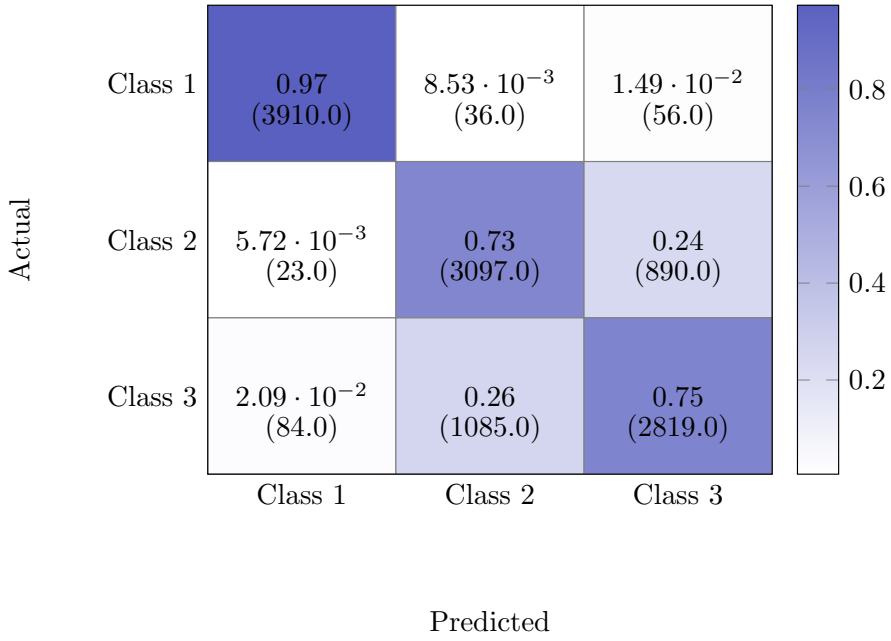

(c) 50%.

Figura 9 – Confusion matrix. Each value is normalized by the total number for the predicted class, which is the sum of the values shown within parentheses.

- support for MC ephemerides from RINEX (Receiver independent exchange format) navigation files in its version 3.xx;
- in addition to global positioning system (GPS), Galileo is now also supported as a constellation option;
- integration of the MATLAB source code implemented by Jiao *et al.* (2017) to simulate scintillation time series for dynamic platforms (although it was not used in this thesis experiments due to the context of fixed monitoring stations);
- computation of LOS satellite trajectories for a given monitoring station over the simulation interval, providing a realistic satellite-receiver geometry for multiple satellites in-view (see Figure 10 as an example obtained from the simulator);
- automatic plot of the the simulated intensity and phase PSD of the scintillation time series, as well as the theoretical[1] post-propagated intensity PSD curve.

While these new features were added to the simulator, the core theoretical basis of the TPPSM to describe the phase screen PSD and the split-step idea remained unchanged. Since there is no consensus[2] in the literature on how to call the complete framework proposed by Rino *et al.* (2018), we refer to this model as CPSSM in this thesis. The simulator contains

[1] The authors claim only the integration of automatic plotting for multiple satellites as a new feature. The original source code for the theoretical PSD intensity, written in C by Carrano (2016), was maintained as it was.

[2] *Vide* Table 1 in Vasylyev *et al.* (2022).

Figura 10 – Example of satellite trajectories in LOS with a given station during the simulation period. The curves in blue represent the satellite trajectories, while the red dot indicates a monitoring station located in São José dos Campos. Only those satellites that are in LOS during the entire window time are considered for simulation.

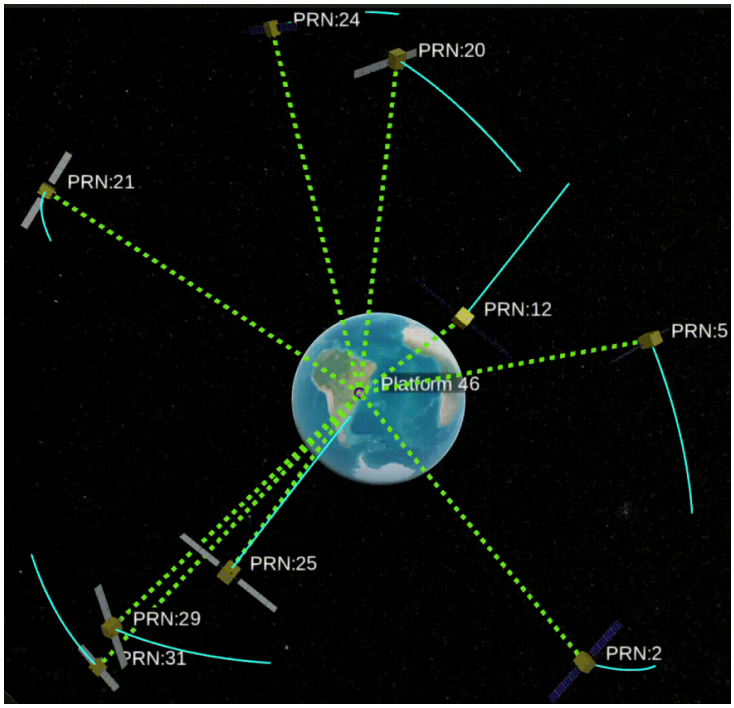

Fonte: Pacelli e Florindo (2025, v2.1).

the following input parameters: (i) scintillation event duration T_{sim}; (ii) correlation length T, which defines the sampling time of the time series; (iii) carrier frequencies (f_c); (iv) drift velocity vector of the ionospheric irregularities; (v) the scintillation scattering regime, which defines irregularity spectral parameters, including the turbulence strength, the spectral indices, and the spectral break wavenumber (defined according to Table 1); (vi) the receiver trajectory and a RINEX file, which define together the satellite-receiver geometries. The simulator outputs the complex baseband scintillation signal, which is then corrupted by AWGN to achieve the desired C/N_0 level according to (2.41).

5.3 Classification performance comparison of CPSSM-generated scintillation signals using CNN and MLP

Once the viability of CNN models for scintillation classification was established using CSM-generated signals and the implementation of the CPSSM was completed, the next step involved evaluating the models with more realistic scintillation signals generated by the CPSSM-based simulator.

5.3.1 Simplified experimental setup

The first goal of the experiments using CPSSM-generated signals is to compare the performance of the standard CNN model with the MLP model, which is commonly used as a baseline model among the DNN architectures for TSC tasks (FAWAZ *et al.*, 2019, Section 3.2.1). This is done before tackling scintillation scenarios MF and MC, that is, the initial focus is on single-frequency scintillation signals generated under a simplified experimental setup.

Differently from the CSM, the present simulator accounts for MF and MC scintillation effects, as well as the impact of different monitoring station locations, satellite–receiver geometries, and local time. The simulator uses a broadcast RINEX v3.04 navigation file with MC ephemerides from February 19, 2017. The monitoring stations are spread world-wide, as shown in Table 6. These cities lie within the equatorial anomaly, where post-sunset scintillation is often observed (BALVEDI *et al.*, 2016, Figure 2). Each simulation starts at 23:00:00 UTC and lasts T_{sim} seconds. For each station, the program computes LOS satellite trajectories over the entire simulation interval.

Tabela 6 – Receiver locations used in the simulation.

Location	**Latitude**	**Longitude**	**Altitude (m)**
São José dos Campos	$-23.2198°$	$-45.8916°$	660
Fortaleza	$-3.7327°$	$-38.5270°$	21
Ascension Island	$-7.9467°$	$-14.3559°$	177
Hong Kong	$22.3193°$	$114.1694°$	479
Chiang Mai	$18.7883°$	$98.9853°$	310
Port Moresby	$-9.4790°$	$147.1494°$	35
San Antonio	$29.4252°$	$-98.4946°$	198
Pontianak	$-0.0263°$	$109.3425°$	1
Thiruvananthapuram	$8.5241°$	$76.9366°$	5
Nairobi	$-1.2921°$	$36.8219°$	1795
Abuja	$9.0563°$	$7.4985°$	360
Quito	$-0.2233°$	$-78.5141°$	2850
Iquitos	$-3.7438°$	$-73.2516°$	106

For a comparative performance between the standard CNN and MLP models, the following simplifications have been adopted: (i) only the eastward component of the drift velocity is nonzero, $v_{\text{d}} \in \{50, 75, 100, 125\}$ [m/s] (JIAO *et al.*, 2017); (ii) only GPS constellation is considered; (iii) ionospheric irregularities are fixed at an altitude of 350 km; (iv) only $N_{\text{f}} = 1$ frequency is considered (L1/E1, 1575.42 MHz); (v) a given scintillation event affects only one monitoring station with only $N_{\text{sat}} = 1$ impaired satellite; (vi) both amplitude and phase scintillation are considered. Therefore, the number of channels per example, $\mathbf{X}[k] \in \mathbb{R}^{N_{\text{sim}} \times N_{\text{c}}}$, is

$N_c = 2$, corresponding to amplitude and phase time series.

5.3.2 DNN training parameters and architectures

During the training phase of the DNN models, the following parameters were used: 20 realizations; 100 epochs for the CNN and 200 for the MLP; 1 300 instances of 5-minute duration time series; a split of 80% training and 20% test; sampling time of the scintillation signal $T = 10\,\text{ms}$; two channels ($N_c = 2$, corresponding to amplitude and phase); optimizer: ADAM; loss function: categorical cross-entropy; for the CNN, two pairs of convolutional and subsampling layers with kernel size 7, average pooling of size 7, softmax activation in the dense layer, and minibatch size 4; and for the MLP, sigmoid activation in the dense layers. The architectures and number of parameters of both models are summarized in Table 7. The MLP model comprises four dense layers with interleaved dropout layers, while the CNN model comprises two convolutional layers each followed by an average pooling layer, concluding with a FC layer.

Tabela 7 – MLP and CNN architectures description.

(a) MLP

Layer (type)	**Output Shape**	**Parameters**
Input layer	30001×2	0
Flatten layer	60002	0
Dropout layer 1	60002	0
Dense layer 1	500	30,001,500
Dropout layer 2	500	0
Dense layer 2	500	250,500
Dropout layer 3	500	0
Dense layer 3	500	250,500
Dropout layer 4	500	0
Dense layer 4	2	1,002

(b) CNN

Layer (type)	**Output Shape**	**Parameters**
Input layer	30001×2	0
Convolutional layer 1	29995×6	90
Average pooling 1	19998×6	0
Convolutional layer 2	9992×12	516
Average pooling 2	3330×12	0
Flatten layer	39960	0
Dense layer	2	79,922

5.3.3 DNN performances

Table 8 summarizes the average performance metrics for the MLP and CNN models on the test set for all realizations: The results indicate that the CNN model outperforms the

Tabela 8 – Average performance metrics of MLP and CNN models on the test set.

Model	Accuracy	Precision	Recall	F1 Score
MLP	88.81%	88.77%	89.52%	88.81%
CNN	97.84%	98.21%	97.41%	97.77%

MLP model across all metrics, achieving an accuracy of 97.84% compared to 88.81% for the MLP. Precision, recall, and F1 score are also significantly higher for the CNN, demonstrating its superior ability to classify scintillation time series accurately.

Moreover, the CNN model requires fewer epochs to converge, achieving high accuracy in just 100 epochs compared to the 200 epochs required for the MLP model. This suggests that the CNN architecture is more efficient for this classification task, likely due to its ability to learn spatial and temporal hierarchies of features from the input data. Figure 11 presents the learning curves of both models, showing the evolution of training accuracy as a function of the number of epochs for a specific realization. The curves demonstrate that the models learn the relevant features from the simulated scintillation time series, with their accuracies improving and stabilizing as the training progresses. This indicates that the chosen architectures and dataset are suitable for the classification of CPSSM-simulated ionospheric scintillation time series.

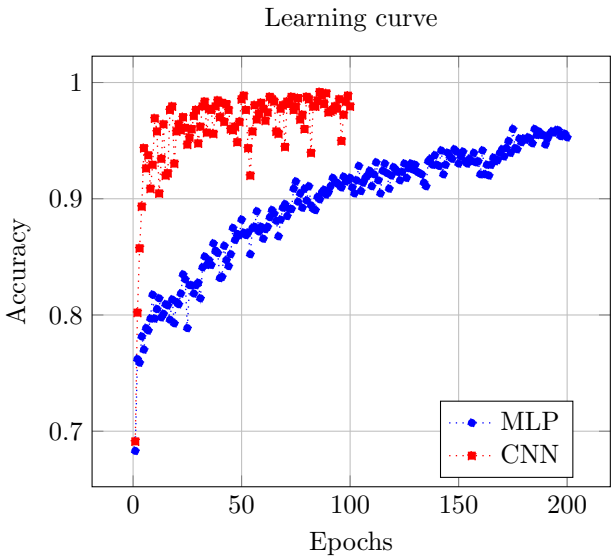

Figura 11 – Learning curve of the DNN models.

5.4 Characterizing CPSSM-generated scintillation signals via dCNN and dCAM in MF and MC scenarios

Once the superior performance of the CNN model over the MLP model has been established using a simplified experimental setup, the next step involved evaluating the CNN model in more complex MF and MC scintillation scenarios in an extended experimental setup. Additionally, the standard CNN architecture was replaced by the dCNN architecture, as described in Section 4.4. This model uses dCAM as a *post-hoc* interpretability method to identify the canonical fades in the scintillation time series that most influence the model decision-making process.

5.4.1 Extended experimental setup

The extended experimental setup modifies the methodology described in Section 5.3.1 in the following aspects:

- both GPS and Galileo constellations are considered;
- in order to observe the same equatorial scintillation event constrained to a given geographical context, the monitoring stations are changed from worldwide locations (as shown in Table 6) to 13 monitoring stations located in Brazil, as shown in Table 9;
- the frequencies L1/E1 (1575.42 MHz), L2 (1227.60 MHz), L5/E5a (1176.45 MHz), E5b (1207.14 MHz), and E6 (1278.75 MHz) are used. Therefore, $N_{\mathrm{f}} = 5$;
- a scintillation event is now defined as $N_{\mathrm{sat}} = 2$ satellites (always the same) in LOS with a given station, being simultaneously affected with the same scintillation severity for all satellite signals, lasting T_{sim} seconds, and with $v_{\mathrm{d}} \in \{25, 50, 75, 100, 125\}$ [m/s];
- it is assumed that every N_{sat} satellite transmits in all N_{f} frequencies;
- only the amplitude time series is taken into consideration. Therefore, the number of channels per example is now $N_{\mathrm{c}} = N_{\mathrm{f}} N_{\mathrm{sat}} = 10$, corresponding to the amplitude time series of each frequency and satellite of a given scintillation event;
- in the extended setup, we have introduced the concept of "scenario", which is defined by a unique combination of the following parameters: (i) scintillation event duration $T_{\mathrm{sim}} \in \{10, 30\}$ seconds; (ii) correlation length[3], $T \in \{10, 20\}$ milliseconds; (iii) $C/N_0 \in \{30, 40, 50, \infty\}$ dB-Hz, where ∞ means noiseless condition. Each combination from the

[3] Depending on the combination of T and T_{sim} a decimation is applied to the scintillation time series to keep the number of sample in $\{500, 750, 1000\}$.

16 scenarios represents a unique operating condition used to evaluate the model. These set of parameters can be understood as the hyperparameters of the monitoring station network as it is up to the network administrator to adjust them according to the application at hand. Note that the C/N_0 is left as a monitoring station hyperparameter since it is largely influenced by the receiver hardware and antenna setup, which is under control of the network administrator;

Tabela 9 – Receiver station locations used in the simulation. The monitoring station network covers different longitudes across the equatorial region in Brazil. For the geometric altitude, the WGS84 ellipsoid is considered. Geomagnetic latitude is computed for 2024 using AACGM (BURRELL, 2025, `v2`), which uses IGRF as the Earth magnetic model. Because AACGM is poorly defined near the equator, some stations lack geomagnetic latitude values.

City	Geomagnetic Latitude (°)	Latitude (°)	Longitude (°)	Altitude (m)
São José dos Campos	-20.99	−23.21	−45.89	660
Fortaleza	–	−3.73	−38.52	21
Brasília	-13.45	−15.79	−47.89	1172
Goiânia	-13.82	−16.68	−49.26	729
Belo Horizonte	-18.89	−19.91	−43.93	858
Campo Grande	-15.15	−20.46	−54.62	530
Natal	–	−5.79	−35.21	30
João Pessoa	–	−7.11	−34.86	40
Recife	-5.20	−8.04	−34.87	10
Palmas	-6.24	−10.18	−48.33	230
Cuiabá	-10.18	−15.60	−56.09	165
Belém	–	−1.45	−48.49	15
São Luís	–	−2.53	−44.28	3

5.4.2 dCNN architecture

A Python implementation of the dCNN model is available in Pacelli e Florindo (2025). The dCNN architecture is implemented using low-level instances of the PyTorch package (PASZKE *et al.*, 2019). It begins with five convolutional layers, with $N_\mathrm{w} = 128$ kernels in the first two layers and $N_\mathrm{w} = 256$ in the remaining layers. All layers use a kernel width of $K_\mathrm{w} = 3$, height of $K_\mathrm{h} = 1$, stride equals to 1, and padding equals to 0 for height and 1 for width, selected to preserve the data resolution. Each convolutional layer is followed by batch normalization and a ReLU activation function. After the final ReLU, a GAP layer is applied, followed by an affine FC layer with two output neurons that represent the weak and strong class probabilities. The predicted class is selected as the one with the higher probability. The model contains 553,346 trainable parameters. Figure 12 summarizes the complete layer sequence of the implemented

dCNN architecture. This thesis reuses the same architecture as in Boniol *et al.* (2022), which excels in other TSC tasks.

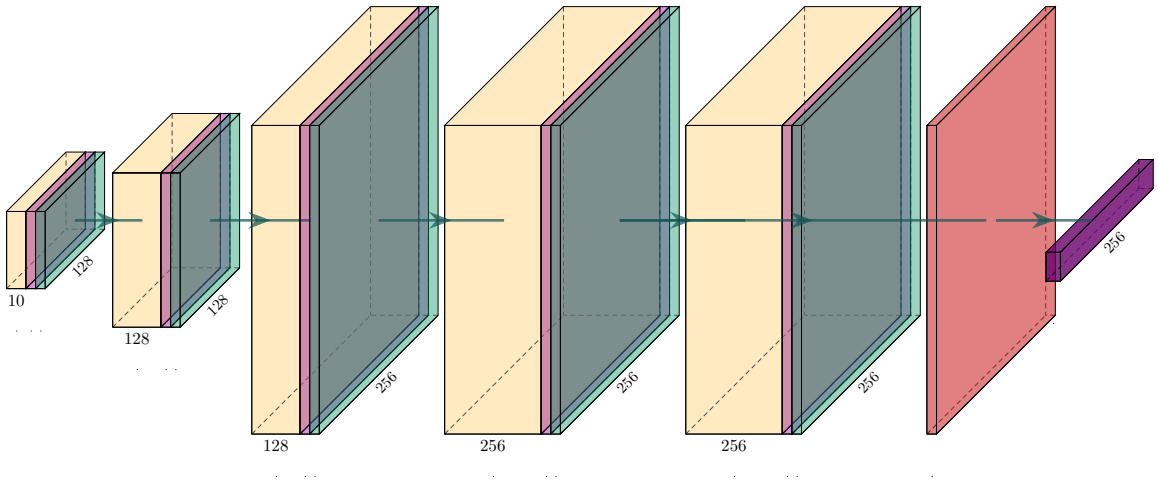

Figura 12 – The dCNN architecture (IQBAL, 2026). Each sequence of yellow, pink, and green boxes represents the convolutional, batch normalization, and ReLU layer, respectively. The width and length values correspond to the input and output channel sizes of each layer, respectively. At the same time, the image dimensions are not represented here as they remain constant throughout the network. The red box indicates the GAP layer, which produces a scalar feature map for each input channel. The final purple box represents the FC layer that takes the 256 feature maps and produces logits for the two classes.

5.4.3 Training and Validation methodology

Due to the variability of 13 monitoring station locations (*vide* Table 9), 2 scattering regimes (*vide* Table 1), and 5 drift velocities (25, 50, 75, 100, and 125 m/s) a total of $13 \times 2 \times 5 = 130$ examples are generated per scenario. Each scenario is repeated for 40 independent runs, resulting in a total of $130 \times 40 = 5200$ examples per scenario. For each run and scenario, the dataset is split into training, validation, and test sets, following an 80%/10%/10% ratio. Figure 13 illustrates the training and validation approach used in this thesis, which ensures that the model is trained on a diverse set of examples while also being validated and tested on unseen data to assess its generalization capabilities.

During training, the cross-entropy loss (BISHOP; NASRABADI, 2006, Eq. 4.108) is used as $\mathcal{L}(\cdot)$, and the synaptic weights are updated with the ADAM optimizer (KINGMA; BA, 2015) using a learning rate of $\eta_{\text{lr}} = 10^{-5}$. The model is trained for $N_{\text{e}} = 70$ epochs, with the instance order shuffled at the start of each epoch. The minibatch size is $N_{\text{b}} = 32$ during

Figura 13 – Flowchart of training, validation, and test splits for each run and scenario.

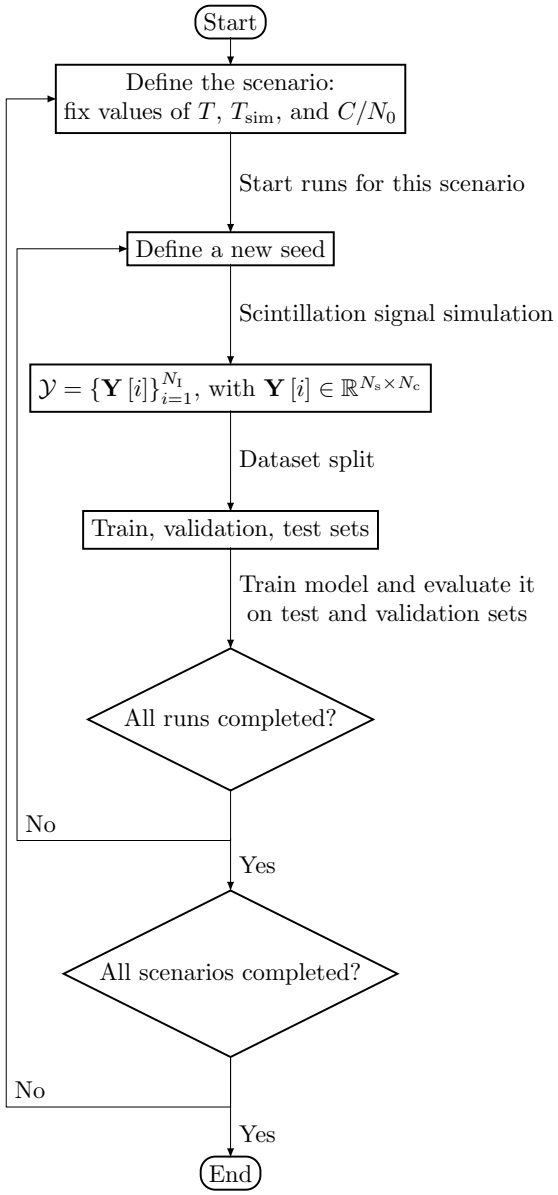

training, but it is set to one during testing so that each instance can be processed independently for detailed analysis. Model performance is evaluated separately for each scenario by varying T_{sim}, T, and C/N_0.

5.4.4 Learning Curves

Figure 14 presents the training and validation learning curves for all scenarios. In both phases, the loss begins at a high value and drops quickly, which suggests that underfitting is unlikely. The two curves remain close across epochs, indicating that the model generalizes well and that overfitting is not observed on average. Two additional trends stand out. First, three

scenarios stabilize at a higher loss level near 0.25: $C/N_0 = 30\,\text{dB}$ with $T = 20\,\text{ms}$, and $C/N_0 = 40\,\text{dB}$ or $50\,\text{dB}$ with $T = 10\,\text{ms}$, all with $T_{\text{sim}} = 10\,\text{s}$. In the remaining scenarios, the loss settles around 0.1. This finding suggests that shorter time series may make the classification task more challenging. Second, the upper edge of the shaded region, which represents the maximum loss, indicates that some runs struggle despite the high mean accuracy reported in Table 5.

Figura 14 – Learning curves for all scenarios during training and validation phases. The solid and dashed lines represent the mean training and validation losses, respectively, while the shaded areas indicate the range between the minimum and maximum losses. The training loss for the noise-free scenario is not shown to avoid clutter.

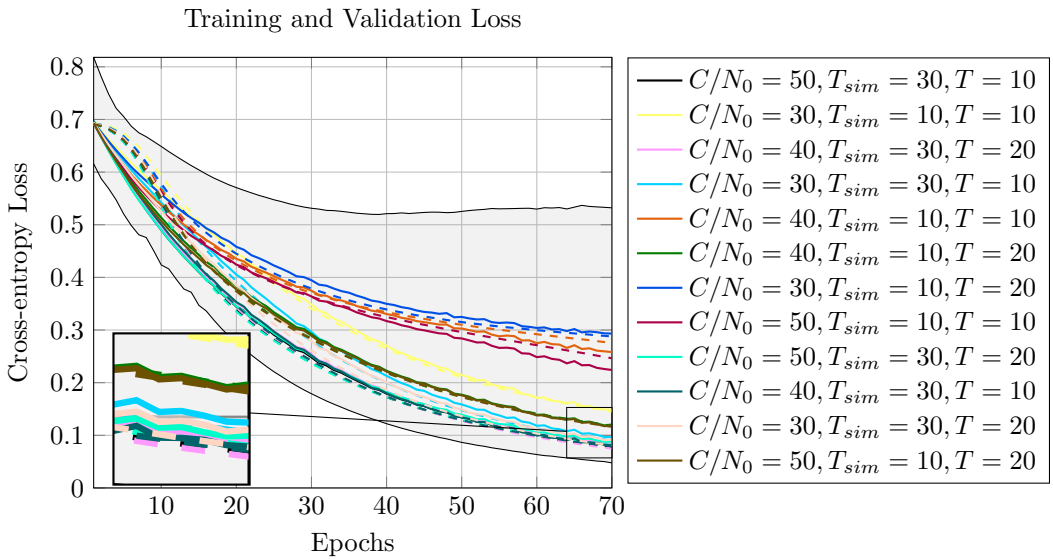

A representative example of such struggle is the 28th run of the scenario with $C/N_0 = 30\,\text{dB}$, $T_{\text{sim}} = 10\,\text{s}$, and $T = 20\,\text{ms}$. It yields the lowest accuracy in Table 5. Figure 15 shows that the model fits the training data but does not generalize well to the validation set. This behavior is a typical sign of overfitting.

Figura 15 – Learning curve for the 28th run of the scenario with $C/N_0 = 30\,\text{dB}$, $T_{\text{sim}} = 10$ s, $T = 20$ ms. Note that that validation learning curve is basically the upper bound of the shaded area in Figure 14.

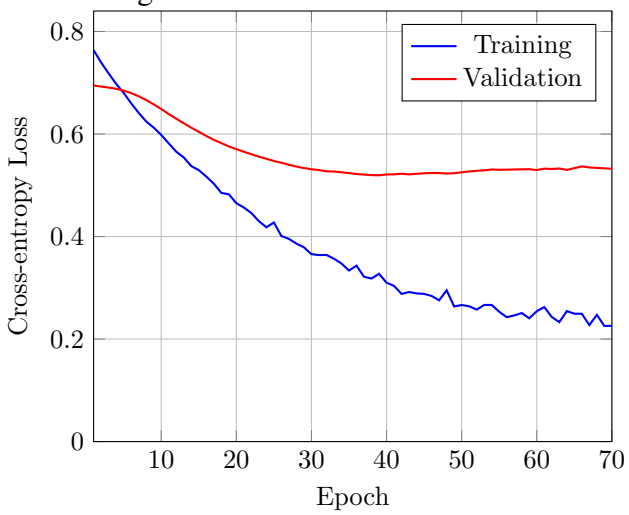

The relatively low test accuracy (about 70 %) for the experiment shown in Figure 15 results from how the scaling parameter and amplitude severity are distributed across the labels. In the CPSSM, the scaling parameter is important because it captures the propagation geometry, drift velocity, and anisotropy coefficients of the ionospheric irregularities (JIAO *et al.*, 2017, Eq. 3 *et seq.*). In practical terms, it rescales time by compressing or stretching the scintillation time series. When the scaling parameter is large, the series is stretched, and abrupt fades are smoothed even under strong scattering. From a geometric perspective, this corresponds to plasma bubbles drifting nearly in step with the IPP, thereby reducing the amplitude variation rate induced by diffractive patterns.

Figure 16 summarizes this run with scatter and violin plots of the S_4 index and the scaling parameter. Several examples labelled as strong scattering satisfy $S_4 < 0.5$, which blurs the separation between the weak and strong regimes and makes classification more difficult. The validation set, which is not seen during training, contains a higher fraction of these low-S_4 strong cases, which explains the overfitting behavior in Figure 15. The plot also reveals scaling-parameter outliers driven by propagation geometry. When the scaling parameter is high, the split does not include training examples of strong scintillation with low S_4, nor weak scintillation with high S_4, so the model tends to follow the patterns learned during training and misclassifies validation cases. In addition, exceptionally large scaling-parameter values produce heavily stretched amplitude variations, and, with the chosen T_{sim}, the resulting amplitude time series is nearly flat, which further reduces the contrast between weak and strong scintillation. This

imbalance suggests that labels based only on the phase PSD may be insufficient for certain, likely rare, propagation geometries.

Figura 16 – Scatter plot of the scaling parameter versus the S_4 index for the 28th run of the scenario with $\mathrm{C/N_0} = 30\,\mathrm{dB}$, $T_{\mathrm{sim}} = 10$ s, $T = 20$ ms. A kernel density estimator is used to generate the PDF of the scaling parameter and of S_4, shown at the bottom and left of the scatter plot, respectively.

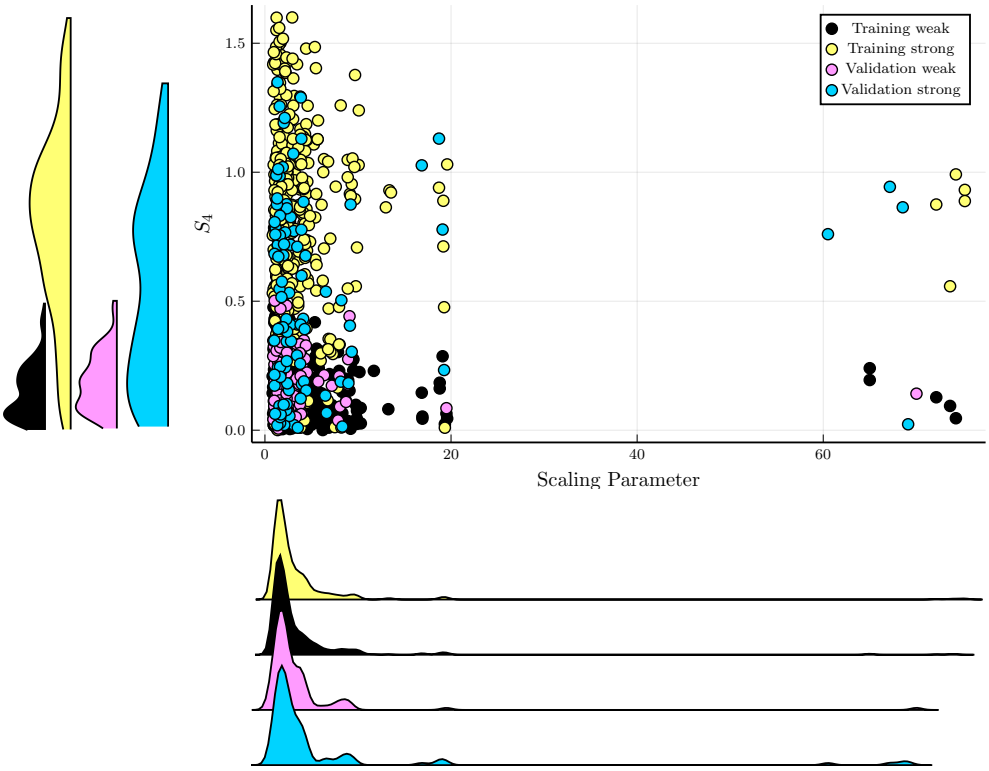

5.4.5 Test accuracy

Although severity labeling is not the primary objective of the present Thesis, we report the accuracy of the test set because meaningful dCAM maps depend on strong classification performance (BONIOL *et al.*, 2022, Section 4.4). Table 5 summarizes the mean accuracy and its standard deviation across 40 runs for each scenario. The proposed dCNN achieves a mean accuracy above 89% in every scenario. The low standard deviations indicate that performance is consistent across runs.

Table 5 shows lower accuracy for the 10 s series, whereas 30 s series remain robust across correlation times, C/N_0 levels, and drift velocities. Reducing T from 20 ms to 10 ms mainly affects 10 s series at low C/N_0, suggesting that short correlation times obscure features when data are brief.

Using $N_{\mathrm{f}} = 5$ frequencies and $N_{\mathrm{sat}} = 2$ satellites yields a test accuracy above 90%

Tabela 10 – Classification accuracy results for all scenarios. The results are reported as the mean and standard deviation of the accuracy over 40 independent runs for each scenario. The row highlighted in bold indicates the scenario with the lowest mean accuracy, which is further analyzed in this subsection.

T_{sim} [s]	T [ms]	C/N_0 [dB-Hz]	Mean accuracy	Standard deviation
10	10	30	0.973	0.037
10	10	40	0.895	0.077
10	10	50	0.910	0.073
10	10	∞	0.912	0.070
10	**20**	**30**	**0.895**	**0.079**
10	20	40	0.983	0.029
10	20	50	0.984	0.029
10	20	∞	0.984	0.029
30	10	30	0.995	0.015
30	10	40	0.994	0.020
30	10	50	0.995	0.015
30	10	∞	0.912	0.070
30	20	30	1.000	0.000
30	20	40	1.000	0.000
30	20	50	0.996	0.013
30	20	∞	1.000	0.000

even at $C/N_0 = 30$ dB-Hz, highlighting the value of MF and multisatellite diversity.

5.4.5.1 dCAM Analysis

In this section, the dCNN decision is interpreted with dCAM heatmaps computed on the test set. Figure 17 depicts a correctly classified strong scattering event that exhibits strong fades across all frequencies.

Figura 17 – dCAM heatmaps of the class activation maps for all frequencies in a single satellite-receiver link. The receiver is located in Campo Grande, with $v_d = 100\,\mathrm{m/s}$, $T_{sim} = 30\,\mathrm{s}$, $T = 10\,\mathrm{ms}$, and C/N_0 set to ∞. From top to bottom, each row corresponds to one frequency band (L1/E1, E6, L2, E5b, and L5/E5a). The left and right columns show the intensity (squared amplitude in dB) and the phase, respectively. During testing, only the time series in the left column is provided to the model. The dCAM output is overlaid on the intensity panel and mirrored onto the phase panel. The color bar encodes the relevance score, with warmer colors indicating higher relevance. Phase unwrapping uses the Fourier-interpolation algorithm proposed by Rino *et al.* (2020). For this example, the dCNN achieves an accuracy of 98 %.

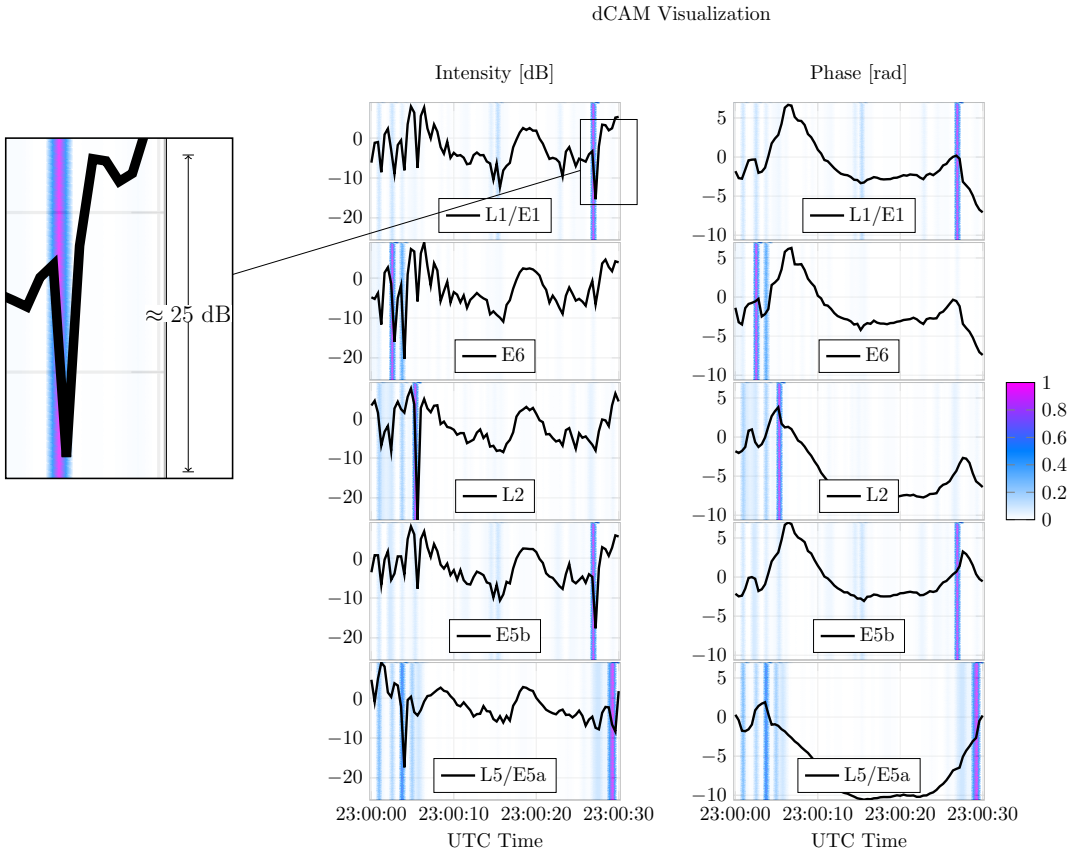

The dCAM indicates *where* in the amplitude time series the dCNN concentrates its attention when classifying the scintillation regime. In other words, it assigns higher relevance to the samples that drive the model toward a strong scattering decision. When interpreting the heatmap, the event is classified as strong scattering overall, but the highlighted regions correspond to features that best match the strong-scattering patterns learned during training.

Canonical fades are characterized by abrupt power losses that occur alongside a near half-cycle phase shift. Figure 17 shows that the strongest activation typically aligns with deep fades and the associated phase fluctuations, which are characteristic of canonical fades (HUMPHREYS *et al.*, 2010b). Since canonical fades account for 90 % of the loss-of-lock events observed in field tests (HUMPHREYS *et al.*, 2010a), these results suggest that dCAM, as a

post-hoc method, can effectively identify *where* canonical fades occur in the time series. This result is the main contribution of the present Thesis.

6 CONCLUSIONS AND FUTURE WORK

This thesis has presented a novel approach for characterizing ionospheric scintillation time series using CNN models. Instead of relying on traditional scintillation indices, S_4 and σ_ϕ, which often fail to capture the complex patterns present in scintillation data, the proposed method leverages the feature extraction capabilities of CNN architectures to classify scintillation regimes directly from the estimated scintillation time series.

The data used in the analysis was computer-generated, and the motivation for that stems from limitations in the state of the practice in scintillation monitoring via GNSS. Real scintillation time series are often not available due to storage constraints. Instead, only high-level scintillation statistics (*e.g.*, S_4 index) are usually stored for long-term monitoring. Even when they are available, only the raw postcorrelated amplitude time series are stored, which contain several other sources of disturbances (*e.g.*, multipath, receiver noise, etc.), in addition to the LOS dynamics. In contrast, the present thesis assumes the scintillation time series properly estimated, which is already possible in the SOTA but is not the reality for most deployed and operational scintillation monitoring receivers and their publicly available datasets.

For this reason, synthetic scintillation data were generated using two well-established scintillation models. First, the CSM was used to create a simplified three-class data set for initial experiments, where only the diffractive patterns are taken into account and the model makes no distinction among frequencies. In this scenario where the statistical model is used, the standard CNN architecture achieved a mean accuracy of 91 % in noiseless conditions, and 81 % when the AWGN variance equals 50 % of the scintillation variance.

Subsequently, Pacelli e Florindo (2025, `v2.1`) have refactored previous MATLAB and C implementations of the CPSSM to generate scintillation datasets in MF and MC configurations. Then, this simulator was used to build a more realistic two-class data set that includes both diffractive and refractive patterns, together with frequency-dependent effects. In an TSC experiment limited to the L1/E1 signal and using both amplitude and phase time series, the standard CNN outperformed an MLP baseline and achieved a mean accuracy of 97 %.

Finally, the standard CNN is replaced by the dCNN, which was designed for the MF and multi-satellite classification task, and its performance was evaluated across a broad range of scenarios. This model, proposed by Boniol *et al.* (2022), achieved mean test accuracy above 89 % in all evaluated conditions, and the low variability across independent runs indicates consistent performance. The results also show that multi-satellite and MF diversity improves

robustness. For instance, with $N_{\mathrm{f}} = 5$ and $N_{\mathrm{sat}} = 2$, test accuracy remains above 90 % even at $C/N_0 = 30\,\mathrm{dB}$.

The main contribution of this thesis is the identification of the canonical fades, responsible for more than 90 % of cycle slips observed in the tracking loop performance of traditional GNSS receivers. Discriminative features are extracted from estimates of the scintillation time series, making dCNN achieve high accuracy when the two-class CPSSM-based dataset is used. The dCAM was used as a *post-hoc* explainability tool to interpret the dCNN decisions highlight the canonical fades. The core strategy used in the present thesis is: instead of generating a scintillation dataset comprised of a wide severity range, the dCNN is trained with two extreme cases so that the dCAM can identify the deep fades and abrupt phase changes that characterize canonical fades as the most salient features for the classification task. As a result, the dCAM produced heatmaps that spotlight these events in the scintillation time series for every channel used as input to the dCNN. This interpretability analysis supports that the dCNN relies on physically meaningful features and that dCAM can identify *where* these events occur in the time series. Overall, the combination of high classification accuracy of dCNN and dCAM-based explanations provides a practical framework for both automated regime classification and *post-hoc* analysis of scintillation events.

This thesis opens several avenues for the research groups of ITA (*Instituto Tecnológico de Aeronáutica*), UFC (*Universidade Federal do Ceará*) and UPC (*Universitat Politècnica de Catalunya*). The fist and utmost priority is to implement a SDR for the monitoring of equatorial ionospheric scintillation activity. The main goal is to collect the empirical scintillation data which is assumed in this thesis, so that the proposed dCNN-based classification framework can be validated with real-world measurements. Different from the current approach for obtaining actual data, with scintillation signal thus collected should be free from the receiver-induced processing artifacts that are generated by the classical tracking loop architectures used in ISMRs. On the one hand, the development of a SDR for scintillation monitoring comprises a wide range of foundations that are beyond the scope of this thesis. However, the challenges imposed by the implementation of such a system, such as the estimation of the scintillation time series from GNSS signal, were already proposed and validated in the literature, proving a viable approach. On the other hand, the present thesis fills the last theoretical gap in this goal, which is having a robust algorithm to identify and classify scintillation regimes from the estimated scintillation time series. This makes the development of the SDR merely a matter of engineering effort. Once

completed, the SDR will be deployed in two locations in Brazil: São José dos Campos (23.2°S, 45.9°W) and Fortaleza (3.7°S, 38.5°W).

While the development of the SDR should be conducted by the author of the present thesis during the post-doctoral stage, some future works from theoretical perspective could be pursued in parallel:

1. **Cycle-slip analysis under CPSSM scintillation in classical CLT loops**: while the characterization work presented in this thesis identified the canonical fades as the main features responsible for cycle slips, a thorough analysis of the cycle-slip occurrence in CLT loops under CPSSM-based scintillation is still missing. Such analysis would provide a more solid ground for the importance of canonical fades in practical scenarios, and would also help to design better training datasets for the dCNN model. For that, the scintillation-corrupted GNSS signals should be generated in computer simulation and used as input to a DLL, PLL and/or FLL. The cycle-slip events should be logged and correlated with the highlights produced by the dCAM in order to verify if the canonical fades are indeed the main triggers of cycle slips;
2. **Geometry-aided Bayesian-based tracking loop estimation for scintillation monitoring**: While the literature presented several works based on KF for robust carrier tracking under scintillation, none of them explores this approach under the monitoring station perspective. As a consequence, they naturally assume unknown satellite-receiver geometry and strive to maintain lock under strong scintillation and LOS dynamics. However, for monitoring purposes, the receiver position is fixed and known, and the satellite ephemeris can be used as long as that offline processing is admitted. This prior knowledge can be used to design a geometry-aided Bayesian estimator that can leverage this information to improve the carrier and code tracking performance under scintillation. This approach should be compared with the SOTA Bayesian estimators for scintillation tracking in order to evaluate its performance gain;
3. **Computational-efficient alternatives to the dCNN**: while the model proposed by Boniol *et al.* (2022) is capable of spotlighting the canonical fades in the scintillation time series, its computational complexity grows factorially with the number of input channels. This makes its deployment in real-time applications challenging, especially when multiple frequencies and satellites are used as input. Therefore, exploring computational-efficient alternatives to the dCNN that can still provide interpretability features is an important

future work. Possible alternatives include lightweight CNN architectures or tensor decomposition techniques, which can reduce the model size and inference time while maintaining satisfactory performance;

REFERENCES

AARONS, J. Global morphology of ionospheric scintillations. **Proceedings of the IEEE**, IEEE, v. 70, n. 4, p. 360–378, 1982. ISSN 0018-9219.

ABDU, MA. Outstanding problems in the equatorial ionosphere–thermosphere electrodynamics relevant to spread F. **Journal of Atmospheric and Solar-Terrestrial Physics**, Elsevier, v. 63, n. 9, p. 869–884, 2001. ISSN 1364-6826.

ABDU, MA.; BITTENCOURT, JA.; BATISTA, IS. Magnetic declination control of the equatorial F region dynamo electric field development and spread F. **Journal of Geophysical Research: Space Physics**, Wiley Online Library, v. 86, n. A13, p. 11443–11446, 1981. ISSN 0148-0227.

BAGNALL, A.; JANACEK, G. A Run Length Transformation for Discriminating Between Auto Regressive Time Series. **Journal of Classification**, v. 31, n. 2, p. 154–178, jul. 2014. ISSN 0176-4268, 1432-1343.

BAGNALL, A.; LINES, J.; BOSTROM, A.; LARGE, J.; KEOGH, E. The great time series classification bake off: A review and experimental evaluation of recent algorithmic advances. **Data Mining and Knowledge Discovery**, v. 31, n. 3, p. 606–660, maio 2017. ISSN 1573-756X.

BAHL, L. R.; BROWN, P. F.; de Souza, P. V.; MERCER, R. L. Speech recognition with continuous-parameter hidden Markov models. **Computer Speech & Language**, Elsevier, v. 2, n. 3-4, p. 219–234, 1987.

BALLARD, G.; KOLDA, T. G. **Tensor Decompositions for Data Science**. Cambridge, United Kingdom: Cambridge University Press, 2025. ISBN 978-1-009-47165-7.

BALVEDI, G. C.; HARRIS, M.; FREGNANI, J. A. G.; SAOTOME, O. Operational Mitigation Practice to Enable the Use of GBAS on Areas Influenced by Harsh Ionosphere Phenomena. 2016.

BARREAU, V.; VIGNEAU, W.; MACABIAU, C.; DEAMBROGIO, L. Kalman Filter based robust GNSS signal tracking algorithm in presence of ionospheric scintillations. In: **2012 6th ESA Workshop on Satellite Navigation Technologies (Navitec 2012) & European Workshop on GNSS Signals and Signal Processing**. [S.l.: s.n.], 2012. p. 1–8. ISSN 2325-5455.

BASU, S.; MACKENZIE, EM.; COSTA, E.; FOUGERE, PF.; CARLSON, HC.; WHITNEY, HE. 250 MHz/GHz scintillation parameters in the equatorial, polar, and auroral environments. **IEEE journal on selected areas in communications**, IEEE, v. 5, n. 2, p. 102–115, 1987. ISSN 0733-8716.

BEACH, T. L. Perils of the GPS phase scintillation index (sigma phi). **Radio Science**, v. 41, n. 5, 2006. ISSN 1944-799X.

BÉNIGUEL, Y. **GISM User Manual**. [S.l.], 2011. 33 p.

BETZ, J. W. **Engineering Satellite-Based Navigation and Timing: Global Navigation Satellite Systems, Signals, and Receivers**. 1st edition. ed. Hoboken, New Jersey: Wiley-IEEE Press, 2015. ISBN 978-1-118-61597-3.

BISHOP, C. M.; NASRABADI, N. M. **Pattern Recognition and Machine Learning**. New York, USA: Springer, 2006. v. 4. ISBN 978-0-387-31073-2.

BONIOL, P.; MEFTAH, M.; REMY, E.; PALPANAS, T. dCAM: Dimension-wise Class Activation Map for Explaining Multivariate Data Series Classification. In: **Proceedings of the 2022 International Conference on Management of Data**. Philadelphia PA USA: ACM, 2022. p. 1175–1189. ISBN 978-1-4503-9249-5.

BOOKER, H. G.; RATCLIFFE, J. A.; SHINN, D. H. Diffraction from an irregular screen with applications to ionospheric problems. **Philosophical Transactions of the Royal Society of London. Series A, Mathematical and Physical Sciences**, The Royal Society London, v. 242, n. 856, p. 579–607, 1950.

BOOKER, H. G.; WELLS, H. W. Scattering of radio waves by the F-region of the ionosphere. **Terrestrial Magnetism and Atmospheric Electricity**, v. 43, n. 3, p. 249–256, set. 1938. ISSN 0096-8013, 0096-8013.

BORRE, K.; FERNÁNDEZ-HERNÁNDEZ, I.; LÓPEZ-SALCEDO, J. A.; BHUIYAN, M. Z. H. (Ed.). **GNSS Software Receivers**. Cambridge: Cambridge University Press, 2022. ISBN 978-1-108-83701-9.

BRIGGS, B. H.; PARKIN, I. A. On the variation of radio star and satellite scintillations with zenith angle. **Journal of Atmospheric and Terrestrial Physics**, v. 25, n. 6, p. 339–366, jun. 1963. ISSN 0021-9169.

BURRELL, A. **Aburrell/Aacgmv2**. 2025.

CARRANO, C. **Ispectrum**. 2016. Https://github.com/ita-gnss-lab/gnss-scintillation-simulator/blob/refactored/libs/plots/Ispectrum/ispectrum-v1.1/ispectrum.c.

CARRANO, C. S.; RINO, C. L. A theory of scintillation for two-component power law irregularity spectra: Overview and numerical results. **Radio Science**, v. 51, n. 6, p. 789–813, 2016. ISSN 1944-799X.

CARRANO, C. S.; RINO, C. L.; GROVES, K. M. Maximum likelihood estimation of phase screen parameters from ionospheric scintillation spectra. In: **15th International Ionospheric Effects Symposium**. [S.l.]: Radio Science Publications Alexandria, 2017. p. 1–11.

CARRANO, C. S.; VALLADARES, C. E.; GROVES, K. M. Latitudinal and Local Time Variation of Ionospheric Turbulence Parameters during the Conjugate Point Equatorial Experiment in Brazil. **International Journal of Geophysics**, v. 2012, n. 1, p. 103963, 2012. ISSN 1687-8868.

CHEN, H.; TANG, F.; TINO, P.; YAO, X. Model-based kernel for efficient time series analysis. In: **Proceedings of the 19th ACM SIGKDD International Conference on Knowledge Discovery and Data Mining**. Chicago Illinois USA: ACM, 2013. p. 392–400. ISBN 978-1-4503-2174-7.

CHENG, D. **Field and Wave Electromagnetics**. 2nd edition. ed. Edinburgh: Pearson, 2013. ISBN 978-1-292-02656-5.

CHYTIL, B. The distribution of amplitude scintillation and the conversion of scintillation indices. **Journal of Atmospheric and Terrestrial Physics**, v. 29, n. 9, p. 1175–1177, set. 1967. ISSN 0021-9169.

CRANE, R. Ionospheric scintillation. **Proceedings of the IEEE**, v. 65, n. 2, p. 180–199, fev. 1977. ISSN 1558-2256.

CURRAN, J. T.; BAVARO, M.; MORRISON, A.; FORTUNY, J. Developing an Ionospheric Scintillation Monitoring Receiver. out. 2014.

DAVIES, K. **Ionospheric Radio**. [S.l.]: IET, 1990.

DIERENDONCK, A. J. V. How GPS receivers measure (or should measure) ionospheric scintillation and TEC and how GPS receivers are affected by the ionosphere. In: **Proc. 11th International Ionospheric Effects Symposium**. [S.l.: s.n.], 2005.

DIERENDONCK, A. J. V.; ARBESSER-RASTBURG, B. Measuring Ionospheric Scintillation in the Equatorial Region Over Africa, Including Measurements From SBAS Geostationary Satellite Signals. In: **Proceedings of the 17th International Technical Meeting of the Satellite Division of The Institute of Navigation (ION GNSS 2004)**. [S.l.: s.n.], 2004. p. 316–324.

DIERENDONCK, AJ. V.; KLOBUCHAR, J.; HUA, Q. Ionospheric scintillation monitoring using commercial single frequency C/A code receivers. In: **Proceedings of ION GPS**. [S.l.: s.n.], 1993. v. 93, p. 1333–1342.

DUNGEY, J. W. Convective diffusion in the equatorial F region. **Journal of Atmospheric and Terrestrial Physics**, Elsevier, v. 9, n. 5-6, p. 304–310, 1956.

EGEA-ROCA, D.; ARIZABALETA-DIEZ, M.; PANY, T.; ANTREICH, F.; LÓPEZ-SALCEDO, J. A.; PAONNI, M.; SECO-GRANADOS, G. GNSS User Technology: State-of-the-Art and Future Trends. **IEEE Access**, IEEE, v. 10, p. 39939–39968, 2022. ISSN 2169-3536.

FAUVEL, K.; LIN, T.; MASSON, V.; FROMONT, É.; TERMIER, A. XCM: An Explainable Convolutional Neural Network for Multivariate Time Series Classification. **Mathematics**, Multidisciplinary Digital Publishing Institute, v. 9, n. 23, p. 3137, jan. 2021. ISSN 2227-7390.

FAWAZ, H. I.; FORESTIER, G.; WEBER, J.; IDOUMGHAR, L.; MULLER, P.-A. Deep learning for time series classification: A review. **Data mining and knowledge discovery**, Springer, v. 33, n. 4, p. 917–963, 2019.

FELTENS, J. **IONMON Maps**. 2026. Disponível em: <https://swe.ssa.esa.int/ionmon>.

FLORINDO, R. d. L.; ANTREICH, F. Multi-Frequency Kalman Filter Carrier Phase Tracking for Ionospheric Scintillation Mitigation and Monitoring. In: **Proceedings of the 37th International Technical Meeting of the Satellite Division of The Institute of Navigation (ION GNSS+ 2024)**. [S.l.: s.n.], 2024. p. 3611–3625. ISSN 2331-5954.

FLORINDO, R. d. L.; PACELLI, R.; FERREIRA, T. L.; SILVA, D. O.; de Lucena, A. M. P.; ANTREICH, F. Advanced Kalman Filter Carrier Tracking: Performance Assessment Under Two Ionospheric Scintillation Models. In: **Proceedings of the 38th International Technical Meeting of the Satellite Division of The Institute of Navigation (ION GNSS+ 2025)**. [S.l.: s.n.], 2025. p. 3421–3435. ISSN 2331-5954.

FOHLMEISTER, F. **GNSS Carrier Phase Tracking under Ionospheric Scintillations**. Tese (Thesis) — Technische Universität München, abr. 2021.

FOHLMEISTER, F.; ANTREICH, F.; NOSSEK, J. A. Dual Kalman filtering based GNSS phase tracking for scintillation mitigation. In: **2018 IEEE/ION Position, Location and Navigation Symposium (PLANS)**. [S.l.: s.n.], 2018. p. 1151–1158. ISSN 2153-3598.

FORTE, B.; RADICELLA, S. M. Problems in data treatment for ionospheric scintillation measurements. **Radio Science**, v. 37, n. 6, p. 8–1–8–5, 2002. ISSN 1944-799X.

FREMOUW, E. J.; LEADABRAND, R. L.; LIVINGSTON, R. C.; COUSINS, M. D.; RINO, C. L.; FAIR, B. C.; LONG, R. A. Early results from the DNA Wideband satellite experiment—Complex-signal scintillation. **Radio Science**, v. 13, n. 1, p. 167–187, 1978. ISSN 1944-799X.

FREMOUW, E. J.; LIVINGSTON, R. C.; MILLER, D. A. On the statistics of scintillating signals. **Journal of Atmospheric and Terrestrial Physics**, v. 42, n. 8, p. 717–731, ago. 1980. ISSN 0021-9169.

FU, W.; HAN, S.; RIZOS, C.; KNIGHT, M.; FINN, A. Real-time ionospheric scintillation monitoring. In: **Proceedings of the 12th International Technical Meeting of the Satellite Division of The Institute of Navigation (ION GPS 1999)**. [S.l.: s.n.], 1999. p. 1461–1472.

GOODFELLOW, I.; BENGIO, Y.; COURVILLE, A. **Deep Learning**. Illustrated edição. Cambridge, Massachusetts: The MIT Press, 2016. ISBN 978-0-262-03561-3.

GREEN, E. I. The story of Q. **American Scientist**, JSTOR, v. 43, n. 4, p. 584–594, 1955.

HAYKIN, S. **Neural Networks and Learning Machines, 3/E**. [S.l.]: Pearson Education India, 2009. ISBN 93-325-8625-X.

HAYKIN, S.; MOHER, M. **An Introduction to Analog and Digital Communications**. 2th. ed. Hoboken, NJ: Wiley, 2006. ISBN 978-0-471-43222-7.

HAYKIN, S.; VEEN, B. V. **Signals and Systems**. [S.l.]: Wiley, 1998. ISBN 978-0-471-13820-4.

HEWISH, A. The diffraction of radio waves in passing through a phase-changing ionosphere. **Proceedings of the Royal Society of London. Series A. Mathematical and Physical Sciences**, The Royal Society London, v. 209, n. 1096, p. 81–96, 1951.

HOFMANN-WELLENHOF, B.; LICHTENEGGER, H.; COLLINS, J. **Global Positioning System: Theory and Practice**. [S.l.]: Springer Science & Business Media, 2012.

HOFMANN-WELLENHOF, B.; LICHTENEGGER, H.; WASLE, E. **GNSS – Global Navigation Satellite Systems: GPS, GLONASS, Galileo, and More**. Vienna: Springer, 2008. ISBN 978-3-211-73012-6.

HUMPHREYS, T. E.; PSIAKI, M. L.; HINKS, J. C.; O'HANLON, B.; KINTNER, P. M. Simulating Ionosphere-Induced Scintillation for Testing GPS Receiver Phase Tracking Loops. **IEEE Journal of Selected Topics in Signal Processing**, v. 3, n. 4, p. 707–715, ago. 2009. ISSN 1941-0484.

HUMPHREYS, T. E.; PSIAKI, M. L.; KINTNER, P. M. Modeling the Effects of Ionospheric Scintillation on GPS Carrier Phase Tracking. **IEEE Transactions on Aerospace and Electronic Systems**, v. 46, n. 4, p. 1624–1637, out. 2010. ISSN 1557-9603.

HUMPHREYS, T. E.; PSIAKI, M. L.; LEDVINA, B. M.; CERRUTI, A. P.; KINTNER, P. M. Data-driven testbed for evaluating GPS carrier tracking loops in ionospheric scintillation. **IEEE Transactions on Aerospace and Electronic Systems**, IEEE, v. 46, n. 4, p. 1609–1623, 2010. ISSN 0018-9251.

INGLE, V. K.; PROAKIS, J. G. **Digital Signal Processing Using MATLAB**. [S.l.]: Cole Publishing Company, 2000.

IOFFE, S.; SZEGEDY, C. Batch Normalization: Accelerating Deep Network Training by Reducing Internal Covariate Shift. In: **Proceedings of the 32nd International Conference on Machine Learning**. [S.l.]: PMLR, 2015. p. 448–456. ISSN 1938-7228.

IQBAL, H. **HarisIqbal88/PlotNeuralNet**. 2026.

ISMAIL, A. A.; GUNADY, M.; BRAVO, H. C.; FEIZI, S. Benchmarking deep learning interpretability in time series predictions. **Advances in neural information processing systems**, v. 33, p. 6441–6452, 2020.

ITU-R, S. G. . **Transionospheric Radio Propagation. The Global Ionospheric Scintillation Model (GISM)**. [S.l.], 2007.

JIAO, Y. **Low-Latitude Ionospheric Scintillation Signal Simulation, Characterization, and Detection on GPS Signals**. Tese (Thesis) — Colorado State University, 2017.

JIAO, Y.; HALL, J. J.; MORTON, Y. T. Automatic equatorial GPS amplitude scintillation detection using a machine learning algorithm. **IEEE Transactions on Aerospace and Electronic Systems**, v. 53, n. 1, p. 405–418, 2017. ISSN 0018-9251.

JIAO, Y.; HALL, J. J.; MORTON, Y. T. Performance Evaluation of an Automatic GPS Ionospheric Phase Scintillation Detector Using a Machine-Learning Algorithm. **NAVIGATION**, v. 64, n. 3, p. 391–402, 2017. ISSN 2161-4296.

JIAO, Y.; MORTON, Y. T. Comparison of the effect of high-latitude and equatorial ionospheric scintillation on GPS signals during the maximum of solar cycle 24. **Radio Science**, AGU, v. 50, n. 9, p. 886–903, 2015. ISSN 1944-799X.

JIAO, Y.; MORTON, Y. T.; TAYLOR, S.; PELGRUM, W. Characterization of high-latitude ionospheric scintillation of GPS signals. **Radio Science**, AGU, v. 48, n. 6, p. 698–708, 2013. ISSN 1944-799X.

JIAO, Y.; RINO, C.; MORTON, Y. J.; CARRANO, C. Scintillation Simulation on Equatorial GPS Signals for Dynamic Platforms. In: **Proceedings of the 30th International Technical Meeting of the Satellite Division of The Institute of Navigation (ION GNSS+ 2017)**. [S.l.: s.n.], 2017. p. 1644–1657. ISSN 2331-5954.

JIAO, Y.; XU, D.; MORTON, Y.; RINO, C. Equatorial Scintillation Amplitude Fading Characteristics Across the GPS Frequency Bands. **NAVIGATION**, v. 63, n. 3, p. 267–281, 2016. ISSN 2161-4296.

JIAO, Y.; XU, D.; RINO, C. L.; MORTON, Y. T.; CARRANO, C. S. A Multifrequency GPS Signal Strong Equatorial Ionospheric Scintillation Simulator: Algorithm, Performance, and Characterization. **IEEE Transactions on Aerospace and Electronic Systems**, v. 54, n. 4, p. 1947–1965, ago. 2018. ISSN 1557-9603.

KAPLAN, E. D.; HEGARTY, C. **Understanding GPS/GNSS: Principles and Applications**. [S.l.]: Artech house, 2017.

KAY, S. M. **Fundamentals of Statistical Processing, Volume 2: Detection Theory**. [S.l.]: Pearson Education India, 2009.

KELLEY, MC. Equatorial spread-F: Recent results and outstanding problems. **Journal of atmospheric and terrestrial physics**, Elsevier, v. 47, n. 8-10, p. 745–752, 1985. ISSN 0021-9169.

KINGMA, D. P.; BA, J. Adam: A Method for Stochastic Optimization. In: BENGIO, Y.; LECUN, Y. (Ed.). **3rd International Conference on Learning Representations, ICLR 2015, San Diego, CA, USA, May 7-9, 2015, Conference Track Proceedings**. [S.l.: s.n.], 2015.

KINTNER, P. M.; HUMPHREYS, T.; HINKS, J. GNSS and ionospheric scintillation. **Inside GNSS**, v. 4, n. 4, p. 22–30, 2009.

KINTNER, P. M.; KIL, H.; BEACH, T. L.; de Paula, E. R. Fading timescales associated with GPS signals and potential consequences. **Radio Science**, v. 36, n. 4, p. 731–743, 2001. ISSN 1944-799X.

KINTNER, P. M.; LEDVINA, B. M.; de Paula, E. R.; KANTOR, I. J. Size, shape, orientation, speed, and duration of GPS equatorial anomaly scintillations. **Radio Science**, v. 39, n. 2, 2004. ISSN 1944-799X.

KINTNER, P. M.; LEDVINA, B. M.; PAULA, E. R. D. GPS and ionospheric scintillations. **Space Weather**, v. 5, n. 9, p. 2006SW000260, set. 2007. ISSN 1542-7390, 1542-7390.

KNIGHT, M. F. **Ionospheric Scintillation Effects on Global Positioning System Receivers**. Tese (Thesis) — University of Adelaide, 2000.

KNIGHT, M. F.; FINN, A.; CERVERA, M. **Ionospheric Effects on Global Positioning System Receivers**. [S.l.], 1998.

KOLDA, T. G.; BADER, B. W. Tensor Decompositions and Applications. **SIAM Review**, Society for Industrial and Applied Mathematics, v. 51, n. 3, p. 455–500, ago. 2009. ISSN 0036-1445.

KULLSTAM, P.; KESKINEN, M. Ionospheric scintillation effects on UHF satellite communications. In: **MILCOM 2000 Proceedings. 21st Century Military Communications. Architectures and Technologies for Information Superiority (Cat. No.00CH37155)**. [S.l.: s.n.], 2000. v. 2, p. 779–783 vol.2.

LÄNGKVIST, M.; KARLSSON, L.; LOUTFI, A. A review of unsupervised feature learning and deep learning for time-series modeling. **Pattern recognition letters**, Elsevier, v. 42, p. 11–24, 2014.

LATHI, B. P. **Modern Digital and Analog Communications Systems**. 4th. ed. New York Oxford: Oxford University Press, USA, 2010. ISBN 978-0-19-538493-2.

LINTY, N.; FARASIN, A.; FAVENZA, A.; DOVIS, F. Detection of GNSS ionospheric scintillations based on machine learning decision tree. **IEEE Transactions on Aerospace and Electronic Systems**, v. 55, n. 1, p. 303–317, 2018. ISSN 0018-9251.

LIU, Y.; MORTON, Y. J.; JIAO, Y. Application of machine learning to the characterization of GPS L1 ionospheric amplitude scintillation. In: **2018 IEEE/ION Position, Location and Navigation Symposium (PLANS)**. [S.l.]: IEEE, 2018. p. 1159–1166. ISBN 1-5386-1647-5.

LOCUBICHE-SERRA, S.; SECO-GRANADOS, G.; LÓPEZ-SALCEDO, J. A. Doubly-adaptive autoregressive Kalman filter for GNSS carrier tracking under scintillation conditions. In: . [S.l.: s.n.], 2016. p. 1–6.

LOCUBICHE-SERRA, S.; SECO-GRANADOS, G.; LÓPEZ-SALCEDO, J. A. Performance assessment of a low-complexity autoregressive Kalman filter for GNSS carrier tracking using real scintillation time series. **GPS Solutions**, v. 26, n. 1, p. 17, nov. 2021. ISSN 1521-1886.

LOCUBICHE-SERRA, S.; SECO-GRANADOS, G.; LÓPEZ-SALCEDO, J. A. Performance limits and benefits of adaptive autoregressive Kalman filters for GNSS scintillation-robust carrier tracking. In: **2021 International Conference on Localization and GNSS (ICL-GNSS)**. [S.l.]: IEEE, 2021. p. 1–6.

LOMBARDI, M. A. The Use of GPS Disciplined Oscillators as Primary Frequency Standards for Calibration and Metrology Laboratories. **NCSLI Measure**, National Institute of Standards and Technology, v. 3, n. 3, p. 56–65, jan. 2008. ISSN 1931-5775, 2381-0580.

LOPES, R.; ANTREICH, F.; FOHLMEISTER, F.; KRIEGEL, M.; KUGA, H. Linear time-invariant filtering for real-time monitoring of ionospheric scintillation in GNSS receivers. **GPS Solutions**, v. 27, maio 2023.

LOPES, R. A. M.; ANTREICH, F.; FOHLMEISTER, F.; KRIEGEL, M.; KUGA, H. K. Ionospheric Scintillation Mitigation With Kalman PLLs Employing Radial Basis Function Networks. **IEEE Transactions on Aerospace and Electronic Systems**, v. 59, n. 5, p. 6878–6893, out. 2023. ISSN 1557-9603.

LUCENA, A. M. P. de; SILVA, F. d. A. T. F. da; SILVA, A. S. da. Scintillation Effects in S-Band Telemetry Link of INPE's Earth Station in Cuiaba-Brazil. **Radioengineering**, v. 30, n. 4, p. 739–748, set. 2021. ISSN 1210-2512.

MACDOUGALL, J. W. Distributions of the irregularities which produce ionospheric scintillations. **Journal of Atmospheric and Terrestrial Physics**, v. 43, n. 4, p. 317–325, abr. 1981. ISSN 0021-9169.

MEYR, H.; MOENECLAEY, M.; FECHTEL, S. A. **Digital Communication Receivers: Synchronization, Channel Estimation, and Signal Processing**. [S.l.]: Wiley Online Library, 1998. v. 444.

MIRIYALA, S.; KOPPIREDDI, P. R.; CHANAMALLU, S. R. Robust detection of ionospheric scintillations using MF-DFA technique. **Earth, Planets and Space**, SpringerOpen, v. 67, n. 1, p. 1–5, 2015. ISSN 1880-5981.

MISRA, P.; ENGE, P. Global Positioning System: Signals, Measurements and Performance (Lincoln, MA: Ganga. **Global Positioning System: Signals, Measurements and Performance Lincoln, MA: Ganga**, 2006.

MORAES, A. d. O.; PERRELLA, W. J. Performance evaluation of GPS receiver under equatorial scintillation. **Journal of Aerospace Technology and Management**, Departamento de Ciência e Tecnologia Aeroespacial, v. 1, p. 193–200, 2009–Jul–Dec. ISSN 2175-9146.

MUSHINI, S.; JAYACHANDRAN, P.; LANGLEY, R.; MACDOUGALL, J.; POKHOTELOV, D. Improved amplitude- and phase-scintillation indices derived from wavelet detrended high-latitude GPS data. **Gps Solutions - GPS SOLUT**, v. 16, p. 1–11, jan. 2010.

NAIR, V.; HINTON, G. E. Rectified linear units improve restricted boltzmann machines. In: **Proceedings of the 27th International Conference on Machine Learning (ICML-10)**. [S.l.: s.n.], 2010. p. 807–814.

NAKAGAMI, M. The m-distribution—A general formula of intensity distribution of rapid fading. In: **Statistical Methods in Radio Wave Propagation**. [S.l.]: Elsevier, 1960. p. 3–36.

NIU, F. **Performances of GPS Signal Observables Detrending Methods for Ionosphere Scintillation Studies**. Tese (Doutorado) — Miami University, 2012.

NIU, F.; MORTON, Y.; TAYLOR, S.; PELGRUM, W.; DIERENDONCK, A. J. V. Performances of GPS Signal Observables Detrending Methods for Ionosphere Scintillation Studies. In: **Proceedings of the 25th International Technical Meeting of the Satellite Division of The Institute of Navigation (ION GNSS 2012)**. [S.l.: s.n.], 2012. p. 3435–3443.

NUNES, F. D.; SOUSA, F. M. Generation of Nakagami correlated fading in GNSS signals affected by ionospheric scintillation. In: **2014 7th ESA Workshop on Satellite Navigation Technologies and European Workshop on GNSS Signals and Signal Processing (NAVITEC)**. [S.l.]: IEEE, 2014. p. 1–8. ISBN 1-4799-6529-4.

NUNES, F. D.; SOUSA, F. M. Practical simulation of GNSS signals in the presence of ionospheric scintillation. In: **2014 IEEE/ION Position, Location and Navigation Symposium-PLANS 2014**. [S.l.]: IEEE, 2014. p. 50–58. ISBN 1-4799-3320-1.

NUNES, F. D.; SOUSA, F. M. G.; MARÇAL, J. M. V. Multi-Frequency Simulation of Ionospheric Scintillation Using a Phase-Screen Model. **NAVIGATION: Journal of the Institute of Navigation**, Institute of Navigation, v. 69, n. 4, dez. 2022. ISSN 0028-1522, 2161-4296.

PACELLI, R.; FLORINDO, R. d. L. **Ita-Gnss-Lab/Code-Iono-Scint-Charact: Characterization of the Ionospheric Scintillation from Its Time Series Estimates.** 2025. ITA GPS/GNSS Laboratory.

PACELLI, R. V.; Aragon-Angel, A.; GARCÍA, A. R.; de Almeida, A. L. F.; ANTREICH, F. Convolutional Neural Networks for Time Series Classification of Ionospheric Scintillation. In: **Proceedings of the 37th International Technical Meeting of the Satellite Division of The Institute of Navigation (ION GNSS+ 2024)**. [S.l.: s.n.], 2024. p. 3019–3028. ISSN 2331-5954.

PACELLI, R. V.; FLORINDO, R.; ANTREICH, F.; Aragon-Angel, A.; Rovira-Garcia, A.; de Almeida, A. L. F. Characterizing Equatorial Scintillation Signals Using Dimensional-Wise Convolutional Neural Networks and Class Activation Maps. **GPS Solutions**, Springer Nature, jun. 2025.

PACELLI, R. V.; FLORINDO, R. d. L. **Ita-Gnss-Lab/Gnss-Scintillation-Simulator**. 2025. ITA GPS/GNSS Laboratory.

PACELLI, R. V.; FLORINDO, R. d. L.; ANTREICH, F.; de Lucena, A. M. P. An all-digital coherent AFSK demodulator for CubeSat applications. **Digital Signal Processing**, v. 162, p. 105147, jul. 2025. ISSN 1051-2004.

PACELLI, R. V.; FLORINDO, R. d. L.; ANTREICH, F.; de Almeida, A. L. F.; Aragon-Angel, A.; GARCIA, A. R. Characterization of Ionospheric Scintillation Using Deep Learning Models. In: **Proceedings of the 38th International Technical Meeting of the Satellite Division of The Institute of Navigation (ION GNSS+ 2025)**. [S.l.: s.n.], 2025. p. 3339–3352. ISSN 2331-5954.

PAPOULIS, A.; UNNIKRISHNA, S.; PILLAI, S. U.; ATHANASIOS, P.; S, U. P.; S, P. **Probability, Random Variables and Stochastic Processes**. 4th ed. edição. ed. Boston: McGraw-Hill Education, 2001. ISBN 978-0-07-366011-0.

PASZKE, A.; GROSS, S.; MASSA, F.; LERER, A.; BRADBURY, J.; CHANAN, G.; KILLEEN, T.; LIN, Z.; GIMELSHEIN, N.; ANTIGA, L. Pytorch: An imperative style, high-performance deep learning library. In: **Advances in Neural Information Processing Systems**. [S.l.: s.n.], 2019. v. 32.

PAULA, ER. D.; RODRIGUES, FS.; IYER, KN.; KANTOR, IJ.; ABDU, MA.; KINTNER, PM.; LEDVINA, BM.; KIL, H. Equatorial anomaly effects on GPS scintillations in Brazil. **Advances in Space Research**, Elsevier, v. 31, n. 3, p. 749–754, 2003. ISSN 0273-1177.

PROAKIS, J.; SALEHI, M. **Digital Communications**. 5th. ed. Boston: Mc Graw Hill, 2007. ISBN 978-0-07-295716-7.

PROAKIS, J. G. **Digital Communications**. 4th. ed. [S.l.]: Mc Graw Hill, 2000. ISBN 978-0-07-118183-9.

PSIAKI, M. L.; HUMPHREYS, T. E.; CERRUTI, A. P.; POWELL, S. P.; KINTNER, P. M. Tracking L1 C/A and L2C signals through ionospheric scintillations. In: **Proceedings of the 20th International Technical Meeting of the Satellite Division of the Institute of Navigation (ION GNSS 2007)**. [S.l.: s.n.], 2007. p. 246–268.

PSIAKI, M. L.; JUNG, H. Extended Kalman filter methods for tracking weak GPS signals. In: **Proceedings of the 15th International Technical Meeting of the Satellite Division of the Institute of Navigation (ION GPS 2002)**. [S.l.: s.n.], 2002. p. 2539–2553.

RATCLIFFE, J. A. Some aspects of diffraction theory and their application to the ionosphere. **Reports on progress in physics**, IOP Publishing, v. 19, n. 1, p. 188, 1956. ISSN 0034-4885.

RINO, C.; BREITSCH, B.; MORTON, Y.; JIAO, Y.; XU, D.; CARRANO, C. A compact multi-frequency GNSS scintillation model. **NAVIGATION**, v. 65, n. 4, p. 563–569, 2018. ISSN 2161-4296.

RINO, C.; BREITSCH, B.; MORTON, Y.; XU, D.; CARRANO, C. GNSS signal phase, TEC, and phase unwrapping errors. **NAVIGATION: Journal of the Institute of Navigation**, v. 67, n. 4, p. 865–873, dez. 2020. ISSN 2161-4296.

RINO, C. L.; CARRANO, C. S. A compact strong-scatter scintillation model. In: **Proceedings of the International Beacon Satellite Symposium**. [S.l.]: Citeseer, 2013.

RINO, C. L.; CARRANO, C. S.; RODDY, P. Wavelet-based analysis and power law classification of C/NOFS high-resolution electron density data. **Radio Science**, AGU, v. 49, n. 8, p. 680–688, 2014.

RINO, C. L.; GROVES, K. M.; CARRANO, C. S.; GUNTER, J. H.; PARRIS, R. T. Digital signal processing for ionospheric propagation diagnostics. **Radio Science**, v. 50, n. 8, p. 837–851, 2015. ISSN 1944-799X.

RINO, CL. A power law phase screen model for ionospheric scintillation: 1. Weak scatter. **Radio science**, AGU, v. 14, n. 6, p. 1135–1145, 1979. ISSN 1944-799X.

RUFENACH, C. L. Power-law wavenumber spectrum deduced from ionospheric scintillation observations. **Journal of Geophysical Research (1896-1977)**, v. 77, n. 25, p. 4761–4772, 1972. ISSN 2156-2202.

SEPTENTRIO. **PolaRx5S User Manual**. [S.l.], 2018.

SHAFT, P. On the Relationship Between Scintillation Index and Rician Fading. **IEEE Transactions on Communications**, v. 22, n. 5, p. 731–732, maio 1974. ISSN 1558-0857.

SHISHOV, V. I. Dependence of the form of the scintillation spectrum on the form of the spectrum of refractive-index inhomogeneities communication I. A phase screen. **Radiophysics and Quantum Electronics**, Springer, v. 17, n. 11, p. 1287–1292, 1974.

SILVA, D. B. Formação e desenvolvimento de bolhas de plasma na ionosfera equatorial: Observação e simulação. 2017.

STRANG, G. **Linear Algebra and Learning from Data**. [S.l.]: Wellesley-Cambridge Press Cambridge, 2019. v. 4.

SUBIRANA, J. S.; ZORNOZA, J. M. J.; HERNÁNDEZ-PAJARES, M. **GNSS Data Processing, Vol. I: Fundamentals and Algorithms**. [S.l.]: ESA Communications, 2013. v. 1. ISBN 978-92-9221-886-7.

TEUNISSEN, P. J.; MONTENBRUCK, O. **Springer Handbook of Global Navigation Satellite Systems**. [S.l.]: Springer, 2017. v. 10.

VALLEY, G. S. **GSV4004B User Manual**. 1131 Seena Avenue, Los Altos, CA 94024, USA, 2017. 51 p.

VASYLYEV, D.; BÉNIGUEL, Y.; VOLKER, W.; KRIEGEL, M.; BERDERMANN, J. Modeling of ionospheric scintillation. **Journal of Space Weather and Space Climate**, EDP Sciences, v. 12, p. 22, 2022.

Vilà-Valls, J.; CLOSAS, P.; Fernández-Prades, C. Advanced KF-based methods for GNSS carrier tracking and ionospheric scintillation mitigation. In: **2015 IEEE Aerospace Conference**. [S.l.: s.n.], 2015. p. 1–10. ISSN 1095-323X.

VILÀ-VALLS, J.; LINTY, N.; CLOSAS, P.; DOVIS, F.; CURRAN, J. T. Survey on signal processing for GNSS under ionospheric scintillation: Detection, monitoring, and mitigation. **NAVIGATION: Journal of the Institute of Navigation**, Institute of Navigation, v. 67, n. 3, p. 511–535, 2020. ISSN 0028-1522.

WANG, Z.; YAN, W.; OATES, T. Time series classification from scratch with deep neural networks: A strong baseline. In: **2017 International Joint Conference on Neural Networks (IJCNN)**. Yokohama, Japan: IEEE, 2017. p. 1578–1585.

WHITNEY, H. E.; AARONS, J.; MALIK, C. A proposed index for measuring ionospheric scintillations. **Planetary and Space Science**, v. 17, n. 5, p. 1069–1073, maio 1969. ISSN 0032-0633.

WHITNEY, HE.; AARONS, J.; ALLEN, RS.; SEEMANN, DR. Estimation of the cumulative amplitude probability distribution function of ionospheric scintillations. **Radio Science**, AGU, v. 7, n. 12, p. 1095–1104, 1972. ISSN 1944-799X.

XU, D.; MORTON, Y. A Semi-Open Loop GNSS Carrier Tracking Algorithm for Monitoring Strong Equatorial Scintillation. **IEEE Transactions on Aerospace and Electronic Systems**, v. 54, n. 2, p. 722–738, abr. 2018. ISSN 1557-9603.

XU, D.; MORTON, Y. J.; RINO, C. L.; CARRANO, C. S.; JIAO, Y. A two-parameter multifrequency GPS signal simulator for strong equatorial ionospheric scintillation: Modeling and parameter characterization. **NAVIGATION**, v. 67, n. 1, p. 181–195, 2020. ISSN 2161-4296.

ZHANG, QT. A decomposition technique for efficient generation of correlated Nakagami fading channels. **IEEE Journal on Selected Areas in Communications**, IEEE, v. 18, n. 11, p. 2385–2392, 2000. ISSN 0733-8716.

ZHAO, B.; LU, H.; CHEN, S.; LIU, J.; WU, D. Convolutional neural networks for time series classification. **Journal of Systems Engineering and Electronics**, v. 28, n. 1, p. 162–169, fev. 2017. ISSN 1004-4132.

ZHOU, B.; KHOSLA, A.; LAPEDRIZA, A.; OLIVA, A.; TORRALBA, A. Learning Deep Features for Discriminative Localization. In: **2016 IEEE Conference on Computer Vision and Pattern Recognition (CVPR)**. [S.l.: s.n.], 2016. p. 2921–2929. ISSN 1063-6919.

ZIEMER, R.; TRANTER, W. H. **Principles of Communications: System Modulation and Noise**. [S.l.]: John Wiley & Sons, 2006. ISBN 81-265-0839-6.

APÊNDICE A – SCINTILLATION INDICES

The development of triggering mechanisms that indicate whether scintillation-induced interference is present on the received signal dates back to the 1970s, when GPS receivers were used to measure scintillation on an experimental basis (FREMOUW *et al.*, 1978). Since then, ISMRs have appeared on the market to specifically monitor the scintillation activity. These devices are integrated into GNSS receiver arrays to compute the scintillation indices, which are continuously compared to preset thresholds, triggering the system in case of a scintillation event (DIERENDONCK; ARBESSER-RASTBURG, 2004). When other ionospheric-related parameters (*e.g.*, TEC, spectral slope, etc.) are also computed, they are called GNSS ionospheric scintillation and TEC monitors (GISTMs). Usually, lock time, C/N_0, and the average of code/carrier divergence[1] are also provided by ISMRs. Figure 18 shows a diagram block overview of a typical ionospheric scintillation monitoring station, where the main components of the signal and data processing chain (correlator bank, navigation bit detection and frame synchronization, *etc.*) are shown. Note that, while the usual processing steps for navigation maintain the same, we have a branch in the signal processing chain that is used to compute the scintillation indices from the postcorrelated signal.

Figura 18 – Diagram block overview of a typical ionospheric scintillation monitoring station.

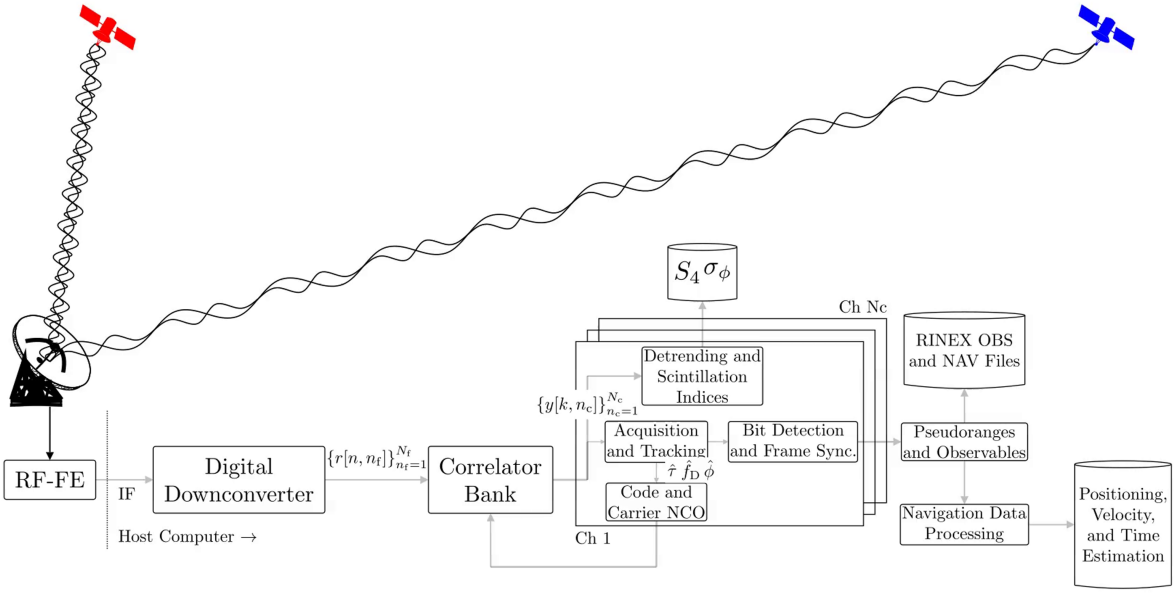

Amplitude scintillation can be quantified using the S_4 index, which is defined as the ratio between the standard deviation of the received signal power and its average power. Let

[1] The code/carrier divergence is also used to provide a multipath detection mechanism (VALLEY, 2017).

us first consider the total amplitude scintillation index, that is, without removing the effect of ambient noise or multipath:

$$S_{4,T} = \sqrt{\frac{\langle I^2 \rangle - \langle I \rangle^2}{\langle I \rangle^2}} \in \mathbb{R}, \tag{A.1}$$

where $I \in \mathbb{R}_+$ are the 50-Hz detrended signal intensity and $\langle \cdot \rangle$ is the ensemble average which, under the assumption of ergodicity, equals the time average over the interval of interest (usually 60 s). This index was introduced by Briggs e Parkin (1963) and became a standard in commercial ISMRs.

The detrended signal intensity is computed from the prompt correlator output. Therefore, its operating rate is directly related to the correlation interval of the tracking loop. The usual sample rate of the prompt correlator output used by ISMRs is[2] 50 Hz, which corresponds to a correlation interval of 20 ms (TEUNISSEN; MONTENBRUCK, 2017, p. 407). In the case of the GPS signals, this aligns with the bit duration[3] of the navigation message, ensuring coherent integration and preventing computation disruptions over navigation bit transitions (LOPES *et al.*, 2023a).

To obtain the amplitude scintillation index, the first step is to compute the raw signal intensity, $SI[k] \in \mathbb{R}_+$, from the prompt correlator output in such as way that this value is not affected by power noise. This is accomplished by computing the so-called narrow and wide band powers (DIERENDONCK *et al.*, 1993), given by

$$NBP[k] = \left(\sum_{i=kM}^{(k+1)M-1} \mathrm{Re}\{y[i]\} \right)^2 + \left(\sum_{i=kM}^{(k+1)M-1} \mathrm{Im}\{y[i]\} \right)^2 \tag{A.2}$$

and

$$WBP[k] = \sum_{i=kM}^{(k+1)M-1} \left(\mathrm{Re}\{y[i]\}^2 + \mathrm{Im}\{y[i]\}^2 \right), \tag{A.3}$$

respectively, where $\mathrm{Re}\{\cdot\}$ and $\mathrm{Im}\{\cdot\}$ take the real and imaginary part of the input argument, $y[k] \in \mathbb{C}$ is the kth output sample from the prompt correlator, and M is the number of samples used in each instant. The parameter M is set so that the narrow and wide band power output at 50 Hz. Naturally, this value depends on the correlation interval: the shorter it is, the higher M is. The correlation interval varies between 1 ms and 20 ms depending on the receiver architecture

[2] Some commercial ISMRs (e.g., PolaRx5S) can also output the unfiltered correlation output at 100 Hz for a more in-depth scintillation analysis (SEPTENTRIO, 2018).

[3] The unique exception is the L2C signal, in which the bit duration is 40 bit/s (SUBIRANA *et al.*, 2013, p. 23).

and system performance (TEUNISSEN; MONTENBRUCK, 2017, p. 407). Finally, the raw signal intensity reads $SI[k] = NBP[k] - WBP[k]$ (LOPES *et al.*, 2023a).

An important aspect in computing the raw signal intensity is the influence of the AGC, which is employed to maintain the signal power at a constant level. In Dierendonck e Arbesser-Rastburg (2004), it was proposed that the AGC be disabled to prevent it from masking scintillation effects. Conversely, a receiver with analogue AGC voltage can also be used to measure amplitude variations. However, calibration techniques must be applied to ensure that the AGC has no contributions on the measured scintillation intensity (WHITNEY *et al.*, 1969).

When scintillation is conducted with low earth orbit (LEO) satellites, such as those from the U.S. Air Force's Wideband project (P76-5), the received signal intensity with no AGC correction shows variations due to the rapid changes in the LOS geometry propagation. A detrending technique must be employed to compensate this effects (CURRAN *et al.*, 2014). This is done by detrending the raw signal intensity, $SI[k]$. Once this disturbance is eliminated, the remaining effects are then assumed to be due to scintillation plus unwanted multipath and ambient noise, which should also be tackled (JIAO; MORTON, 2015). A detrending process for amplitude scintillation, proposed by Dierendonck *et al.* (1993), consists of normalizing it as follows:

$$I = \frac{SI[k]}{SI_{\text{lpf}}[k]}, \tag{A.4}$$

where $SI_{\text{lpf}}[k]$ is obtained after passing $SI[k]$ through a sixth-order lowpass Butterworth filter so that other sources that affect the signal power variation can be eliminated. In some ISMRs, such as Valley (2017), the cutoff frequency of the Butterworth filter is left to the user's discretion, although the value of 0.1 Hz is a common choice. If it is set to zero or left unset, an average over the last minute is used to normalize the raw scintillation intensity, that is,

$$I = \frac{SI[k]}{\langle SI[k] \rangle}. \tag{A.5}$$

Although the sixth-order Butterworth filtering is the most conventional technique to detrend the raw signal intensity, it is well known to cause "phase without amplitude" phenomena frequently observed at high latitude (FORTE; RADICELLA, 2002; MUSHINI *et al.*, 2010; BEACH, 2006). Therefore, by following the recommendations of the Air Force Research Laboratory, the (A.5) is also valid (DIERENDONCK; ARBESSER-RASTBURG, 2004; WHITNEY *et al.*, 1969).

When medium earth orbit (MEO) or geostationary earth orbit (GEO) satellites are used, the scintillation intensity is not strongly affected by satellite-to-receiver power variations.

In this case, some ISMRs may not use detrending technique, that is, $I = SI[k]$ (CURRAN *et al.*, 2014).

Some extra efforts are still required to remove the effects of ambient noise and multipath. Ambient noise can be eliminated by estimating the average signal-to-noise ratio (SNR) density over the 60-s time interval and using that estimate to compute S_4 due to ambient noise. The main rationale behind this is that, since deep fades like those observed in equatorial region are mostly caused by the diffraction effect, one can assume a situation where the signal is forward scattered, thus not changing the average received power (KULLSTAM; KESKINEN, 2000; KINTNER *et al.*, 2009). A direct consequence of this assumption is that the received signal can, eventually, experience a signal enhancement if the scattered waves interfere constructively[4]. In practice, since the SNR is not available, the 60-second average of the estimated C/N_0 is used, and the corrected S_4 index reads (VALLEY, 2017; DIERENDONCK *et al.*, 1993)

$$S_4 = \sqrt{\frac{\langle I^2 \rangle - \langle I \rangle^2}{\langle I \rangle^2} - \frac{100}{\langle C/N_0 \rangle}\left[1 + \frac{500}{19\,\langle C/N_0 \rangle}\right]}. \tag{A.6}$$

When there is no scintillation activity at all, the radicand might be slightly negative. When this happens, this formula can be easily corrected by setting it to zero. Commercial ISMRs output both the total S_4 index ($S_{4,T}$) and its correction every 60 s (SEPTENTRIO, 2018).

Concerning the multipath effect, the main idea is to analyze how different the code and carrier phase behave so that we can detect multipath-induced variations on the S_4 index. Since the code measurements are much more affected by multipath than carrier phase measurements, the code phase will diverge much more when multipath is present, thus providing a way to detect it (DIERENDONCK; ARBESSER-RASTBURG, 2004). The detection mechanism is based on the difference between the code and phase pseudorange over the last minute in which the S_4 index is computed. This value is used to detect high S_4 values that are likely due to multipath (DIERENDONCK; ARBESSER-RASTBURG, 2004).

Although some commercial ISMRs output the S_4 index (e.g., GSV4004B), some authors prefer to compute it directly from the high-rate raw correlator output, which is also provided by the receiver (JIAO; MORTON, 2015; DIERENDONCK; ARBESSER-RASTBURG, 2004). This approach enables the customization of parameters, such as the average interval, detrending techniques, S_4 output rate, etc. The parameter M is also adjusted so that the narrow and wide band power output at 50 Hz (see (A.2) and (A.3)). The typical operating rates of $y[k]$

[4] This behavior is captured by the Nakagami-*m* stochastic process (DIERENDONCK; ARBESSER-RASTBURG, 2004).

found in the literature are 100 Hz (corresponding to a correlation interval of $T = 10$ ms) and 1 kHz (corresponding to a correlation interval of $T = 1$ ms), which lead to $M = 2$ and $M = 20$, respectively (JIAO *et al.*, 2017a; DIERENDONCK; ARBESSER-RASTBURG, 2004). Note that, in either way, $MT = 20$ ms, which is equal to the navigation bit interval of GPS signals, thus ensuring coherent integration and preventing computation disruptions over navigation bit transitions (LOPES *et al.*, 2023a).

For phase scintillation monitoring, a common approach is to estimate the standard deviation of the 50-Hz detrended carrier phase, that is,

$$\sigma_\phi = \sqrt{\langle \phi^2 \rangle - \langle \phi \rangle^2} \in \mathbb{R}, \tag{A.7}$$

where $\phi \in \mathbb{R}$ are the detrended phase signal. The averaging process performs similarly to the amplitude scintillation index, that is, σ_ϕ also operates at 1 Hz. The detrending phase uses a sixth-order high-pass digital Butterworth filter, which removes the low-frequency effects below the 0.1 Hz cut-off frequency (DIERENDONCK; ARBESSER-RASTBURG, 2004). This process, however, is mainly impaired by the oscillator phase noise as it might not be removed by filtering, and by far would dominate the estimated scintillation phase. Fortunately, previous studies have reported that the oscillator phase noise is reduced to desired levels when the widely adopted TCXO oscillator is substituted by the OCXO (DIERENDONCK *et al.*, 1993).

APÊNDICE B – STATISTICAL CHARACTERIZATION OF THE BASEBAND NOISE

In the following Appendix, we will statistically describe the discrete-time noise $\eta[n] \in \mathbb{C}$ that disturbs the baseband received signal (vide (2.9)).

Recall that the transmitted signal is impaired by $\eta_{\mathrm{RF}}(t)$, a zero-mean and real-valued white Gaussian noise whose two-sided PSD is $N_0/2$. After the down-conversion to intermediate frequency, the IF analogue filter eliminates the out-of-band interference around f_{IF}. For the sake of simplicity, suppose that it performs ideal filtering so that the PSD of the filtered Gaussian noise in intermediate frequency, $\eta_{\mathrm{IF}}(t) \in \mathbb{R}$, can be approximated to

$$S_{\eta_{\mathrm{IF}}}(f) = \begin{cases} \dfrac{N_0}{2} & |f \pm f_{\mathrm{IF}}| \leq B_{\max} \\ 0 & \text{otherwise} \end{cases}, \tag{B.1}$$

where $B_{\max} \in \mathbb{R}$ is the maximum bandwidth among all transmitted baseband signals, $s(t, n_{\mathrm{c}}) \in \mathbb{C}$, defined as one-half of the frequency support of its spectrum (PROAKIS; SALEHI, 2007, p. 20). Although the spectrum of a complex envelope is not necessarily centred at 0 Hz, in our case, $s(t, n_{\mathrm{c}})$ happens to be real (*vide* comments in Section 2.1) and therefore its spectrum is Hermitian symmetric[1] (HAYKIN; VEEN, 1998, p. 207). In this case of symmetry, its spectrum is necessarily centred at 0 Hz and limited within the frequency range $[-B_{\max}, B_{\max}]$.

By considering a linear filtering, since $\eta_{\mathrm{RF}}(t)$ is zero-mean, Gaussian, and WSS, it follows that $\eta_{\mathrm{IF}}(t)$ has the same properties (PAPOULIS *et al.*, 2001, p. 398). Therefore, the variance of $\eta_{\mathrm{IF}}(t)$ reads

$$\sigma_\eta^2 = \mathrm{E}\left[\eta_{\mathrm{IF}}^2(t)\right] - \mathrm{E}\left[\eta_{\mathrm{IF}}(t)\right]^2 = \mathrm{E}\left[\eta_{\mathrm{IF}}^2(t)\right] = P_\eta = \int_{-\infty}^{\infty} S_{\eta_{\mathrm{IF}}}(f)\,\mathrm{d}f = 2N_0 B_{\max}, \tag{B.2}$$

where $\mathrm{E}[\cdot]$ is the statistical expectation operator and P_η is the power noise, which equals the variance as the process is zero-mean.

Although there is no single lowpass equivalent of a bandpass signal, we can still define a complex envelope with a clear frequency-domain interpretation. Let $\eta(t) \in \mathbb{C}$ be the complex envelope or lowpass equivalent of $\eta_{\mathrm{IF}}(t)$, then (MEYR *et al.*, 1998, p. 37)

$$\eta_{\mathrm{IF}}(t) = \sqrt{2}\,\mathrm{Re}\left\{\eta(t)\, e^{j2\pi f_{\mathrm{IF}} t}\right\}, \tag{B.3}$$

where

$$\eta_+(t) = \eta(t)\, e^{j2\pi f_{\mathrm{IF}} t} \in \mathbb{C} \tag{B.4}$$

[1] A spectrum $A(f)$ is Hermitian or conjugate symmetric if and only if $A^*(f) = A(-f)$ or, alternatively, $|A(f)| = |A(-f)|$ and $\angle A^*(f) = -\angle A(f)$.

is the analytic signal or the pre-envelope of $\eta(t)$, which is obtained after passing $\eta_{\text{IF}}(t)$ through a filter whose transfer function is $\sqrt{2}U(f)$, where

$$U(f) = \begin{cases} 0, & f < 0 \\ \frac{1}{2}, & f = 0 \\ 1, & f > 1 \end{cases} \tag{B.5}$$

is called the phase splitter or Heaviside step function (PROAKIS; SALEHI, 2007, p. 17). Therefore, the PSD of the analytic signal is

$$S_{\eta_+}(f) = 2|U(f)|^2 S_{\eta_{\text{IF}}}(f) = \begin{cases} N_0 & |f - f_{\text{IF}}| \leq B_{\max} \\ 0 & \text{otherwise} \end{cases}. \tag{B.6}$$

By using (B.4), it is easy to see that

$$R_\eta(\tau) = \mathrm{E}\left[\eta^*(t)\,\eta(t+\tau)\right] \tag{B.7}$$

$$= R_{\eta_+}(\tau)\, e^{-j2\pi f_{\text{IF}}\tau}, \tag{B.8}$$

where $R_\cdot(\tau)$ denotes the autocorrelation function with respect to its subscript and $\cdot^*$ indicates the conjugate operator. By applying the Fourier transform on both sides of (B.8) and recalling (B.6), we have that

$$\boxed{S_\eta(f) = S_{\eta_+}(f + f_{\text{IF}}) = \begin{cases} N_0, & |f| \leq B_{\max} \\ 0, & \text{otherwise} \end{cases},} \tag{B.9}$$

where $S_\cdot(\tau)$ denotes the power spectral density with respect to its subscript. Note that the variance of the baseband noise remains $\sigma_\eta^2 = P_\eta = 2N_0 B_{\max}$. Moreover, since $\eta_{\text{IF}}(t)$ is zero-mean, WSS, and Gaussian, it follows that both $\eta_+(t)$ and $\eta(t)$ have the same properties (MEYR *et al.*, 1998, p. 38).

Equation (B.3) can be further developed as

$$\eta_{\text{IF}}(t) = \sqrt{2}\eta_i(t)\cos(2\pi f_{\text{IF}} t) - \sqrt{2}\eta_q(t)\sin(2\pi f_{\text{IF}} t), \tag{B.10}$$

where $\eta(t) = \eta_i(t) + j\eta_q(t)$ and $\eta_i(t), \eta_q(t) \in \mathbb{R}$ are the in-phase and quadrature component of $\eta(t)$, respectively. Since $\eta(t)$ is a zero-mean WSS Gaussian process, its in-phase ($\eta_i(t)$) and quadrature ($\eta_q(t)$) components are also zero-mean WSS Gaussian processes (MEYR *et al.*, 1998, p. 40).

By using (B.10), the autocorrelation function of $\eta_{\mathrm{IF}}(t)$ can be expressed as

$$\begin{aligned} R_{\eta_{\mathrm{IF}}}(\tau) = & \ \mathrm{E}\left[\, \eta_{\mathrm{IF}}(t)\, \eta_{\mathrm{IF}}(t+\tau)\right] \\ & = \mathrm{E}\Big[\sqrt{2}\left(\eta_i(t)\cos(2\pi f_{\mathrm{IF}} t) - \eta_q(t)\sin(2\pi f_{\mathrm{IF}} t)\right) \\ & \qquad \sqrt{2}\left(\eta_i(t+\tau)\cos(2\pi f_{\mathrm{IF}}(t+\tau)) - \eta_q(t+\tau)\sin(2\pi f_{\mathrm{IF}}(t+\tau))\right)\Big]. \end{aligned} \tag{B.11}$$

By expanding this product, we have that

$$\begin{aligned} R_{\eta_{\mathrm{IF}}}(\tau) = & \quad 2R_{\eta_i}(\tau)\cos(2\pi f_{\mathrm{IF}}(t+\tau))\cos(2\pi f_{\mathrm{IF}}(t+\tau)) \\ & + 2R_{\eta_q}(\tau)\sin(2\pi f_{\mathrm{IF}}(t+\tau))\sin(2\pi f_{\mathrm{IF}}(t+\tau)) \\ & - 2R_{\eta_i,\eta_q}(\tau)\cos(2\pi f_{\mathrm{IF}}(t+\tau))\sin(2\pi f_{\mathrm{IF}}(t+\tau)) \\ & - 2R_{\eta_q,\eta_i}(\tau)\sin(2\pi f_{\mathrm{IF}}(t+\tau))\cos(2\pi f_{\mathrm{IF}}(t+\tau)), \end{aligned} \tag{B.12}$$

where $R_{a,b}(\tau) = \mathrm{E}\left[a^*(t)\, b(t+\tau)\right]$ denotes the cross-correlation function between $a(t)$ and $b(t)$. By using some trigonometric identities[2], it follows that

$$\begin{aligned} R_{\eta_{\mathrm{IF}}}(\tau) = & \quad \big(R_{\eta_i}(\tau) + R_{\eta_q}(\tau)\big)\cos(2\pi f_{\mathrm{IF}} t) \\ & + \big(R_{\eta_i}(\tau) - R_{\eta_q}(\tau)\big)\cos(2\pi f_{\mathrm{IF}}(t+\tau)) \\ & - \big(R_{\eta_i\eta_q}(\tau) - R_{\eta_q,\eta_i}(\tau)\big)\sin(2\pi f_{\mathrm{IF}} t) \\ & - \big(R_{\eta_i\eta_q}(\tau) + R_{\eta_q,\eta_i}(\tau)\big)\sin(2\pi f_{\mathrm{IF}}(t+\tau)) \end{aligned} \tag{B.13}$$

Since $\eta(t)$ is proper[3], zero-mean, and WSS, the following proprieties hold (PROAKIS, 2000, p. 159)

$$R_{\eta_i}(\tau) = R_{\eta_q}(\tau), \tag{B.14}$$

$$R_{\eta_i,\eta_q}(\tau) = -R_{\eta_q,\eta_i}(\tau) = -R_{\eta_i,\eta_q}(-\tau), \tag{B.15}$$

where the second equation in (B.15) uses a basic property[4] of ACF for real-valued signals. Therefore, the second and fourth term in (B.13) cancel, yielding

$$R_{\eta_{\mathrm{IF}}}(\tau) = 2R_{\eta_i}(\tau)\cos(2\pi f_{\mathrm{IF}} t) - 2R_{\eta_i,\eta_q}(t)\sin(2\pi f_{\mathrm{IF}} t). \tag{B.16}$$

---

[2] $\cos(\alpha)\cos(\beta) = (\cos(\alpha-\beta) + \cos(\alpha+\beta))/2$
$\sin(\alpha)\sin(\beta) = (\cos(\alpha-\beta) - \cos(\alpha+\beta))/2$
$\sin(\alpha)\cos(\beta) = (\sin(\alpha-\beta) + \sin(\alpha+\beta))/2$

[3] A complex-valued and WSS process $a(t)$ is called proper when its pseudocovariance is zero, *i.e.*, $\mathrm{E}\left[(a(t) - \mathrm{E}[a(t)])^2\right] = 0$ (PROAKIS; SALEHI, 2007, p. 65).

[4] $R_{a,b}(\tau) = \mathrm{E}[a(t)\, b(t+\tau)] = \mathrm{E}[b(t+\tau)\, a(t)] = R_{b,a}(-\tau),\ \forall\, a(t), b(t) \in \mathbb{R}$

On the other hand, by considering the properties (B.14) and (B.15) and recalling that $\eta(t) = \eta_i(t) + j\eta_q(t)$, the ACF of $\eta(t)$ reads

$$\begin{aligned} R_\eta(\tau) &= \mathrm{E}\left[\eta^*(t)\,\eta(t+\tau)\right] \\ &= R_{\eta_i}(\tau) - jR_{\eta_i,\eta_q}(\tau) + jR_{\eta_q,\eta_i}(\tau) + R_{\eta_q}(\tau) \\ &= 2(R_{\eta_i}(\tau) - jR_{\eta_i,\eta_q}(\tau)) \end{aligned} \tag{B.17}$$

By substituing (B.17) into (B.16), we have that

$$R_{\eta_{\mathrm{IF}}}(\tau) = \mathrm{Re}\Big\{R_\eta(\tau)\,e^{j2\pi f_{\mathrm{IF}}t}\Big\} \tag{B.18}$$

Hence, the PSD of $\eta_{\mathrm{IF}}(t)$ in terms of $\eta(t)$ reads (PROAKIS, 2000, p. 161)

$$\begin{aligned} S_{\eta_{\mathrm{IF}}}(f) &= \int_{-\infty}^{\infty} \mathrm{Re}\Big\{R_\eta(\tau)\,e^{j2\pi f_{\mathrm{IF}}t}\Big\}e^{-j2\pi ft}\,\mathrm{d}f \\ &= \frac{1}{2}\left(S_\eta(f - f_{\mathrm{IF}}) + S_\eta(-f - f_{\mathrm{IF}})\right), \end{aligned} \tag{B.19}$$

which perfectly matches with (B.1) if we substitute (B.9) into (B.19).

By taking separately the real and imaginary parts in (B.17) and recalling the properties (B.14) and (B.15), it follows that (MEYR *et al.*, 1998, p. 38 *et seq.*)

$$R_{\eta_q}(\tau) = R_{\eta_i}(\tau) = \frac{1}{2}\mathrm{Re}\big\{R_\eta(\tau)\big\} \overset{\mathcal{F}\{\cdot\}}{\longleftrightarrow} S_{\eta_i}(\tau) = S_{\eta_q}(\tau) = \frac{1}{4}\left(S_\eta(f) + S_\eta(-f)\right) \tag{B.20}$$

and

$$R_{\eta_i,\eta_q}(\tau) = \frac{1}{2}\mathrm{Im}\big\{R_\eta(\tau)\big\} \overset{\mathcal{F}\{\cdot\}}{\longleftrightarrow} S_{\eta_i,\eta_q}(f) = \frac{1}{4j}\left(S_\eta(f) - S_\eta(-f)\right), \tag{B.21}$$

where $\mathrm{Im}\{\cdot\}$ takes the imaginary part of the input argument and $\cdot \overset{\mathcal{F}\{\cdot\}}{\longleftrightarrow} \cdot$ indicates that the left-hand side (in time domain) and the right-hand side (in frequency domain) form a Fourier transform pair.

From (B.15), one can infer that $R_{\eta_i,\eta_q}(0) = 0$ and therefore $\eta_i(t)$ and $\eta_q(t)$ are uncorrelated (only for $\tau = 0$) (PROAKIS, 2000, p. 161). However, since we assume ideal filtering, the stochastic process $\eta_{\mathrm{IF}}(t)$ is bandpass symmetric[5] around f_{IF}, which means that $S_\eta(f)$ is a symmetric function, *i.e.*, $S_\eta(f) = S_\eta(-f)$ (MEYR *et al.*, 1998, p. 40). Thus, the

[5] A stochastic process $a(t) \in \mathbb{R}$ is said to be bandpass symmetric around f_0 iff. $U(f+f_0)S_a(f+f_0) = U(-f+f_0)S_a(-f+f_0)$ (MEYR *et al.*, 1998, p. 40).

equations (B.20) and (B.21) can be simplified to

$$\boxed{R_{\eta_q}(\tau) = R_{\eta_i}(\tau) = \frac{1}{2}\mathrm{Re}\{R_\eta(\tau)\} \overset{\mathcal{F}\{\cdot\}}{\longleftrightarrow} S_{\eta_i}(\tau) = S_{\eta_q}(\tau) = \frac{1}{2}S_\eta(f) = \begin{cases} \frac{N_0}{2}, & |f| \leq B_{\max} \\ 0, & \text{otherwise} \end{cases}} \tag{B.22}$$

and

$$\boxed{R_{\eta_i,\eta_q}(\tau) = \frac{1}{2}\mathrm{Im}\{R_\eta(\tau)\} = 0 \overset{\mathcal{F}\{\cdot\}}{\longleftrightarrow} S_{\eta_i,\eta_q}(f) = 0,} \tag{B.23}$$

respectively. Note that the same conclusions can be made if we recall the following Fourier transform property: if $S_\eta(f)$ is symmetric and real, then $R_\eta(\tau)$ is also symmetric and real (although $\eta(t)$ is complex) (HAYKIN; VEEN, 1998, p. 209). Moreover, we can also conclude that, for this condition of symmetry, $\eta_i(t)$ and $\eta_q(t+\tau)$ are uncorrelated not only for $\tau = 0$ but for all $\tau \in \mathbb{R}$.

Therefore, by substituting (B.22) and (B.23) into (B.17) and (B.16), we have that

$$\boxed{R_\eta(\tau) = 2R_{\eta_i}(\tau)} \tag{B.24}$$

and

$$\boxed{R_{\eta_{\mathrm{IF}}}(\tau) = 2R_{\eta_i}(\tau)\cos(2\pi f_{\mathrm{IF}} t)} \tag{B.25}$$

By taking the inverse Fourier transform in (B.9), we have that

$$R_\eta(\tau) = \mathcal{F}^{-1}\{S_\eta(t)\} = N_0 \int_{-B_{\max}}^{B_{\max}} e^{j2\pi f\tau}\,\mathrm{d}f = 2N_0 B_{\max}\,\mathrm{sinc}(2\tau B_{\max}), \tag{B.26}$$

where

$$\mathrm{sinc}(x) = \frac{\sin(\pi x)}{\pi x} \tag{B.27}$$

and $\mathcal{F}^{-1}\{\cdot\}$ denotes the inverse Fourier transform of the input argument. Finally, considering a sampling interval of $T_\mathrm{s} = 1/2B_{\max}$ and disregarding the quantization noise, the autocorrelation function of $\eta[n]$ can be approximated to

$$\boxed{R_\eta(mT_\mathrm{s}) \triangleq R_\eta[m] = 2N_0 B_{\max}\delta[m],} \tag{B.28}$$

where

$$\delta[m] = \begin{cases} 1 & m = 0 \\ 0 & \text{otherwise} \end{cases} \tag{B.29}$$

is the Kronecker function. Note that the clock error signal is not included as $\eta(t)$ is assumed to be WSS and therefore its statistics do not change with a time-shifting. In Section 2.1, we denote the discrete-time noise as $\eta[n, n_{\mathrm{f}}]$ once we admit differences across the narrowband signals. Such differences come from nonideal frequency response of the RF stage or from the presence of other frequency-dependent interferences arising from the receiver circuit, before the signal is digitalized. However, if we assume that the noise is still WSS across the narrowband signals, then the autocorrelation function of $\eta[n, n_{\mathrm{f}}]$ can be approximated to (B.28) for all $n_{\mathrm{f}} \in \{1, 2, \cdots, N_{\mathrm{f}}\}$, where N_{f} is the number of narrowband signals.